Utilizing Solar Vapour Energy by Use of Nanofluids in a Direct Absorption Solar Collector

by
Edda Torsdottir Ulset

Master's Program in Energy
with Specialization in Energy Technology

January, 2018

Geophysical Institute
University of Bergen
Norway

Abstract

Traditional solar thermal collectors and photovoltaic (PV) systems suffer from low energy conversion efficiencies. This is mainly due to high thermal losses from overheated absorber plates or solar cells. For steam generation purposes, certain nanofluids (NFs) have been proposed as an alternative due to their high photothermal response and possibility of direct light-to-steam conversion by volumetric absorption. High temperature steam in a direct absorption solar collector (DASC) can potentially be used for electricity generation, purification of drinking water and sterilization. However, efficient and cheap solutions are needed in order to compete against other energy production methods.

Many researchers have focused on the absorption process within NFs, but few have investigated the boiling of NFs creating high temperature steam, especially the effect of varying the nanoparticle (NP) concentration. In this thesis, a low cost solution is proposed by use of carbon black (CB) and iron oxide (IO) NPs, both known to posses high thermal conductivities. Three volumetric absorbers with a variety of concentrations were experimentally investigated and compared with regard to: time to boiling, vapour temperature, evaporation ratio, absorption, and vapour generation efficiency. A surfactant, sodium dodecyl sulfate (SDS), was added to a range of CB NF samples in order to investigate how the dispersion stability effected the boiling. In addition, possible NP contamination of NF condensates were investigated by use of Raman spectroscopy and static light scattering (SLS).

The findings from this study confirm enhanced boiling of CB and IO NFs compared to water, and prove the importance of dispersion stability of NFs. A NP concentration of 2.00 wt.% resulted in the highest performance for all three NFs. The 2.00 wt.% IO NF achieved the highest steam temperature of 129°C and improved the vapour generation efficiency by $88.3 \pm 0.08\%$. The other NFs also presented excellent performance. Nevertheless, the SLS analysis revealed NP contamination in all condensates of CB NF samples containing SDS, in addition to the NF condensates belonging to IO concentrations of $\geqslant 3.00$ wt.%. This can be attributed to the wettability effects of both SDS and increased IO concentration. These findings can prevent the latter concentrations of NFs from being used in applications where clean water is important, or in systems where NP deposition needs to be avoided.

Acknowledgments

Foremost, I would like to express my very great appreciation to my supervisors associate professor Boris V. Balakin of the Department for Mechanical and Marine Engineering at Western Norway University of Applied Sciences, and professor Pawel Kosinski of the Department of Physics and Technology at University of Bergen. Thank you Boris V. Balakin for your passionate participation and valuable input, and thank you Pawel Kosinski for guidance, useful comments and encouragement. They were always very helpful and supportive. My sincere thanks also goes to the entire Solar-Nano[1] research group for constructive comments, in addition to endless meetings and discussions.

A special thanks goes to Chief Engineer Rachid Maad at the Department of Physics and Technology and Department Engineer Roald Langøen at the mechanical workshop for the help in developing the experimental set-up. Thank you Rachid Maad for insightful comments and remarks.

I would also show my gratitude to the bachelor students Sindre Løver Hovden and Mathias Endal Tennebø of the Department for Mechanical and Marine Engineering at Western Norway University of Applied Sciences for their contribution in characterizing the radiative heat flux constituting from the radiation source used for this work. I would also like to thank Chief Engineer Egil Nodland of the Department of Chemistry at the University of Bergen for the chemometric data analysed in this thesis. Furthermore, I thank Irene Heggstad of ElmiLab at the University of Bergen for help and guidance in obtaining electron microscopes data, and Julia Zabednova for programming in ImageJ.

My sincere thanks also goes to Pavel Struchallin from Moscow Engineering Physics Institute for the provision of valuable SDS data of condensate samples obtained in this work. Finally I would like to thank dr Konstantin Redkin and professor Isaac Garcia at Pittsburgh University for their collaboration with the Solar-Nano research group, and especially for the electron microscope characterization of a dried NF sample prepared in this study.

Bergen, January 2018

Edda Torsdottir Ulset

[1] solar-nano.com

Contents

Nomenclature

a	Thermal diffusivity	[m^2s^{-1}]
A	Area	[m^2]
A_b	Absorbance	
c	Concentration	[mol m^{-3}]
C_p	Specific heat capacity	[J kg^{-1} K^{-1}]
d	Particle diameter	[m]
E	Energy	[J]
E_{abs}	Absorbed radiation power	[W m^{-2}]
E_v	Emitted radiation power	[W m^{-2}]
g	Gravitational acceleration	[ms^{-2}]
Gr	Grashof number	
h	Heat transfer coefficient	[W m^{-2} K^{-1}]
h_f	Enthalpy of formation	[J kg^{-1}]
h_{fg}	Latent heat of vaporization	[J kg^{-1}]
h_g	Specific enthalpy of saturated vapour	[J kg^{-1}]
h_s	Specific enthalpy of superheated vapour	[J kg^{-1}]
H	Enthalpy	[J]
I	Radiative heat flux	[W m^{-2}]
k	Thermal conductivity	[$Wm^{-1}K^{-1}$]
$K_{a,v}$	Absorption coefficient	[m^{-1}]
L	Characteristic length	[m]
m	Mass	[kg]
$\dot{m}$	Mass flow	[kg s^{-1}]
n	Complex component of the refractive index	
N	Relative complex refractive index (particles to fluid)	
Nu	Nusselt number	
P	Pressure	[Pa]
Pr	Prandl number	
Ra	Rayleigh number	
t	Time	[s]
T	Temperature	[°C, K]
V	Volume	[m^3]
Q	Heat	[J]
$\dot{Q}$	Thermal power	[W]
x, y, z, l	Distance	[m]

Greek letters

α	Absorptivity	
β	Thermal expansion coefficient	$[K^{-1}]$
δ	Thickness of boundary layer	[m]
η	Efficiency	
ε	Emissivity	
ε_x	Extinction coefficient	$[m^2 mol^{-1}]$
λ	Wavelength	[m]
μ	Absolute viscosity	$[kg\ m^{-1} s^{-1}]$
ν	Kinematic viscosity	$[m^2 s^{-1}]$
ϕ	Volume fraction	
ρ	Density	$[kg\ m^{-3}]$
σ	Stefan-Boltzmann's constant	$[W\ m^{-2} K^{-4}]$
χ	Particle size parameter	

Subscripts, superscripts

ABS	Absorption
CV	Convection
CO	Conduction
p	Constant pressure

Abbreviations

CB	Carbon black
CNT	Carbon black nanotube
$DASC$	Direct Absorption Solar Collector
GCB	Graphitized carbon black
GNP	Gold nanoparticle
IO	Iron oxide
IR	Infrared
$LCOE$	Levelized cost of energy
$LSPR$	Localized surface plasmon resonance
NF	Nanofluid
NP	Nanoparticle
OAS	One-sun ambient steam generator
PCA	Principal component analysis
PV	Photovoltaic
RT	Response time
SDS	Sodium dodecyl sulfate
SLS	Static light scattering
STE	Solar thermal energy

1. Introduction

1.1 Motivation

In 2016 the world energy consumption was equivalent to $1.544 \cdot 10^{17}$ Wh/year and is estimated to further increase and reach $2.157 \cdot 10^{17}$ Wh/year by the year 2040. Fossil fuels, such as oil, gas or coal, currently cover 85.5 % of the energy use (2016) [1, 2]. In order to prevent emissions to the environment, these need to be replaced with renewable energy. One of the United Nations main goals is to "ensure access to affordable, reliable, sustainable and modern energy for all" [3]. In order to fulfil this target, the utilization of available and clean energy resources must be improved.

The planets most abundant source of energy is the Sun. It emits a thermal power of $3.8 \cdot 10^{26}$ W, where $1.08 \cdot 10^{17}$ W reaches the Earth's surface with an average irradiation of 1366 W/m^2 [4, 5]. The energy potential from the Sun is so immense, that by covering the Earth's surface with solar cells with an efficiency of 0.1, the world energy demand would roughly be covered 420 times. If around 4 % of the area of Sahara desert was covered, the global energy demand would be met. Today the solar energy is utilized by either PV or solar thermal energy (STE) applications. Of the electricity used in 2015, only 1 % was produced by solar energy [1]. For solar energy to be affordable and sustainable, the technological development is crucial. Levelized cost of energy (LCOE)[1] for current solar technologies needs to decrease in order to compete against other conventional energy production methods. Further efficiency enhancement of solar energy technologies could be a key factor to meet future energy requirements.

The energy from the Sun can either be converted directly to electricity by use of PV systems or absorbed in solar thermal collectors for a range of applications. Solar cells can be an appealing choice for energy production, but their construction causes an issue with regard to toxic chemicals, as well as poisonous waste material at the end of their lifetime. PV systems also suffer from overheating, leading to thermal losses and low efficiency. The poor efficiency is mainly due to the bulk materials and dopants lack of ability to absorb the incoming radiation outside of their band gaps. A major reason for selecting a STE application is because they can utilize about twice as much energy as a PV system, see the energy breakdown in figure 1.1. In addition, PV applications lack the capability of storing energy overnight when the Sun is not available. These are important reasons why STE is one of the most promising renewable resources being developed for energy storage, power generation, domestic water heating, distillation, and other industrial processes.

[1] LCOE: a measure of lifetime cost of energy divided by energy production.

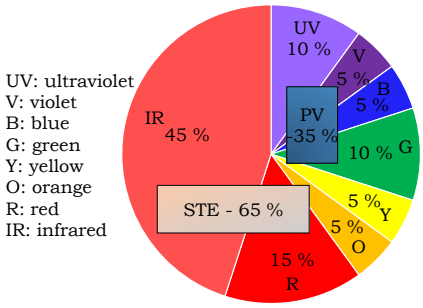

Figure 1.1: Energy breakdown of the solar spectrum. Adapted from Taylor [6].

In addition to the aforementioned applications, STE can potentially be used for water purification purposes. Natural fresh water is scarce in many countries in the world, especially in Africa and the Middle East. Today's available desalination processes of sea water, multi-stage flash distillation and reverse osmosis, require a high electricity demand [7]. Furthermore, these applications are unavailable in areas without electricity. By use of solar heat directly, the energy conversion efficiency will increase and water purification will be independent of available electricity.

To generate electricity a solar collector must achieve high enough evaporation efficiency and steam temperatures to drive a turbine. Conventional power plants rely on large optical concentration of solar energy using mirrors or lenses. This is why solar thermal collectors are usually characterized by their concentration magnitude, divided into two main categories: concentrating collectors and non-concentrating collectors, also called high-temperature and low-temperature solar collectors, respectively [8, 9]. Today the development of existing and new types of solar thermal collectors focuses on minimizing the heat losses within the collector in order to maximize the amount of energy from the available solar radiation.

In concentrated solar collectors, the solar energy heats up a working fluid, for example molten salts or mineral oil, which gives up its energy in a heat exchanger to evaporate a turbine working fluid for electricity production. In most non-concentrating collectors, solar energy is captured by a surface absorber, which heats up the working fluid. Nevertheless, these collectors suffer from high radiative losses due to overheating of the surface. Vacuum can be introduced in some collectors to minimize convectional heat losses, but it is a costly feature when it comes to required material and maintenance. The heat transfer steps for a conventional collector are illustrated in figure 1.2 where R_{CO} represents the energy conversion resistance from the surface absorber to the working fluid.

With advances in technology, concentrated STE power plants are increasing in popularity. The various collectors are classified into four main categories characterized by the way the solar radiation is focused, and the technology used to receive the energy: solar tower, parabolic trough collector, linear Frensel and parabolic dish. The parabolic dish system using a Stirling engine achieves the most efficient energy conversion of all with an efficiency of 18-23% [10]. However, there are several difficulties with current concentrated solar systems: they require a big amount of space and the LCOE is too high compared to other energy applications. In order to reduce the land area and the huge amount of solar concentration needed, a more efficient and cheap energy absorption process is required.

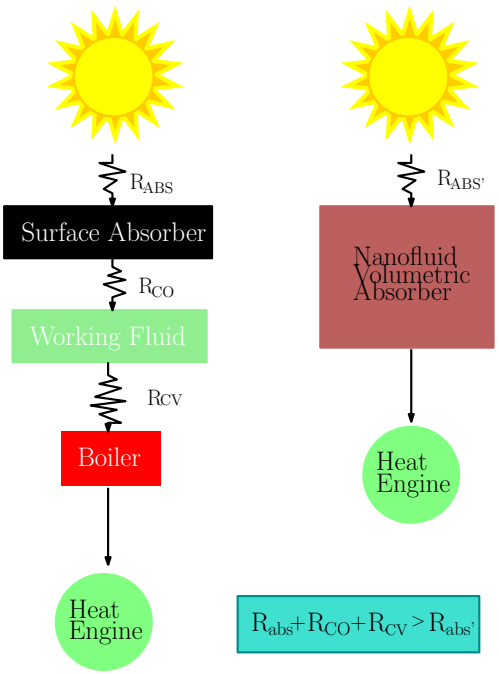

Figure 1.2: Resistance comparison between conventional collector and NF volumetric absorber. R_{ABS}, $R_{ABS'}$, R_{CO} and R_{CV} are thermal resistances corresponding to each heat transfer step.

Recent studies [11–13] have reported 4-40% increased absorption efficiencies by use of NFs in a volumetric absorber, also known as the DASC. NFs, which are by definition NPs dispersed in liquid, hold unique photothermal properties dependent on the type of NPs. The objective is not only to reduce the resistances within the collector, but also to minimize the amount of heat transfer steps achieving a more efficient use of solar energy, see figure 1.2. In addition to power generation, the produced vapour can potentially be used directly in sterilization, distillation, waste water treatment, solar ponds, and in other industrial processes [14–17].

To attain highest possible vapour temperatures with high efficiencies by use of NFs, many factors are involved. The properties of the NF are essential for the vapour generation process. The important factors are the size and shape of the NPs suspended in a liquid (morphology), photothermal properties, rheological behaviour, and dispersion stability [18]. A special attention should be paid to reduce the temperature in the bulk fluid and capture more energy in the superheated parts of the NF [17]. An effort should also be made to use a NF which utilizes the entire solar energy spectrum, that is, wavelengths from 250 to 2500 nm [19], which is one of the objectives of this research.

There is a need of better understanding of the use and behavior of NFs in a direct solar absorber to develop an effective, clean and cheap application to compete against conventional energy production methods. Few researchers have investigated the vapour generation process in NFs by use of solar energy, especially effects of particle concentration [20].

In this thesis three types of NFs are compared experimentally with an extensive variation in concentration to find the optimum NF composition with regard to

absorption and steam generation capabilities. CB and IO NPs were used to produce the NFs due to their enhanced thermal conductivity properties. The effect of adding a surfactant, SDS, to CB NFs was also investigated. Scanning Electron Microscope (SEM) and Transmission Electron Microscope (TEM)-images of the NPs were obtained by use of electron microscopes in order to explore the size distribution and the morphology of the NPs. The condensed steam was captured and analysed by use of Raman spectroscopy to examine if the NPs contaminate the vapour.

1.2 Specific objectives

The specific objectives of this thesis were to:

(i) Optimize and finish an experimental lab set-up.

(ii) Investigate the procedure of producing CB and IO NFs when it comes to chemical additives and concentration.

(iii) Verify NP sizes by use of TEM and SEM analysis.

(iv) Compare CB and IO NFs and concentrations of these with regard to boiling, focusing on:

- Mass change
- Fluid and vapour temperature
- Efficiency

(v) Examine if the NPs contaminate the generated vapour using Raman spectroscopy.

2. Theoretical Analysis

This chapter presents the necessary theoretical background on which the framework of the experimental set-up and the concept of a DASC is based on.

In the first section an introduction on the subject of NPs and NFs is shown. The following section contains a brief literature review of recent studies on NFs illuminated either by a solar simulator, a laser, or directly by the Sun. Next, the attention is directed to the basics of thermal physics in order to elucidate the heat transfer and the approach to calculate the efficiencies of the process. In the same section, further theory on thermal properties relevant for NFs is introduced. Finally, the heat transfer within NFs and potential vapour generation mechanisms are shown.

2.1 Nanoparticles and nanofluids

NPs are particles with a diameter normally between 5 and 100 nm [21]. When these particles are dispersed in a liquid, the fluid is called a NF. For solar heating purposes, some NPs have been studied more than others due to their high photothermal response. It is proven that NP-additions can increase thermal conductivity of bulk fluids used as a heat transfer medium [14, 16, 22]. Some researchers have synthesized and combined custom NPs to enhance their unique heat transfer capabilities [18, 23, 24]. Frequently studied carbon based NPs for heat transfer fluids are CB, graphene, graphitized carbon and carbon nanotubes. Metallic NPs of interest within heat transfer are, for instance, aluminium oxide (Al_2O_3), copper (Cu), gold (Au), IO (Fe_3O_4), nickel (Ni), and titanium oxide (TiO_2).

In addition to demonstrate high thermal conductivity, metallic NPs exhibit exceptional absorption properties due to an optical phenomenon known as localized surface plasmon resonance (LSPR) [17, 25]. When the metallic NPs are illuminated by light consisting of wavelengths larger than the NP size, the electrons located in the conduction band interact with the radiation and cause energetic oscillations, see illustration in figure 2.1. This leads to a rapid temperature increase of the NPs. In addition to material and size, the LSPR frequency is dependent upon factors such as agglomeration (NP clustering), inter-particle distance, and particle shape [26].

NFs have shown to hold different characteristics than fluids containing larger particles (μm or mm) [27]. The decreased particle size leads to a larger surface-to-volume ratio, which improves thermal properties. In addition, nanosized particles do not block channels in which NFs are transported as easily as bigger sized particles [22]. The latter is applicable if the NF were to be transported in tubes, for example in

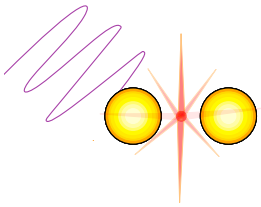

Figure 2.1: LSPR

a circulation system. To avoid blockage of channels, it is also essential that the NPs do not agglomerate. The particle size is therefore important in terms of the overall efficiency of a DASC system. Illumination of these NPs will therefore lead to high temperatures, making them suitable for absorbing radiation from directed sunlight.

CB NPs are one of few substances with similar absorption characteristics as the ideal concept of a black body, which in theory absorbs all incident radiation. Duffie et al. [28] report that 99% of incoming radiation can be absorbed by a thick layer of CB, which makes these NP suited for use in a volumetric absorber. Han et al. [29] also reveal good absorption in the entire solar spectrum for CB NFs. Although the cost of carbon based NPs is lower than of metal NPs [30], the unique nature of ferromagnetic NPs in a NF can be used to be manipulate the heat transfer process by use of magnetic fields.

As mentioned in previous section (2.4.2), NF heat transfer is a complex topic which today's researchers are attempting to understand in full detail in order to find and control the optimum NP material with regard to size, shape and concentration in a bulk fluid. Taylor et al. [19] describes the drawback of having too concentrated NF: absorption will only happen at the surface and light will not penetrate the liquid, which increases heat loss to surroundings. If the concentration is too low, the light will be transmitted and not utilized.

The preparation of NFs are normally categorized into either a one-step or two-step process [19]. In the one-step process, the NPs are directly synthesized inside the base fluid to accomplish the desired volume or mass fraction. This procedure can minimize particle clustering and does not require the additional effort of drying, transportation, and storage of NPs. The drawback with this method is that impurities will exist in the NF due to incomplete reactions inside the NF [27]. The two-step process first involves synthesizing the NPs to a desired shape and size, then adding it to the base fluid. Due to the existing NP production techniques, which are already scaled up in the process industry, the two-step method is more commonly used than the one-step process [31]. However, a big drawback with the two-step process is easily agglomerated NP powders. Although the resulting product from the two-step process will lead to a cleaner result with regard to impurities, the entire process is more energy consuming. This is an important topic when it comes to LCOE of a DASC system.

As a result of the large surface-to-volume ratio of the NPs, the reactive interface increases. NPs tend to agglomerate at a certain distance due to the van der Waals forces [32]. Factors increasing NP clustering are mainly fluid motion, gravitational force and the Brownian motion. In order to prevent agglomeration in NFs, the

solution can either be mechanically stirred using a magnetic stirrer, treated in a high-pressure homogenizer, or dispersed by use of an ultrasonic cleaner or disruptor. Hwang et al. [33] experimentally tested the latter methods using 0.5 wt.% CB NF, with an addition of surfactant (1.0 wt.% SDS) that prevents agglomeration and produces a more stable solution. TEM images from the results showed no improvement using a stirrer, but agglomeration decreased using both an ultrasonic bath and a disruptor. The most stable NF was prepared using the high-pressure homogenizer, which breaks agglomerates in an environment with a high shear force and cavitation.

In order to obtain a stable NF, chemical additions such as surfactants and pH buffers are normally used [33]. However, NFs containing surfactants tend to break down at high temperatures, which will decrease the stability after a certain time [19]. To maintain the NF stability in a DASC, one may suggest adding a sonificator, but this can be complex as well as costly.

2.2 Literature review

The most recent research concerning volumetric absorbers for steam generation purposes is reviewed below. The literature survey presents different approaches of NF production and the utilization opportunities existing for volumetric solar absorbers.

Gold NPs (GNPs) have shown to improve the heat generation within volumetric absorbers. Neumann et al. [23] developed nanoshell particles consisting of silica and gold (SiO_2/Au). They performed experiments showing boiling by illumination of sunlight, generating steam temperatures up to 150°C. The results showed that 80% of the solar energy was converted into steam. This steam could be sufficient enough to drive a turbine or to sterilize medical instruments. Neumann et al. also discovered that by use of nanoshell-particles, the distillation fractions exceeded the azeotropic limit for conventional fractional distillation. An ethanol fraction of 99% was produced, which is much higher than the conventional 95% [21]. Neumann et al. suggest that the nanoshells weakens the hydrogen-bonds between water and pure ethanol, and that this could be an explanation for the high fraction of ethanol [16].

Jin et al. [17] observed an enhanced heating and vapour production using customized GNPs. The results showed NF stability for more than two months with no change in the chemical properties of the NF. The experiments were conducted with focused natural sunlight using Frensel lenses. The GNP NF was placed in an inner tube inside a quartz-tube (to sustain high temperatures), where the tubes were separated by vacuum to reduce heat losses. With an illumination of 220 sun (1 sun = 1000 W/m^2), the highest solar vapour efficiency was 80.3% using 12.75 ppm GNP. Three separate thermocouples were used, unlike in the experiments performed by Neumann et al., where they only used a single measurement point. Jin et al. state that their experimental and numerical data are in significant disagreement with the hypothesised local vapour bubble mechanism elaborated in a later section of the thesis. They report that this mechanism is not possible for low heat fluxes below 1 MW/m^2 produced by concentrated sunlight using e.g. Frensel lenses. However, Jin

et al. claim that this mechanism can occur using high fluence lasers with a radiance higher than 1000 MW/m^2 [17, 34].

An alternative to the costly gold NPs is proposed in a study by Ghasemi et al. [14]. A thermal conversion efficiency of 85% was achieved using a hydrophilic double layer structure (DLS) made of graphene and carbon NPs with a solar illumination source of 10 sun. The DLS transported water through the pores using capillary forces and evaporated the water inside the layer. The carbon foam was used for insulation with graphene on top to absorb the incoming sunlight. For comparison Ghasemi et al. conducted another experiment using CB NF instead of DLS in the same set-up. The NF was made of 0.5 wt.% CB dissolved in deionized water and sonificated for one hour [14]. Using a solar simulator, the results showed higher steam temperatures, faster evaporation and higher efficiency for the DLS. With 10 sun, the vapour and efficiency of the system using CB NF was 80°C and $75 \pm 3\%$. Corresponding data for DLS was 100°C and $85 \pm 3\%$.

Ni et al. [30] investigated graphitized CB (GCB), graphene and CB NFs by sonificating 0.5 wt.% of the respective NPs in distilled water for one hour without any surfactant. In the experimental set-up, the NFs were isolated using a concentric acrylic tube surrounded by aerogel particles. The particles were situated in a bigger tube and sealed off by acrylic discs on top to reduce heat losses. Using 10 sun, vapour generation efficiency was estimated to 69% for all three NFs. Ni et al. state that higher efficiencies are achievable in a larger set-up due to an increased ratio between the surface and volume. Experiments showed that the transient efficiency of GCB and graphene NFs is 7% better than for the CB NF. By comparing all three NFs, GCB reached steady state fastest.

The different properties corresponding to various NPs can be optimized through chemical design. For instance, NPs can be modified in order to increase their dispersion stability in a fluid. Liu et al. [13] experimentally prepared graphene NPs and compared their performance with unmodified graphene in a DASC. The results showed increased dispersion of modified NPs in the ionic liquid $[HMIM]BF_4$ compared to the unmodified graphene. By use of data from numerical simulations and experiments, Liu et al. present no change in transmittance for the modified graphene after being heated to the boiling point, while the unmodified sample induced 20-80% transmittance. They also reveal a stable receiver efficiency for the unmodified sample of 85-89% after the boiling point, but a 37% decrease in efficiency for the unmodified graphene. Liu et al. attribute this to a possible increase in agglomeration in the unmodified graphene for high temperatures, which shows the importance of dispersion stability within a DASC.

In addition to GNPs and carbon based NPs, magnetic NPs are also promising for photothermal applications. Zeng et al. [35] used floating and experimentally prepared Fe_3O_4/C magnetic particles to absorb the incoming sunlight. The IO was incorporated into carbon in order to make a recyclable product and enhancing its photothermal response. Using a solar simulator, Zeng et al. showed an increased evaporation rate by a factor of 2.3 using 3.5% salt water compared to pure water. They demonstrated a successful recycling of the NPs by use of a magnet with almost no influence on the performance.

Chen et al. [7] modified magnetic microspheres consisting of Fe_3O_4 and MFe_2O_4

(M=Mn, Zn, Co) so that they could form a surface layer on top of the water. Evaporation efficiencies of the magnetic microspheres and IO dispersed in water were compared by irradiating a 200 ml sample from above. The efficiency of the microspheres was 1.7 times higher than of the NF consisting of IO.

Sand NPs were prepared and studied by Manikandan et al. [11] in a DASC using propylene glycol and water as the base fluid. The 2.0 vol.% sand propylen glycol NF showed an improved efficiency of 16.5% compared to the pure base fluid. Due to the low freezing point of propylene glycol, this technology could potentially be used in moderate climates. An advantage of using sand is the low cost and high availability of this silica rich substance.

Recent research has focused on the absorption inside the NFs, but few researchers have investigated in which degree the amount of NPs impact the performance of a volumetric absorber. Wang et al. [20] achieved 46.8% efficiency using $19.04 \cdot 10^{-4}$ vol.% NF made of CB nanotubes (CNTs) and distilled water with a radiation in the range of 1-10 sun. Four concentrations of CNT NFs were experimentally tested. Due to several temperature sensors situated in different layers of the NF, they were able to record localized heating in the top layer of the NF. Findings from this study show that heating of the entire bulk fluid was not required in order to boil the NFs.

NFs can also be used for heat transfer applications without high temperature steam generation. Ni et al. [15] demonstrated a floating solar receiver, a one-sun ambient steam generator (OAS), which evaporates the water surface without concentrated solar light. The main part of the OAS consisted of a thermal insulator made of polystyrene foam, which served to float the whole structure on top of a body of water. Situated on the top of the foam, a cermet coated on copper was used as a selective absorber. Finally, the selective absorber was covered with a transparent layer made of bubble wrap in order to reduce convective heat losses. A cotton wick was inserted through the structure to deliver water from the cold water to the hot absorber using capillary forces. Ni et al. demonstrated the OAS's ability to reach steam temperatures up to 100°C even with interruptions in illuminations due to cloud cover or seasonal variation.

Future work is necessary to find inexpensive and efficient methods to generate high temperature steam without the need of pressurizing the system. Few researchers have investigated the effect of steam generation by recording vapour temperature, especially with respect to a wide range of NF concentrations. In addition, a DASC should include condensate recycling in order to optimize the utilization of waste heat and resources. Very few reports were found regarding the matter of condensate contamination of NPs. The extensive potential of using inexpensive NFs, either CB or IO NPs, in a direct solar absorber lays the ground work of this thesis.

2.3 Thermal physics

2.3.1 Heat transfer

Heat is a form of energy transferred from a continuum to another as a result of temperature difference. The Merriam Webster dictionary defines heat as "the energy associated with the random motions of the molecules, atoms, or smaller structural units of which matter is composed" [36]. The mechanism of heat transfer is usually divided into three main categories: conduction, convection and radiation.

Radiation

Radiation is transfer of energy in the form of electromagnetic waves called photons [37]. These energy packets have been observed to possess both wave and particle characteristics. The energy of a single photon is given by hv, where h is the Planck's constant and v denotes its frequency [38]. The frequency of a photon is given by its wavelength and the speed of light. The radiation frequency categorizes the type of radiation (eg. radio waves, microwaves, x-rays, ultraviolet light and gamma rays), where visible light is only a minor part of the electromagnetic spectrum, see figure 2.2. Unlike conduction and convection, heat transfer through radiation does not require a medium and can travel through vacuum or any transparent solid or fluid.

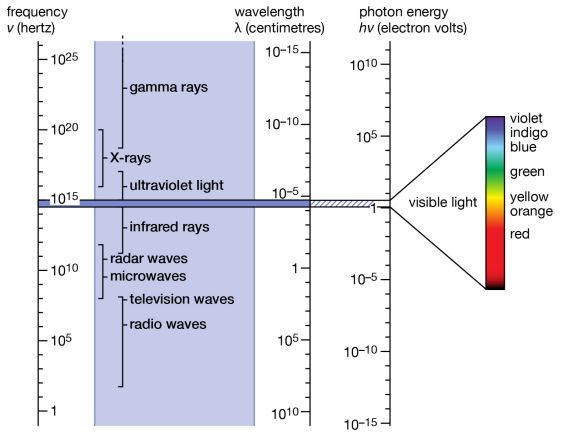

Figure 2.2: Electromagnetic spectrum of light. Reproduced from Encyclopædia Britannica [39].

All bodies with a temperature greater than 0 K emit electromagnetic energy in form of thermal radiation [28]. This is due to intermolecular kinetic energy. Thermal radiation emitted by a body may be calculated using the Stefan-Boltzmann's law: $\dot{Q}_{emit} = \varepsilon\,\sigma\,A\,T_s^4$, where T_s is the temperature [K] of the surface A, ε is the emissivity and σ is the Stefan-Boltzmann's constant: 5.6704×10^{-8} W/(m^2·K^4) [37]. For an idealized surface called a black body, $\varepsilon = 1$. Based on the Stefan-Boltzmann's law, net radiational heat transfer between two surfaces is determined from:

$$\dot{Q}_{1\to2} = \varepsilon\,\sigma\,A_1\,F_{1\to2}\,(T_1^4 - T_2^4), \tag{2.1}$$

where $\dot{Q}_{1\to2}$ is the heat transfer per unit time from body 1 to body 2. A_1 is the surface of body 1. T_1, T_2 are the temperatures [K] of body 1 and body 2, respectively. $F_{1\to2}$ is the view factor, i.e. the fraction of radiation from A_1 falling on A_2.

Incoming radiation can either be absorbed by a body, reflected or transmitted. The fraction of the incoming radiation which is absorbed is given by the absorptivity α of a surface. Like emissivity, absorptivity is a value between 0 and 1, where $\alpha = 1$ for a black body which absorbs all incoming radiation. The amount of energy absorbed by a surface is determined by the wavelength and the temperature of the incoming radiation. The visible, ultraviolet, and near-infra red region of light are of the most dominant wavelengths within solar energy: 0.29-25.00 μm [28]. Photons with short wavelength and high frequency are the ones with the largest energy content. To maximize solar energy utilization an absorber must have excellent absorptivity properties close to 1 without reflecting or transmitting radiation.

Convection

Convection is a heat transfer mechanism occurring between a material and the adjacent liquid or gas, combining conduction and fluid motion. The main types are natural and forced convection. Forced convection is a heat transfer in which a fluid is forced to move. This is usually done to optimize the heat transfer, for example in a heat exchanger. Natural convection is independent of any external source and the fluid motion is due to density gradients only.

The convective heat flux is normally proportional to the difference between the fluid and surface temperature, see figure 2.3 and Newton's law of cooling [40, 41]:

$$\dot{Q}_{conv} = h_c A\,(T_s - T_\infty), \tag{2.2}$$

where T_s is the surface temperature [K], T_∞ is the fluid temperature [K] far from the surface, and h_c is the convective heat transfer coefficient. This coefficient can be found by calculating the average Nusselt number given by $Nu = h_c\,L/k$, where L is the characteristic length and k is the thermal conductivity of the material.

If the temperature of the surface, T_s, has a higher temperature than the ambient temperature, T_∞, the air close to the surface is heated. Due to this heating, the air expands and moves upward, see figure 2.3a. A thermal convective boundary layer will be formed. On the other hand, if the surface is colder than the surrounding fluid, the boundary layer will be mirrored, see figure 2.3b.

The thickness of the boundary layer, δ, can be determined by using thermodynamic calculations involving dimensionless groups such as the Prandtl number and the Grashof number. In order to do this, the following properties of the boundary layer are required: film temperature, volumetric expansion coefficient, and kinematic viscosity.

The Prandtl number represents thermal properties of the fluid and is often extracted from tables [42]. Typical values for the Prandtl number at 1 atm and 20°C are

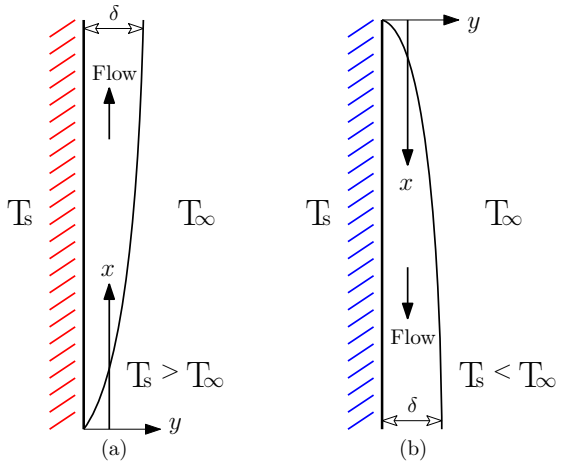

Figure 2.3: Natural convective boundary layers on a vertical surface.

approximately 0.7 for air and 7 for water. By definition, the Prandtl number is given by [42–44]:

$$Pr = \frac{\mu C_p}{k}, \tag{2.3}$$

where μ is the absolute viscosity and C_p is the specific heat capacity of the fluid. For vertical flat plates, the local Grashof number Gr_x for gases is [44, 45]:

$$Gr_x = \frac{g\,\beta\,(T_s - T_\infty)\,x^3}{v^2}, \tag{2.4}$$

where x is the length of the boundary layer and g is gravitational acceleration. The coefficient of thermal expansion β is a property of the fluid. For ideal gases, the coefficient is the inverse of the mean film temperature[1] [40]. Kinematic viscosity ν is given by $\nu = \mu/\rho$, where ρ is the density of the fluid [40]. According to Graebel [44] and Lienhard [42], the thermal boundary layer thickness δ of a vertical isothermal plate is found by:

$$\delta = 3.936\,x \left(\frac{0.952 + Pr}{Pr^2}\right)^{1/4} Gr_x^{-1/4}. \tag{2.5}$$

As mentioned, the film coefficient h_c can be found by calculating the Nusselt number. Nu can be expressed as a function of either the Reynolds or Grashof number, depending on the type of convection analysis. For free convection from a vertical plate, the Nusselt number is given by $f(Gr, Pr)$ [46]:

$$Nu = \left(0.825 + \frac{0.387 Ra^{1/6}}{(1 + (0.492/Pr)^{9/16})^{8/27}}\right)^2, \tag{2.6}$$

where Ra is the Rayleigh number given by $Ra = Pr\,Gr$.

[1]Film temperature: an approximation of the temperature inside the boundary layer, calculated by the mean value of the surface and the fluid temperature.

Conduction

Conduction is transfer of heat through matter due to molecular collisions where more energetic molecules exchange energy with less energetic molecules. Conduction can take place in all phases of matter, but is most significant in solids. The rate of heat transfer in all spatial directions x, y, and z is given by the Fourier's law of heat conduction [40]:

$$\frac{dq}{dA} = -k\left(\frac{\delta T}{\delta x} + \frac{\delta T}{\delta y} + \frac{\delta T}{\delta z}\right) = -k\nabla T, \tag{2.7}$$

where the heat flux dq/dA is proportional to the temperature gradient, ∇T. Eq. (2.7) applies for an isentropic process only, which is an idealized thermodynamic process where the entropy of the system remains constant.

2.3.2 Thermal properties of fluids

Specific heat capacity and latent heat of vaporization

Enthalpy, H, is a thermodynamic state function defined by the sum of the internal energy and the product of pressure and volume: $H = E + PV$, where E is the total internal energy, P the pressure and V the volume of the thermodynamic system [47]. According to the first law of thermodynamics, the change in internal energy is equal to the work done by the system or the energy transferred to the system [48].

When the temperature of a closed system increases, molecular interactions escalate and causes a rise in internal energy. Specific heat capacity is the ratio of change in enthalpy to the change in temperature in a closed system with constant pressure: $C_p = (\Delta H/\Delta T)_p$ [37]. The change in enthalpy of 1 kg of a substance from its constituent elements at its most stable state is conventionally defined as: $h_f = C_p\Delta T$, where h_f is standard enthalpy of formation [49]. In figure 2.4, h_f is given by the energy required to heat one unit mass of water from 0°C to 100°C.

The amount of energy absorbed or released by a material during a phase change without changing its temperature is called latent heat [50]. The energy needed to change the physical state of a substance from liquid to a gas equals the work required to break the intermolecular forces between molecules. This energy is called enthalpy of vaporization or latent heat of vaporization. The heat added to a liquid in order to generate vapour is given by $Q = h_{fg}\Delta m$, where h_{fg} is latent heat and Δm is mass evaporated. The total specific enthalpy of saturated vapour is therefore equal to $h_g = h_f + h_{fg}$.

In figure 2.4, h_s represents specific enthalpy of superheated vapour and is given by $h_s = h_g + C_{ps}(T_s - T_f)$, where T_s is the temperature of the vapour, T_f is the saturation temperature and C_{ps} is the specific heat capacity of the vapour [51].

The values of latent heat of vaporization and specific heat capacity of a substance are often used at standard pressure and temperature (1 atm, 25°C). However, these variables are both pressure and temperature dependent. Figure 2.5 shows how the

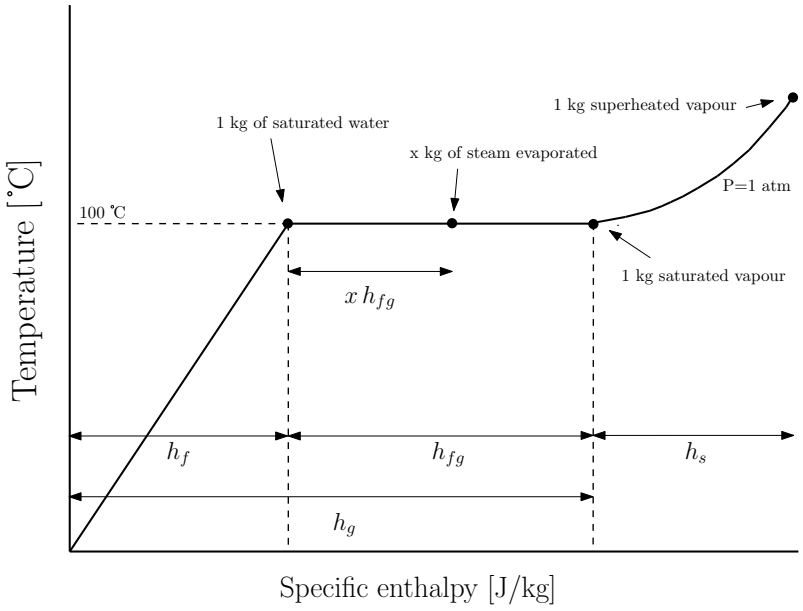

Figure 2.4: Specific enthalpy of water at standard atmospheric pressure.

specific heat capacity of liquid water varies with temperature at 1 atm. The specific heat capacity of liquid water is more or less stable at temperatures from 1°C to 99°C, but a severe decrease in specific heat capacity is observed close to the boiling point. At standard conditions, the specific heat capacity of water is 4180 J/(kg·K), the specific heat capacity of vapour is 1860 J/(kg·K), and the latent heat of vaporization of water is 2257 kJ/kg [20].

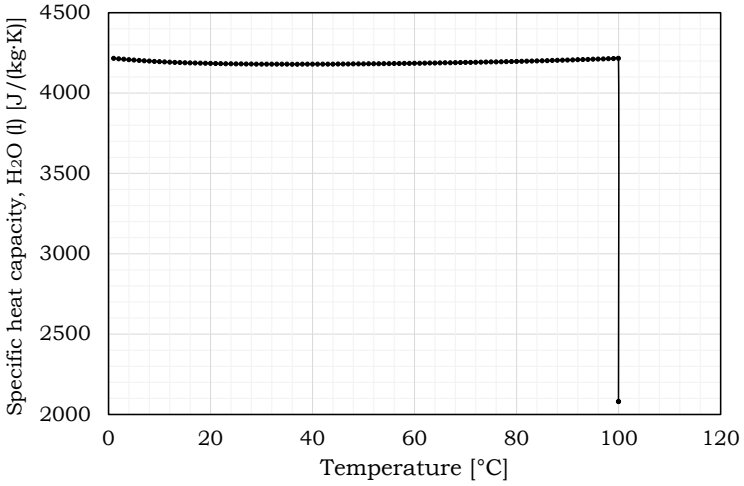

Figure 2.5: Heat capacities of water at standard atmospheric pressure [52].

It has been reported that presence of NPs in water possibly enhances the specific heat capacity and latent heat of vaporization [53–55]. Chieruzzi et al. [56] reported an increase of C_p for $NaNO_3$-KNO_3 NFs containing SiO_2/Al_2O_3 NPs. Ameen et al. [55] revealed trends showing higher h_{fg} values by increased volume fractions and decreased NP sizes, both in an experimental study and through molecular dynamic simulations. They also reviewed the possibility that the increase could be caused by extra bonds between the NPs and the water molecules. Chen et al. [54] reported reduced effects on h_{fg} by adding a surfactant to distilled water droplets. A smaller value of h_{fg} will

enhance water evaporation, while a larger h_{fg} requires additional energy for inducing a phase change. It should be noted that few researchers have investigated the NP effect on C_p and h_{fg}, so this topic is still not explored thoroughly.

Thermal conductivity

Thermal conductivity is a property describing the heat transfer capability of a given material, denoted as k. All materials conduct heat differently, depending on its chemical composition and temperature. The thermal conductivity of a solid, liquid, or gas is related to the specific heat capacity by $k = a\,\rho\,C_p$, where a is thermal diffusivity [57].

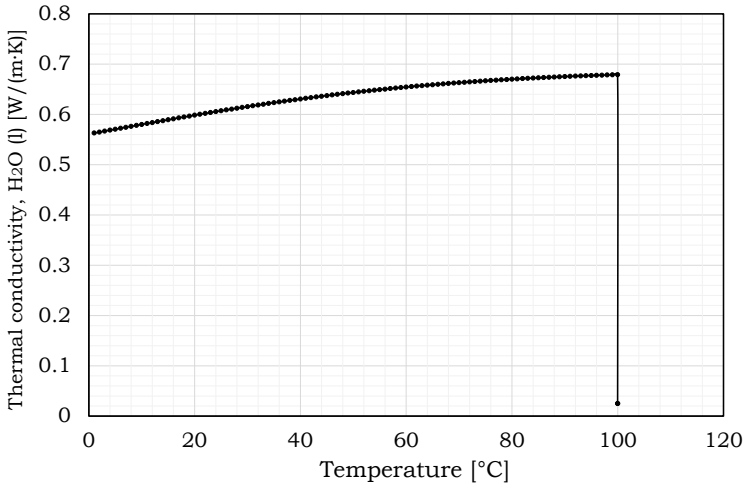

Figure 2.6: Thermal conductivity of water at standard atmospheric pressure [52].

Figure 2.6 illustrates how the thermal conductivity of water varies with temperature at constant pressure. Although water exhibits a high heat capacity, the thermal conductivity of water is rather in the mid-range compared to other substances.

As mentioned in section 2.1, additions of NPs can enhance the thermal conductivity of NFs. Table 2.1 presents thermal conductivity of common materials, which could potentially be used in a NF. Several reports show that NPs exhibiting high values of k increase the thermal conductivity of the bulk fluid [22]. For instance, a thermal conductivity study by Wang et al. [58] showed up to 15% k-enhancement for the water based Al_2O_3 NF and 18% for the water based Cu NF by use of 0.8 wt.% NPs. The higher k-values for the Cu NFs are attributed to the high thermal conductivity of Cu, see table 2.1.

However, some reports conclude that the k of certain NPs does not directly correlate to the k of a NF [22]. For instance, even though Al_2O_3 crystals have a higher thermal conductivity than TiO_3, a study by Yoo et al. [59] revealed a 14% higher k-value for the TiO_3 NF compared to water and only a 4% increase in thermal conductivity for the Al_2O_3 NF. They concluded that that the most important factor determining the thermal conductivity of a NF is the surface-to-volume ratio of the NPs. By comparing water based IO NPs with other water based NFs, the same effect is seen. Zhang et al. [60] discovered 38% k-enhancement for 4.0 vol.% IO NF and 30% higher k for NFs containing Al_2O_3 or TiO_3. Jamilapanah et al. [61] investigated the thermal

conductivity in a range of IO concentrations in ethylene glycol. Their results present an increased thermal conductivity of 51.8% compared to the bulk fluid, by use of 2.00 wt.% IO.

Although many researchers have experimentally investigated the possible increased thermal conductivity of NFs, a robust physical theory explaining the enhancement has not yet been proposed [57].

Table 2.1: Thermal conductivity of materials in room temperature [62–65]. Units are W/(m·K).

Material	k	**Material**	k	**Material**	k
Carbon nanotube	2000	Graphite	167.4	MgO	59.6
SiC	490	Si	160	Al_2O_3	27
Ag	430	Mg	156	Ti	20.9
Cu	400	Zn	111.7	CuO	18
AlN	350	Ni	87.7	TiO_2	6.7
Gold	318	Fe	80.3	Fe_2O_3	0.58
Al	226	ZnO	60	CB	0.375

Absorbance

In chemistry, absorbance is the logarithmic relationship between the incident radiative heat flux to the transmitted radiative heat flux through a material [66]. Absorbance differs from absorptivity (mentioned in subsection 2.3.1) because it also includes reflection and scattering phenomena occuring in a medium. The absorbance of a medium is found using the Beer-Lambert's law [67]:

$$A_b = \log\frac{I_0}{I} = \varepsilon_x \, l \, c, \tag{2.8}$$

where I_0 denotes the incoming radiative heat flux, I denotes the transmitted radiative heat flux, c is the molar concentration, l is the coordinate along the length direction, and ε_x is the molar absorptivity also called the extinction coefficient. Eq. (2.8) states that the absorbance of a liquid is proportional to its concentration. The Beer-Lambert's law can also be simplified by introducing the absorption coefficient: $K_{a,v} = \varepsilon_x \, c$, which is dependent upon the wavelength of the incident light and the material or fluid absorbing the radiation.

In order to attain the absorbance of a medium, the extinction coefficient must be found. The extinction coefficient of a fluid, ε_x, is given by [57]:

$$\varepsilon_x = \frac{4\pi n}{\lambda}. \tag{2.9}$$

In Eq. (2.9), λ is the wavelength of the incident light and n is the complex refractive index, which is an optical property that can be found in many handbooks, for example Palik [68].

If the fluid contains particles, the extinction coefficient can be difficult to find if it is a strong scattering medium [19]. This is typical for high concentrations of particles. Mie scattering theory is a collection of physical laws describing the scattering regime of independent particles [19, 57]. The theory was originally derived for spheres, but was later developed for irregularly shaped particles. The extinction coefficient of a fluid containing particles can be assumed to be found through a simple addition of the extinction coefficients corresponding to each phase [19]:

$$\varepsilon_x = \varepsilon_{x,p} + \varepsilon_{x,bf}, \tag{2.10}$$

where $\varepsilon_{x,p}$ is the extinction coefficient of the particles and $\varepsilon_{x,bf}$ denotes the extinction coefficient of the base fluid given by Eq. (2.9).

Since a major part of the incident light consists of wavelengths with a magnitude larger than the sizes of commonly used NPs (5-100 nm), the scattering (Q_{scat}), absorption (Q_{abs}) and extinction (Q_{ext}) efficiencies for individual NPs can be found [19,57]:

$$Q_{ext} = Q_{abs} + Q_{scat}. \tag{2.11}$$

The absorption and scattering efficiencies are obtained by use of equations according to the Mie scattering theory [19,57], and are not shown in this thesis. These equations involve the particle size parameter χ in addition to the relative complex refractive index N. The latter property describes scattering from particles to the fluid and can be found experimentally by use of a refractometer. The particle size parameter χ, also called the relative particle size, is given by $\chi = \pi d/\lambda$, where d is the mean particle diameter.

Since the scattering efficiency is proportional to d^4 [19, 57], Q_{scat} can be neglected when $Q_{abs} >> Q_{scat}$. This only applies if the NPs and any agglomerates formed in the solution are small. In this case, the extinction coefficient of the particles can be calculated by the approximation:

$$\varepsilon_{x,p} = \frac{300\phi(Q_{abs} + Q_{scat})}{2d} \approx \frac{300\phi Q_{abs}}{2d}, \tag{2.12}$$

where ϕ is the volume fraction of NPs in the bulk fluid [19]. The scattering efficiencies are based on a completely transparent base fluid. This is not true for water, which efficiently absorbs infrared radiation. The absorption of the bulk fluid is taken into account in Eq. (2.10) in order to find the extinction coefficient of the NF.

2.4 Nanofluid heat transfer

2.4.1 Absorption and heat losses

One of the main challenges with all kind of solar energy systems is reduction of heat losses to surroundings. In order to maximize the efficiency of solar thermal systems, it is essential to understand the heat transfer in both conventional surface absorber systems and DASCs.

When radiation passes through matter, the energy from the photons may be absorbed. The magnitude of absorption depends on the characteristics and the length of the material. In surface absorber systems the absorbed radiation is $E_{abs} = \alpha \cdot I_0$, see figure 2.7a. For volumetric absorbers the absorptivity of a NF depends both on the material and the thickness of the fluid layer y [69]. The energy absorbed in a volumetric absorber can be found by rearranging Beer-Lambert's law, Eq. (2.8), by use of $E_{abs} = I_0 - I$:

$$E_{abs} = I_0 \left[1 - \exp(-K_{a,v}\, y)\right], \tag{2.13}$$

where $K_{a,v}$ is the absorption coefficient and y is the thickness of the fluid layer illustrated in figure 2.7b.

Due to particle settling, convection, profile non-uniformity, agglomeration, and other phenomena such as chemical polarity, a fluid can hold different concentration distributions. This can be illustrated as separate layers within a fluid. For further enhancement of absorption capabilities the NFs can be engineered to consist of various layers holding different absorption properties, see figure 2.7c. Figure 2.7b and c demonstrates the differences between conventional surface absorbers and two types of DASC systems. For a NF consisting of layers with various absorption coefficients $K_{a,n}$ and thicknesses y_n, Eq. (2.13) can be rewritten as [69]:

$$E_{abs} = I_0 \left[1 - \exp(-K_{a,1}y_1 - K_{a,2}y_2 \ldots - K_{a,n}y_n - K_{a,n-1}y_{n-1})\right]. \tag{2.14}$$

Eq. (2.14) demonstrates that by adjusting the thickness layer of the NF and its concentration, the most effective absorption configuration can be found. If the NF is made of magnetic NPs, their position could potentially be controlled using magnets.

As mentioned in the radiation section 2.3.1, all bodies with a temperature higher than absolute zero emit thermal radiation. The radiative losses depend on the total hemisphere from which the radiation is emitted. For surface absorbers the total hemisphere consists of a half of the hemisphere of a volumetric absorber, see figure 2.7. By use of the Kirchhoff's radiation law, which states that an idealized black body in thermal equilibrium emits the same amount of energy being absorbed, $\alpha = \varepsilon$, the radiative losses from a volumetric absorber, consisting of one layer, can be calculated combined with the Stefan-Boltzmann's law [69, 70]:

$$E_v = \left[1 - \exp(-K_{a,v}\, y)\right]\sigma T_v^4, \tag{2.15}$$

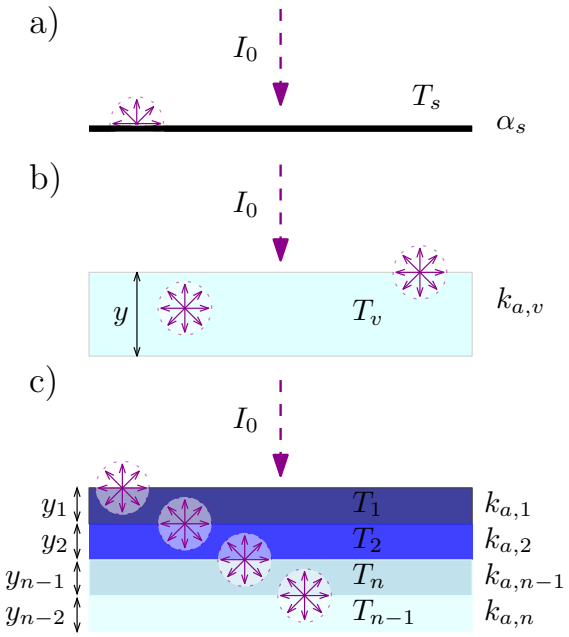

Figure 2.7: Sketch of absorption and radiative losses in a) conventional surface absorbers b) DASC with a layer of y c) engineered DASC-solution with multiple layers. Inspiration from Khullar et al. [69].

where E_v is the emissive power and T_v the NF temperature. Eq. (2.15) shows that by an increase in the absorption coefficient, the emissive power also increases. For volumetric absorber configurations consisting of several layers the emissivity could be even larger [69].

In summary, this demonstrates that a NF can absorb a larger fraction of the incident radiation than a surface absorber, however the radiative losses are theoretically higher in a NF.

2.4.2 Possible boiling scenario

To exploit as much energy of the solar radiation as possible, a better understanding of the heat transfer process is needed. There exist two potential vapour generation mechanisms when heating a NF: the classical heat transfer model based on equilibrium with the surrounding fluid molecules, and the hypothesized local vapour bubble [23, 30, 34, 71].

The first mechanism is based on Fourier's law heat conduction [30, 71]. It is assumed that an equilibrium between the NPs and the bulk fluid will quickly arise during illumination and vapour will be formed due to temperature increase of the bulk fluid. This is followed by homogeneous nucleation of steam bubbles in the bulk fluid. Research and experiments done by Ni et al. [30] suggest that this model applies.

The concept of the second mechanism is that a vapour bubble will be formed and encapsulate each NP. The layer of vapour will have a lower thermal conductivity and prevent heat transfer to the surrounding liquid, which creates a temperature difference between the bulk fluid and the NPs [21,23,72]. If the continued illumination

is sufficient, this layer will grow thicker and vaporize due to the local temperature increase and the density difference, see figure 2.8. The NP will therefore absorb the directed energy whilst being isolated by the vapour bubble. Thermal equilibrium of the entire bulk fluid is reached after a period of time.

This debated phenomenon was first proposed by Neumann et al. [23] and has later been investigated by a number of researchers [20, 73]. Neumann et al. illuminated carbon and SiO_2Au-nanoshell NFs situated in an ice bath. They confirmed localized heating by increased pressure indicating steam production, even though the temperature of the bulk fluid remained 0°C. Lukianova-Hleb et al. [34] attribute this to the NP surface tension pressure applied to the vapour bubble nucleus. However, experimental investigation of the thermal layer around individual NPs is difficult and therefore not yet accomplished. Another concern regarding the formation of a steam shell around an individual NPs is that the Laplacian pressure in the shell must be enormous (several MPa). It is therefore reasonable to assume that the steam bubbles are either formed around clouds of nanoparticles or that the particle-fluid surface tension is sufficiently reduced at nano-scale [16].

Jin et al. [17] state that the localized boiling cannot be explained by the hypothesized nanobubble, but that the conventional heat transfer model applies. They claim that the solar intensity in the focal point generates a superheated region so that a non-uniform temperature distribution will be created throughout the bulk fluid. This can explain intense boiling in local areas of the bulk fluid. Wang et al. [20] suggest that the high evaporation efficiency found in their experimental work is due to localized heating in the top layer at the NF-air interface rather than a consequence of heating the entire bulk fluid.

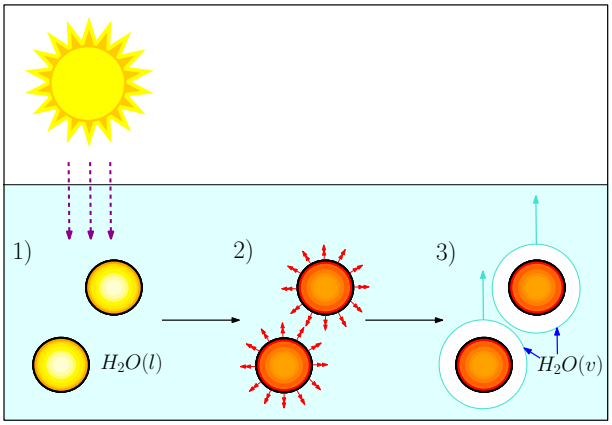

Figure 2.8: Sketch of nanoparticles absorbing energy from the Sun, corresponding to the hypothesized local vapour bubble model. Inspiration from Neumann et al. [23].

3. Methods

3.1 Study design

This work involves experimental research in which the performance of three volumetric absorbers is compared. In this study, CB and IO NPs were chosen to evaluate how the NP wetting influences different stages of the illumination process. CB NF with 1.00 wt.% SDS was also explored to verify if the surfactant had an impact on the heat transfer process. Tap water was used as the base fluid for each NF to conduct realistic experiments for future drinking water applications. Different concentrations of NPs in water were investigated in order to find the NF concentration corresponding to optimum performance. Performance capabilities were analysed with regard to evaporation ratio, maximum vapour temperature, absorption, boiling, and vapour efficiency. In addition, a sample of condensed vapour of each concentration was collected to examine whether the NPs contaminated the water.

In order to conduct repeatable and reliable experiments a set-up was developed, testing a range of temperature sensors. Two halogen lamps, simulating solar radiation, were directed towards a test tube containing the NF sample. Two temperature sensors were attached through the test tube lid, one recording NF temperature and the other vapour temperature. LabView was used in order to record mass change.

3.2 Nanofluid preparation

In this work the one-step process mentioned in section 2.1 was selected due to the straightforward procedure and low cost. Different physical techniques for breaking agglomerates were investigated by Hwang et al. [33] (mentioned in section 2.1). The high-pressure homogenizer was most efficient, but the ultrasonic bath was also reported to have a positive effect. It should be noted that Hwang et al. do not mention the quantity of agglomerates they investigated or how many samples were checked in the analysis. This could have had an effect on the results. In this thesis, Branson 3510 ultrasonic cleaner was used to break agglomerates.

Several researchers [19, 33, 74] have used SDS as the surfactant to prevent agglomeration and induce stability. Taylor et al. [19] and Hwang et al. [33] used 1 wt.%, which showed increased stability. The same amount of SDS was therefore used for the present work in samples containing CB NPs.

CB NPs (Timcal Ensaco 350G) with a bulk density of 2250 kg/m^3 were used to

produce CB NFs. Iron (II,III) oxide NPs [75] with a bulk density of 5240 kg/m^3 and SDS [76] with a bulk density of 1010 kg/m^3 were purchased from Sigma Aldrich. The chemicals were measured by percentage of mass using Sartorius CPA 324S balance. Tap water (chemical composition data in Appendix F) was used as a base fluid and weighted in a beaker before adding NPs and SDS. The samples were carefully stirred prior to the physical treatment in the sonificator, which was set for one hour for all the samples.

Figure 3.1: CB NPs (left) and IO NPs (right).

3.3 SEM and TEM characterization

SEM and TEM-images of the NPs used in the current study were obtained using electron microscopes at ElmiLab UiB. A ZEIZ SUPRA 55VP SEM with voltage range 100 V - 30 kV and magnification up to $1.5 \cdot 10^6$ was used to attain SEM-images. For TEM-images a JEOL 2100 TEM with magnification up to $1.5 \cdot 10^6$ and kV ranges of 80, 100, 120, 160 and 200 kV was used. The electron microscope study was performed in order to find the actual sizes of the NPs and give an idea of the agglomerates sizes formed in the NF. The results from this review can also be used for further study of the extinction coefficient mentioned in section 2.3.1 and other type of analysis where particle size is important.

Sizes of dry NPs were determined by use of TEM and SEM-images shown below, in addition to a range of images obtained in this study. A selection is supplemented in Appendix D.

CB NPs were found to be in the range of 15-95 nm by use of TEM and SEM-images shown in figure 3.2 and 3.5. The average particle size of CB was found to be 51.1 ± 17.0 nm by processing the pictures in the ImageJ software, see figure 3.4. The agglomerates in air were found to be in a range of 2.5-31.0 μm. The sizes of IO NPs, see figure 3.5 and 3.3, were proved to be larger than stated from the supplier. Sigma Aldrich reported IO NP sizes between 50-100 nm, but the size distribution analysis of SEM and TEM images in figure 3.4 revealed an average NP size of 184.4 ± 54.9 nm within the range 40-360 nm. Agglomerates detected in the TEM analysis were of sizes between 2.0 and 24.0 μm.

A NF sample made with 0.50 wt.% CB and 1.00 wt.% SDS was dried and viewed in a scanning electron microscope[1], see figure 3.6. The SEM image of CB shown in figure 3.5 and the SEM image of the dried NF with SDS presented in figure 3.6 show similar NP-sizes.

The results from the SEM and TEM analysis of the CB NPs are shown in an article submitted to *Applied Thermal Engineering*, see Appendix G.

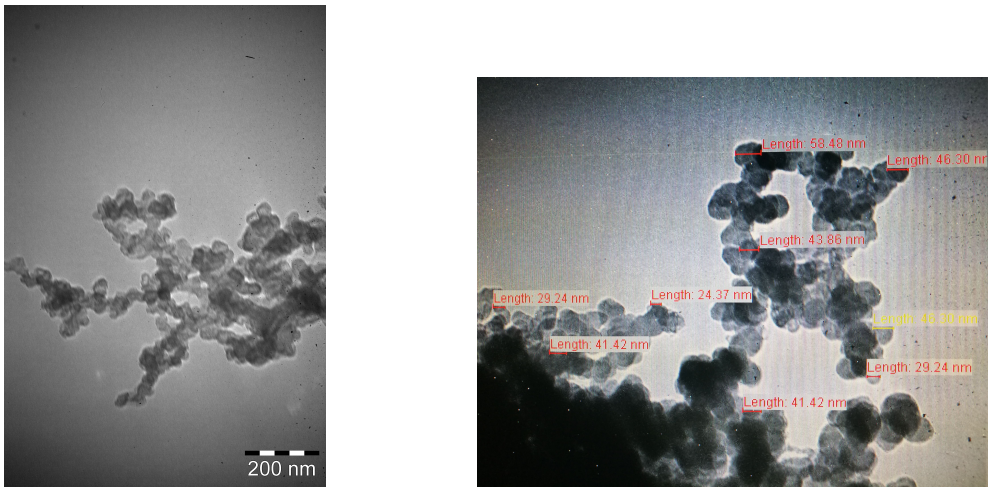

Figure 3.2: TEM pictures of CB NPs.

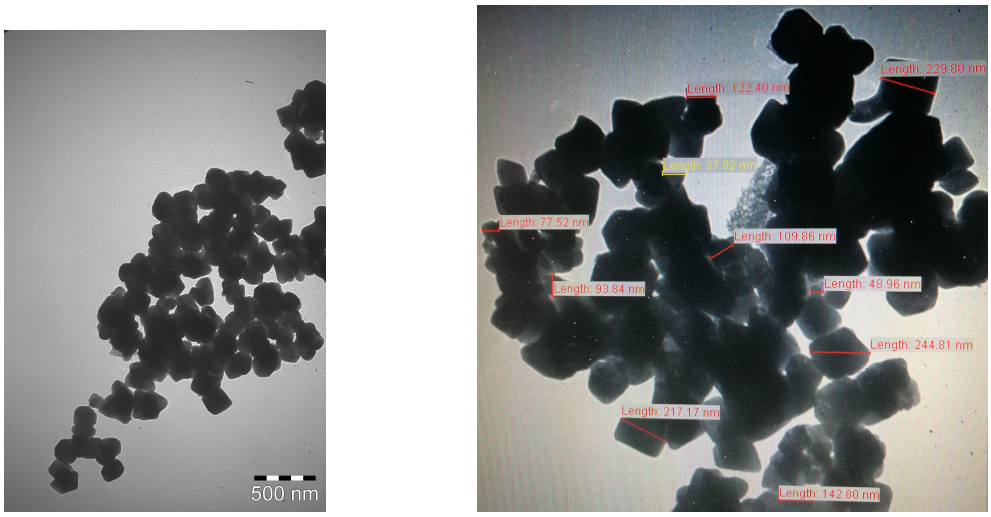

Figure 3.3: TEM pictures of IO NPs.

[1]Collaboration with Pittsburgh University.

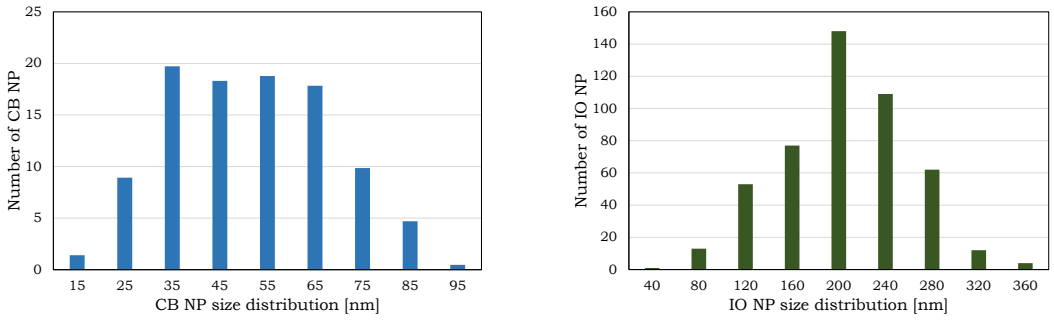

Figure 3.4: Size distribution of CB and IO NPs.

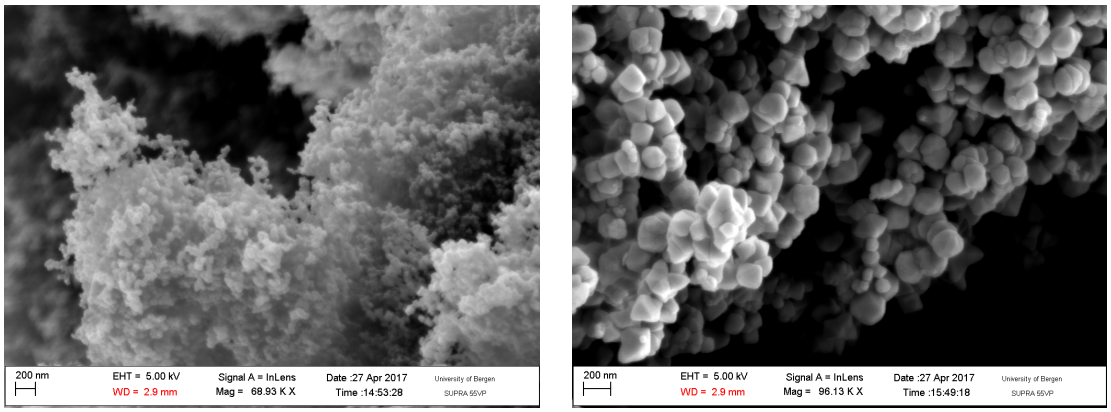

Figure 3.5: SEM pictures of NPs of 1) CB 2) IO.

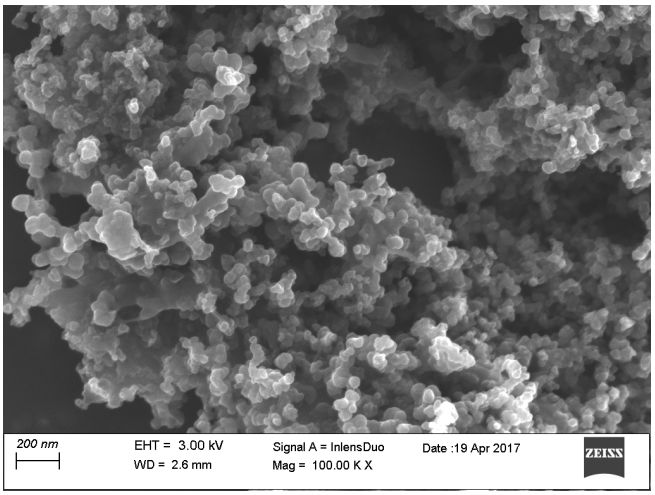

Figure 3.6: SEM picture of dried CB NF with SDS.

3.4 Developement of experimental setup

3.4.1 Temperature sensors

In the following sections, the response time (RT) is used as a measure of the reaction time of a sensor. The time a sensor in room temperature needs to reach 63.2% of the temperature in a dry-well or in water is called RT, denoted as τ [41, 77]. More details and the derivation of the time constant is shown in Appendix E.0.1.

In order to perform correct and reliable temperature measurements, a variety of temperature sensors was investigated. The RT of the different sensors in water and air was found through experiments presented as supplementary information, see Appendix E.0.2. Air RT measurements were conducted using a FLUKE 9102S dry-well fixed at 50°C and 80°C. Thermal RT of sensors from the room temperature to 50°C water was also investigated using a beaker on top of a heater. Water temperature was confirmed to be 50°C prior to RT measurements by use of additional thermometers.

A thermistor is a resistor sensitive to temperature changes [78]. A NTC-thermistor, see table 3.1, was first integrated into the experimental set-up. The first experiments revealed unreliable fluctuations in the recorded temperature as a result of high water vapour temperature. The sensor situated in the nanofluid showed stable measurements. The NTC-thermistor from Vishay in table 3.1 also malfunctioned when measuring the vapour temperature. To achieve reliable vapour measurements, a NTC-sensor with high temperature resistance was purchased from Vellemann, see table 3.1. RT of the thermistor can be found in Appendix E.0.2. Unfortunately, this type of thermistor could not handle the presence of water due to the exposed wires within the thermistor measuring resistance. This was seen as large temperature fluctuations out of range.

As the thermistors demonstrated poor accuracy, two types of thermocouples were tested. Thermocouples are used in a wide range of temperature measurement applications due to their extensive temperature interval [78]. They consist of two different metal wires joined at both ends. When one end of the thermocouple is heated, an electrical current starts to flow. A voltage will be produced and correspond to a certain temperature. A thermocouple can either consist of noble metals or base metals, where the latter is the most common. Type T, E, K, and J are made of base metals and R, S, C, and GB are noble metal thermocouples [78]. The main

Table 3.1: Relevant thermistor specifications from producer.

Thermistor type	**Response time air (s)**	**Temp. range (°C)**
NTC (low cost)	No data	−40 to +125
NTC (Vishay BCcomponents)	1.2	−40 to +125
NTC 135-104LAF (Vellemann)	4	−60 to +300

difference between the types is the temperature range.

Experiments to find the corresponding RT for relevant thermocouples were conducted. The RT for a T-type and a K-type thermocouple was tested with a HH506RA Multilogger Thermometer from Omega. The RT of the thermocouples can be found in table 3.2, calculated from the total time in figures found in E.0.2. The RT is measured from room temperature to air at 50°C, 80°C, and to water at 50°C.

The response times for both T-type and K-type were satisfactory, but RT performance of T-type was twice as high than of the K-type thermocouple in 80°C air. In addition, the error followed by using T-type is lower. Consequently, small T-type thermocouples with specification HTMQSSIM100G150 were purchased from Omega. The sheath material was chosen to be stainless steel (SS) due to its chemical compatibility. Of the three junction types available, exposed (E), grounded (G), and ungrounded (U), a grounded thermocouple was chosen, see figure 3.7. An exposed thermocouple has the shortest RT, but cannot be used in NFs due to the fully exposed metal wires. A grounded thermocouple was the preferred option considering its low RT compared to an ungrounded thermocouple.

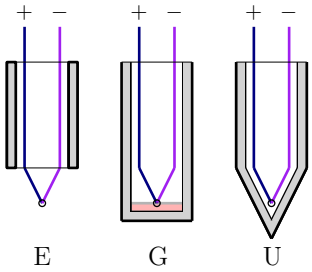

Figure 3.7: Thermocouple types: exposed, grounded, and ungrounded.

Table 3.2: Relevant thermocouple specifications found experimentally and collected from producer data*.

Thermocouple	$\boldsymbol{RT}_{\textbf{air 50°C}/\textbf{air 80°C}}$ **(s)**	$\boldsymbol{RT}_{\textbf{water 50°C}}$ **(s)**	**T-range*(°C)**
T-type (test)	68.3 / 32.2	4.4	−250 to +350
K-type (test)	55.0 / 65.2	1.9	−200 to +1250
T-type HTMQSSIM100G150	13.3 / 17.7	0.6	−200 to +350

3.4.2 Mass loss measurements

In each experiment mass change with time was recorded in LabView using Sartorius CPA 324S weight scale with an uncertainty of ±0.1 mg. A custom made stand was used to keep the NF situated above the scale in order to illuminate the entire NF from the bottom and on the sides, and at the same time to record the mass change of the vapour. The computer programme was set to record with a time step of one second (see figure 3.10 and figure 3.11 for illustration of the set-up).

It was desirable to measure both mass loss and temperature changes of the NF during illuminiation. However, in order to accomplish reliable mass loss measurements, it was not possible for the current set-up to measure temperature and mass change at the same time for each experiment. An experiment using 0.5 wt.% CB NF was conducted, but weight readings oscillated and showed numbers out of range. A cover was manufactured in order to protect the weight scale, but the thermocouples that were attached to the top of the NF tube and the wires that were connected to the multilogger thermometer had too much impact on the scale due to vibrations. The temperature sensors and extension cable were removed, leaving the evaporation tube from the cap to the condensation container. The measurements were also unstable. Therefore, all weight measurements were carried out separately for each NF concentration, doubling the number of experiments planned. The weight measurements were performed using an identical cap without temperature sensors.

3.4.3 Radiation source

There are various techniques to simulate solar light. Two halogen lamps of type Anslut 400 W / 230 V were used in the experimental set-up. The radiative heat flux I from the lamps was first estimated by use of temperature measurements at distance intervals from the glass on the lamps [79]. A ST-9215B thermometer from Yi Chun Electrics Co. with an accuracy of ±1°C was sprayed black for maximum absorption prior to temperature recordings. Each measurement was conducted for 10-15 minutes in order to stabilize recorded temperature. The amount of heat transferred to the area of the temperature sensor was found by applying the Newton's law of cooling (Eq. (2.2)) and the Stefan-Boltzmann's law (Eq. (2.1)) in a heat balance. The emissivity of the sensor was assumed to be 0.8 due to lack of prerequisite to find this. The radiative heat flux could then be calculated using the temperature measurements: $I = h_c(T_{sensor} - T_{amb}) + \sigma\epsilon(T^4_{sensor} - T^4_{amb})$. h_c was determined by the Nusselt number using Eq. (2.6) in section 2.3.1. The radiative heat flux against distance is plotted in figure 3.8. Figure 3.8 was used as an estimate to find an appropriate distance to get sufficient radiation to boil the NFs.

Natural convection arising from the heat of the lamps must be avoided when using the halogen lamps since the objective is to simulate solar light, see section 2.3.1. It was therefore important to position the sample outside the thermal boundary layer. By use of the equations in section 2.3.1, the boundary layer δ was found. The temperature of the glass of the lamp was measured using a K-type thermocouple, which was protected to avoid radiation affecting the temperature. The Grashof number was calculated from Eq. (2.4). Inserted in Eq. (2.5), the thickness of the

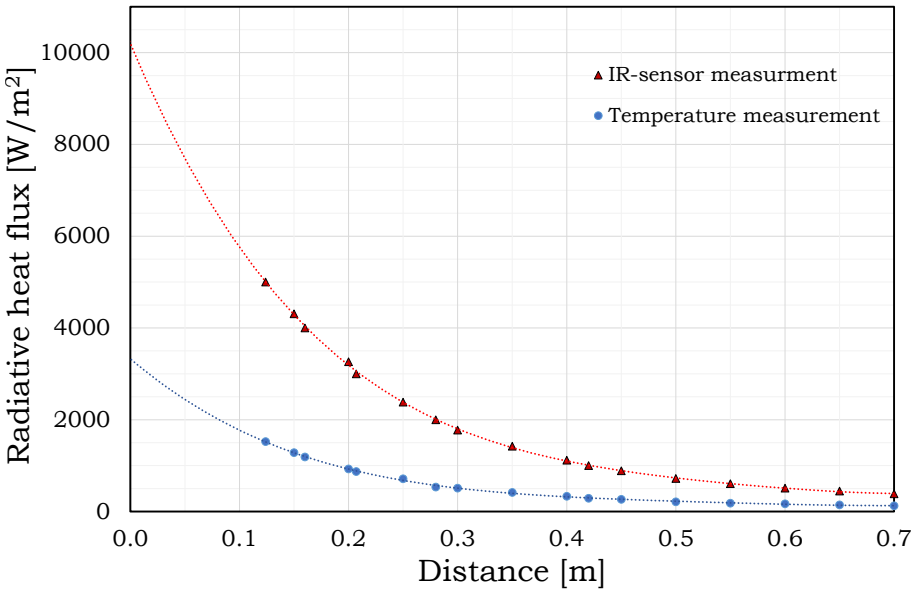

Figure 3.8: Radiative heat flux vs. distances away from the halogen lamp, measured using an IR-sensor, and found with temperature measurements and the Stefan-Boltzmann's law.

thermal boundary of layer was found to be 0.976 cm. This value is relatively small so that samples can safely be placed at distances from the lamp exceeding 1 cm.

To get a better estimation of the radiation from the lamps, an infrared(IR)-sensor of the type radiometer LS122IR from Linshang was used. The IR-sensor was calibrated using a Oriel Sol3A solar simulator at Bergen University College. The measurements were conducted with the sensor facing the center of one lamp at different distances parallel to the beam. Measurements closer than 12.4 cm were outside the sensor range, and the data was extrapolated using a fourth order polynom, see the measurement results in figure 3.8.

The distance of 10 cm was decided to be used in the experimental set-up, by using two lamps so that the light beam from lamp 1 was perpendicular to the light beam from lamp 2. This led to boiling of CB NF within a time frame of 5-8 minutes. According to the IR-sensor graph in figure 3.8, a 10 cm distance corresponds to a radiative heat flux of 5759.7 W/m^2 (5.56 sun). The latter data was used to define the radiative heat flux in this work.

It was essential to know in which degree the wavelengths from the lamps correspond to the solar spectrum. Measurements of the lamp spectrum were made with a Ramses AAC-VIS radiometer from TriOS in order to verify the wavelengths. The radiometer had a spectral accuracy of ± 0.2 nm. In figure 3.9 the spectrum obtained with the radiometer is compared with data received from Osram [80] and the solar spectrum obtained from AM 1.5 standard spectrum ASTM G173-03 [81].

The Ramses radiometer detects radiation within 280-950 nm and therefore cannot deliver data corresponding to the entire solar spectrum in the range from 250 to 2500 nm. However, both Ramses measurements and data from Osram indicate a shift of approximately 350 nm to the right of the solar spectrum. The lamps will therefore not radiate the same amount of short wavelength radiation from 280 nm to

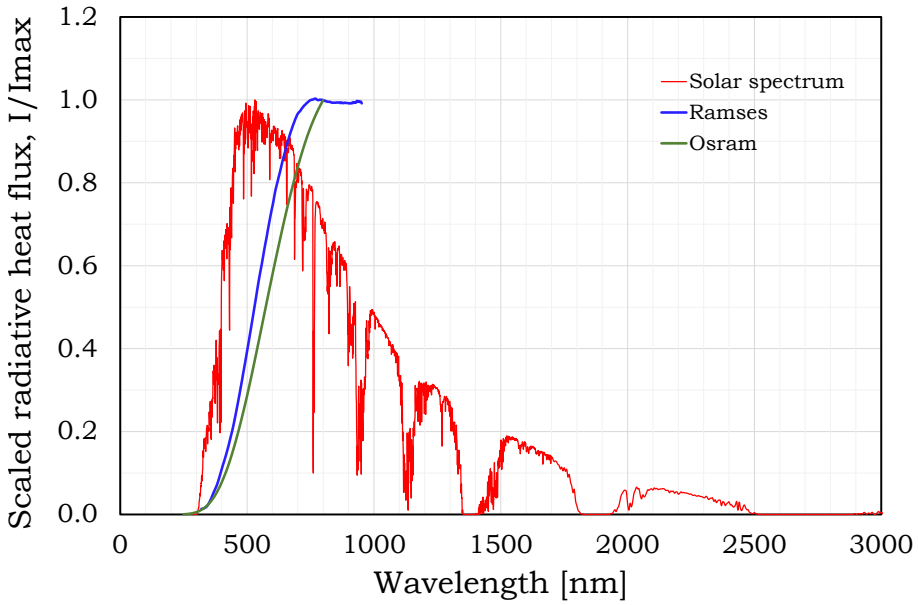

Figure 3.9: Solar spectrum compared with Osram data and measurement by use of Ramses radiometer.

about 650 nm, but deliver mostly infrared radiation (700-1050 nm). By numerical integration of the solar spectrum and the Ramses graph in figure 3.9, it is found that the halogen lamps radiate only 52.5% of the short wavelength radiation illuminated by the Sun. This was determined from 280 nm to the intersection between the solar spectrum and Ramses measurements.

3.5 The experimental set-up

As mentioned in the previous section, the experimental set-up included two halogen lamps located 10 cm from the NF sample, see illustration in figure 3.11. Separate experiments to measure mass loss and temperature data were conducted. The same NF samples were used in the set-up in order to merge results from two experiments to produce efficiency data. In this work it was assumed that the experiments for each concentration with regard to temperature and mass loss were identical, but the error caused by this assumption must be emphasized. There were two main differences between the temperature experiments and the weight experiments. The most important difference was the presence of temperature sensors made of stainless steel, see figure 3.10, since this will decrease the boiling time of each NF. The sensor will become hot as it absorbs the thermal radiation, and by heating the surrounding fluid it will have an impact on the boiling. To collect vapour for Raman spectroscopy, a plastic tube was attached from the outlet bringing the condensate to a small container. This additional geometry will give a minor increase in pressure for temperature experiments. Further analysis of the experimental errors can be found later in section 4.6.

The T-type thermocouples were attached to the lid of the NF tube and located in the middle of the solution at the distance 13.1 cm from the top of the lid, as sketched in figure 3.10. The thermocouple recording vapour temperature was located 2.2

cm from the top and protected by aluminium and white fabric outside the tube to avoid additional radiation affecting temperature readings. Condensed vapour was collected in all temperature experiments from the outlet on the top of the tube and to a container as depicted in figure 3.11. The duration of each experiment was at least 30 min in order to get valuable data for the boiling process.

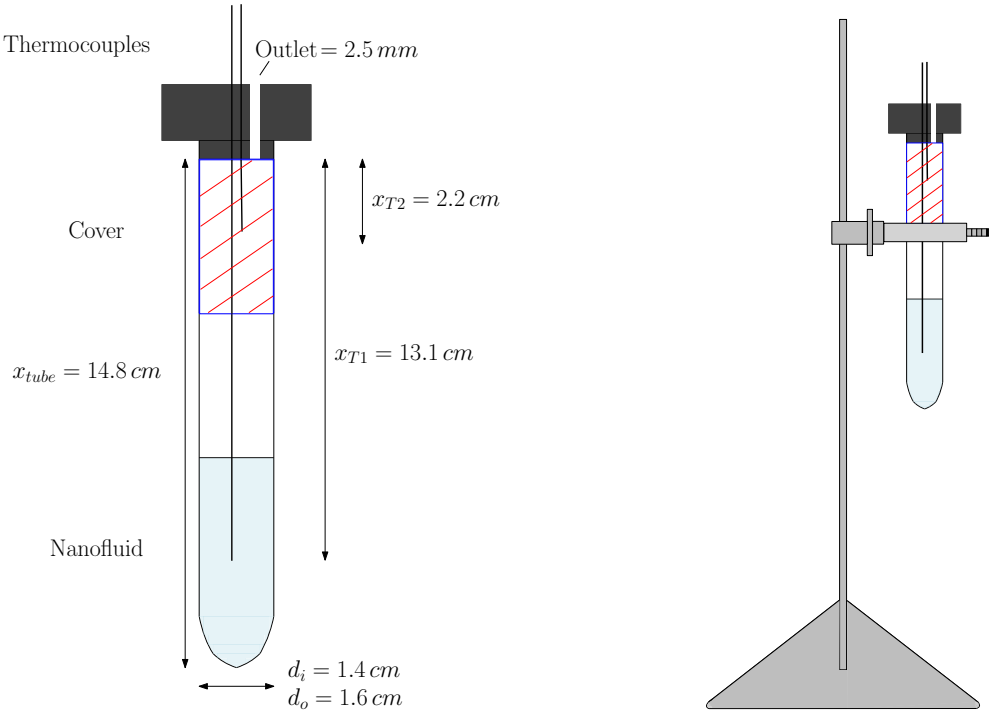

Figure 3.10: Left: NF tube with two temperature sensors (sensors are not included in the weight measurements). Right: NF tube in custome made stand.

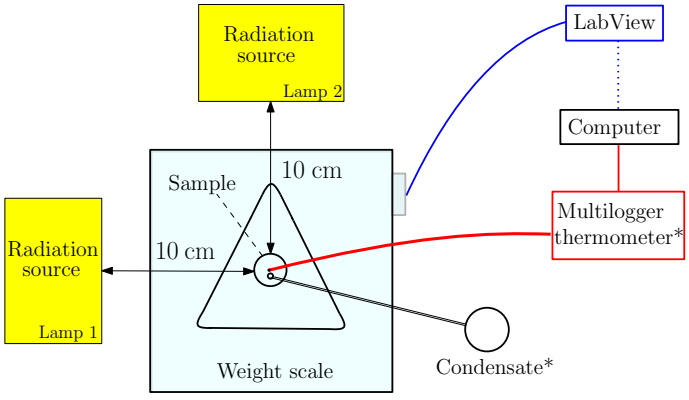

Figure 3.11: Schematic representation of experimental set-up in horizontal plane. Components marked with * are not included in weight experiments.

3.6 Energy conversion

Two types of efficiencies are defined and used in this work: absorption efficiency and vapour generation efficiency. All three models depend on the total incident solar radiation explained in the next subsection.

3.6.1 Total incident thermal radiation

In order to produce reliable efficiency data it is important to estimate the magnitude of radiation received by the NF. The total incoming radiation is defined as $\dot{Q}_{rad} = I\,A$, where I is the radiative heat flux. As described in section 3.4.3, the radiative heat flux equals 5759.7 W/m^2 at a 10 cm horizontal distance from the lamp.

To calculate the total incoming radiation on the NF, the absorption area A must be defined. Heat absorption will both occur on the surface of the test tube and inside the NF. In the latter case, the total area is based on how far deep the NF absorption takes place, which is dependent upon multiple variables as type of NF, concentration, agglomeration and location of the NPs with respect to time. The complexity of this task lies beyond the scope of this thesis and the absorption which takes place within the NF is therefore neglected.

In previous works [15, 17] the absorption area was assumed to be either the area of a lens which concentrates the sun light or the cross section of the receiver. In the present study, the radiation area was chosen to be the cross section as illustrated in figure 3.12 B. As a result of the simplified radiation area, errors will exist in the calculation of efficiency. For example the radiation beam has to travel longer on the edges of the tube and the reduced radiative heat flux at these points is therefore not accounted for. When light passes through the air and enters the glass tube, the light beam slows down due to density differences and causes a bending, that will affect the absorption area. In addition, the tube wall is circular, which causes some of the incoming radiation to reflect and scatter in different directions (see sketch A in figure 3.12). The latter is not considered in the simplified model.

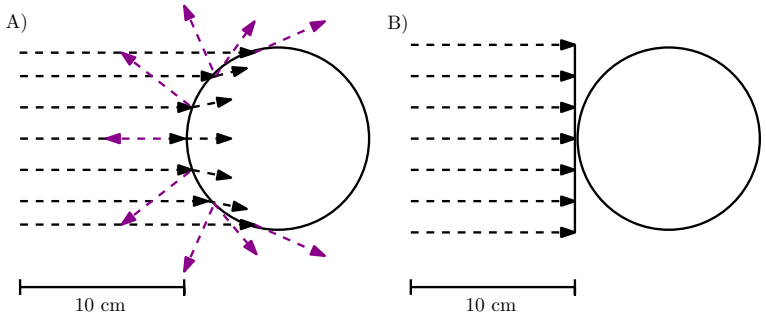

Figure 3.12: Cross section of tube from above with radiation entering from the left. A) Reality B) Simplified model

When the NF have reached the boiling point, mass loss due to evaporation will reduce the height, which leads to a smaller radiation area. However, due to NPs ability to stick to the glass tube, the reduction may be lower.

Considering all the aforementioned assumptions challenging, in all the efficiency calculations of current work the radiation area is treated as a constant. An extra uncertainty appears due to this reason.

3.6.2 Absorption efficiency

The absorption efficiency, η_{abs}, describes the energy needed to bring the NF to the boiling point scaled by the total irradiation energy transferred to the fluid: $\eta_{abs} = Q_{abs} \,/\, Q_{rad}$. For a transient process in which the parameters are not constant, this can be extended and solved numerically [17]:

$$\eta_{abs} = \frac{\int_{T_0}^{T_1} m\, C_{NF}\, dT}{\int_{t_0}^{t_1} I A\, dt}, \tag{3.1}$$

where C_{NF} is specific heat capacity of the NF and dT corresponds to the temperature change within the NF for each time step dt. Eq. (3.1) is integrated from the start of the experiment, $t = t_0$, until the boiling point has been reached at the time t_1. This corresponds to the start temperature at T_0 and the final boiling temperature T_1. Mass of the fluid, m, is often treated as a constant by reason of the limited mass loss during the absorption process, but in this thesis it is taken into consideration. In addition, C_{NF} is calculated for each time step using the mass fractions f: $C_{NF} = C_{H_2O} f_{H_2O} + C_{NP}(1 - f_{H_2O})$. The density of the NF used for radiation area calculations is given by: $\rho_{NF} = \rho_{H2O}\, m_{H2O} + \rho_{NP} m_{NP} + \rho_{SDS} m_{SDS}$ where m denotes the mass and ρ the density of the respective species. In this work a heat capacity of 462 J/(K·kg) [82] was used for IO and 710 J/(K·kg) for CB NPs. As mentioned in section 2.3.2, the effect NPs bring to the heat capacity of water is not yet known [53]. The equation for C_{NF} will therefore be an estimate. The heat capacity of SDS is not taken into account as its amount was too low to have an impact on the results.

3.6.3 Vapour generation efficiency

In this work the vapour generation efficiency is defined as the enthalpy change after the boiling point has been reached, scaled by the total incident solar radiation $\eta_{vap} = Q_{vap} \,/\, Q_{rad}$. The enthalpy change considers the phase change energy and additional energy to superheat the vapour. Developed from the heat equation for vapour generation in section 2.3.2, and the heat increase within the vapour with regard to the specific heat of vapour, the vapour generation efficiency becomes:

$$\eta_{evap} = \frac{\int_{m_0}^{m_1} \big(h_{fg} + C_{ps}(T_{vap} - T_{sat})\big) dm}{\int_0^t I\,A\,dt}, \tag{3.2}$$

where m is integrated over the mass of the vapour produced when boiling commences from the initial mass m_0 to the final mass m_1, and h_{fg} is the latent heat of vaporization of water at 1 atm. After the NF has reached the boiling point and evaporated, the generated steam will undergo a change in its internal energy. The increase in vapour temperature is based on the specific enthalpy property of the fluid, see section 2.3.2. The heat capacity of the steam C_{ps} used in Eq. (3.2) is 1860 J/(K·kg). T_{vap} is the vapour temperature after boiling commences, T_{sat} is the saturation temperature, and dm is the mass change of the steam exiting the NF tube.

As described in section 2.3.2, latent heat of vaporization is temperature dependent and in which manner the NPs effect the values of latent heat is still not fully identified [53]. For that reason h_{fg} is treated as a constant for transient efficiency calculations. The heat captured by the NF is assumed to be proportional to the mass of water in the NF. The mass fraction of water for all NF concentrations is therefore added to the numerator in the calculation of vapour efficiency. Like heat capacity and latent heat of vaporization, the temperature and NP dependency of specific enthalpy of steam were not taken into consideration due to complexity and lack of reported values.

4. Results and discussion

4.1 Overview

This chapter presents experimental results on the use of CB and IO NFs as a direct solar absorber. This is illustrated in figure 4.1. The optimum concentrations of CB and IO NFs related to boiling time, evaporation ratio, vapour temperature, absorption and vapour generation efficiency are shown and analysed.

In between the experiments with CB and IO, the thermocouples had to be replaced. As mentioned in section 3.5, the thermocouple in the NF slightly affects the boiling time and it is therefore essential that the thermocouple is located at the exact same position for each experiment. The measurements from the thermocouple which recorded vapour temperature were affected by sensor elevation above the NF surface. This was due to the temperature distribution formed above the NF. Since the thermocouples had to be replaced, the results of boiling NFs with CB and IO cannot be entirely compared. Additional experiments using the most efficient concentrations of NFs were therefore conducted and are shown as a final result. Further, condensed vapour was collected and examined in order to investigate whether NPs contaminate the generated vapour.

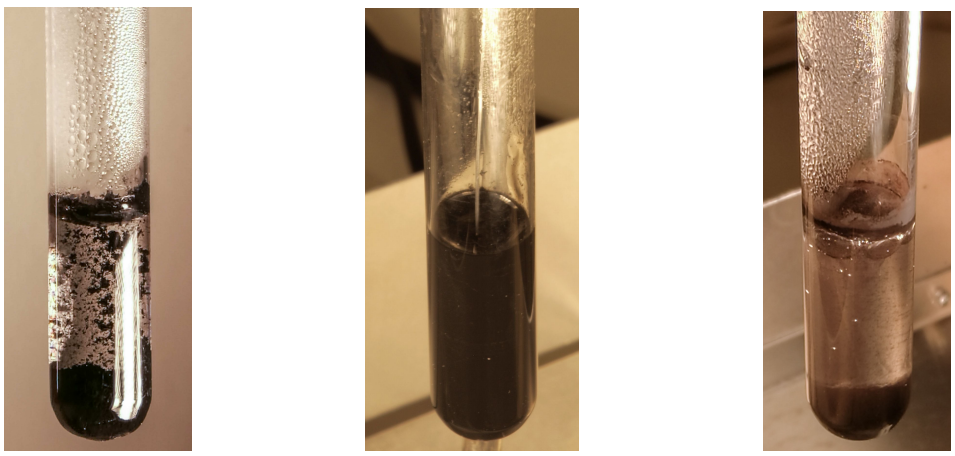

Figure 4.1: Convection in NFs: 1) CB without SDS, 2) CB with SDS, 3) IO.

4.2 Boiling carbon black nanofluids

Constructing the lab set-up required several attempts in order to find the appropriate distance from the illumination source to the sample, and the desired sample volume. The objective was to achieve a distance that initiated boiling of the NFs.

The initial experiments showed that the onset of boiling occurred at around 100°C for NFs with a concentration less than 2.00 wt.% CB. After visual boiling of 3.00 wt.% CB NF, 31 seconds elapsed before the NF temperature reached 100°C, which is a significant delay. By the boiling of 4.00 wt.% CB, the sensor used several minutes until 100°C was detected. For higher concentrations than 4.00 wt.% CB NF the temperature values never reached 100°C. This can be explained by boiling in outer areas of the sample due to NPs blocking the radiation. It is therefore likely that there exist larger temperature gradients throughout the sample for higher concentrations of CB. The NF temperature had to be stable in order to declare the boiling point. Therefore, the temperature change for each time step was studied for all experiments in order to define the boiling point at stable temperature values.

The following section contains experimental results from boiling CB NFs with tap water as base fluid. Nine CB NFs without SDS and five CB NFs with 1.00 wt.% SDS were prepared and illuminated in the final experimental set-up (explained in section 3.5). The concentrations were in the range of 0.10-10.00 wt.% CB. The NF samples were sonificated for one hour in order to break agglomerates formed in suspension.

The experimental data consisted of 70 temperature and weight measurement studies, where 22 experiments involved samples containing SDS. The data collected is the basis of the plots presented in the next subsections. Each NF sample of 5 g was radiated during a period of 30 minutes, corresponding to a radiation of 5.76 sun from a single lamp. All experiments were conducted by the use of initially cold halogen lamps and room temperature varying from 23 to 25°C. Every NF concentration was investigated in a minimum of four experiments: two temperature and two weight experiments. If the percent difference between two results exceeded 5 %, new experiments were conducted. In some results the uncertainty calculations exceeded this limit. An uncertainty analysis can be found in section 4.6.

Figure 4.2 displays an example of the boiling of a 0.50 wt.% CB NF sample. In the figure it can be seen that NF temperature increases until steady boiling commences at 100 °C. The air over the NF is heated up by convection as the NF temperature increases until the boiling point. Next, vapour temperature remains constant until a certain point at which the temperature shows a marked increase. This is similar for all the CB NFs, see Appendix B. The reason for the sudden increase in vapour temperature measurements for CB NFs could be due an increase in concentration after a period of boiling. A higher concentration leads to a reduction of distances between the NPs, which initiates excessive heating of the water. Also, this could indicate that in the period where the vapour temperature is constant at 100°C, boiling does not occur in the entire bulk fluid, as mentioned in section 2.4.2.

In the secondary axis in figure 4.2, mass loss with respect to time shows initiation of evaporation when the NF reaches its boiling point and presents continuous boiling. Temperature and mass loss figures for all concentrations can be found in Appendix B.

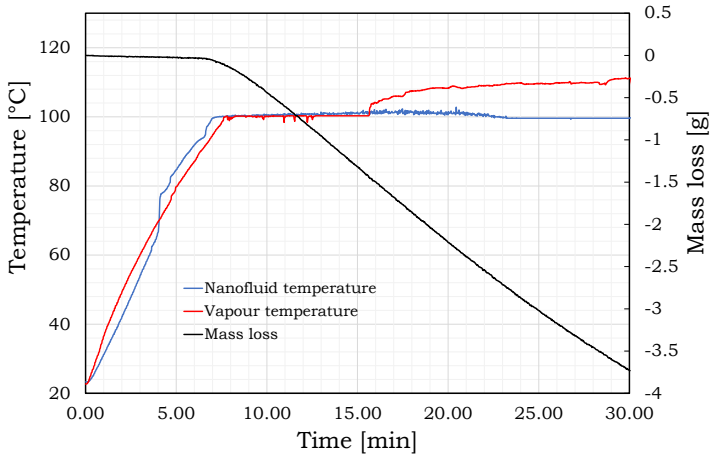

Figure 4.2: Boiling of 0.50 wt.% CB NF.

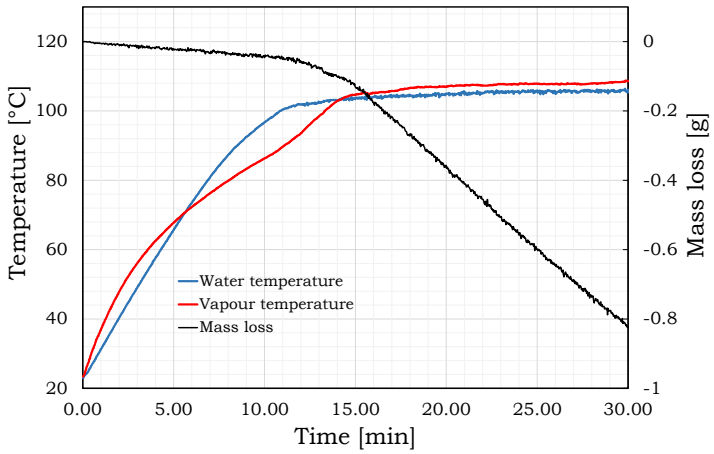

Figure 4.3: Boiling of tap water.

It was also interesting to investigate a case when only water (without NPs) was illuminated. The results are presented in figure 4.3. The time until boiling of water occurs is considerable longer than for CB NF samples. The temperature of the vapour increases slowly and the maximum temperature is lower for water than for CB NFs. The vapour temperature reaches a maximum of 108.8 °C and the mass loss is low compared to figure 4.2.

For the cases where concentrations were below 3.00 wt.% in CB NFs without surfactant addition, the NPs deposited to the bottom at the beginning of each experiment, see figure 4.1. As the temperature of the NF increased by convection, the NPs were put into motion. When boiling commenced the NF was fully homogenized. For higher concentrations the NF was very viscous and generated no visual precipitation, see figure 4.4 for illustration.

By the reason of the increased viscosity for concentrations higher than 2.00 wt.%, the sample collection was more difficult. SDS will only efficiently suspend NPs in dilute

liquids and for that reason it was decided not to perform experiments on samples containing SDS for concentrations higher than 3.00 wt.%.

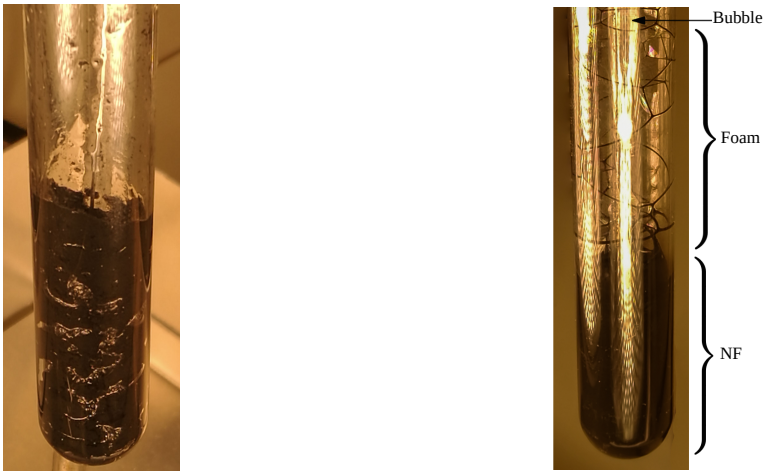

Figure 4.4: Left: Boiling of 5.00 wt.% CB NF. Right: Boiling of 0.50 wt.% CB NF with SDS.

4.2.1 Temperature analysis

Figure 4.5 displays a summary of the boiling time for all CB NFs. Boiling was visible in all samples. The time until the NF had reached saturation is plotted for all concentrations and presents a curve with a minimum boiling time in the range 0.50-3.00 wt.% CB NF. Tap water (not shown in figure 4.5) reached 100°C after 10.99 ± 0.16 min which confirms enhanced boiling for all concentrations of CB. Boiling was not detected in any of the experiments with pure tap water. As mentioned above, the explanation for the quick boiling of the CB NF concentrations in figure 4.5 is most likely due to an increased area of light absorption. On the other hand, for NP concentrations exceeding 3.00 wt.%, the time until boiling increases, which indicates that the light does not penetrate the NF in an optimum manner due to a decrease in absorption area.

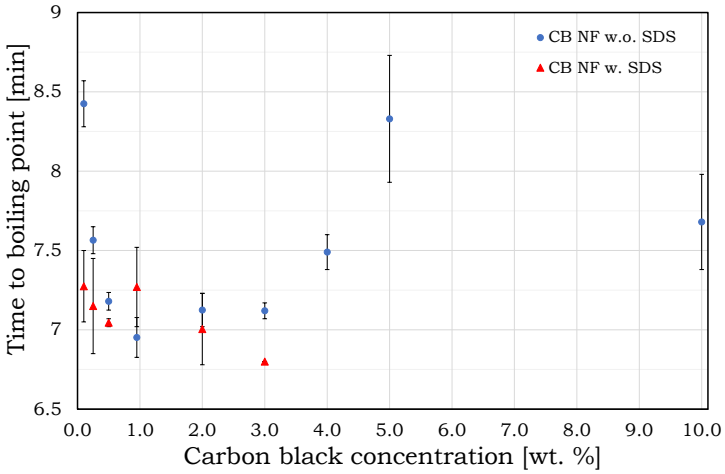

Figure 4.5: Time to reach the boiling point plotted against CB concentrations.

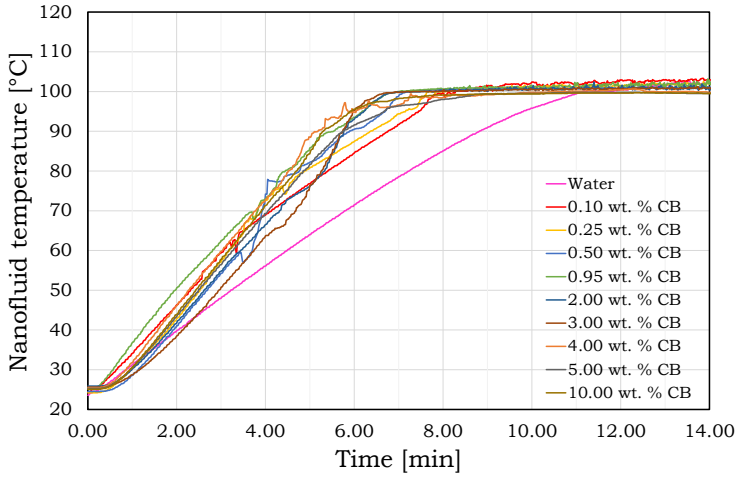

Figure 4.6: CB NF temperature as a function of time.

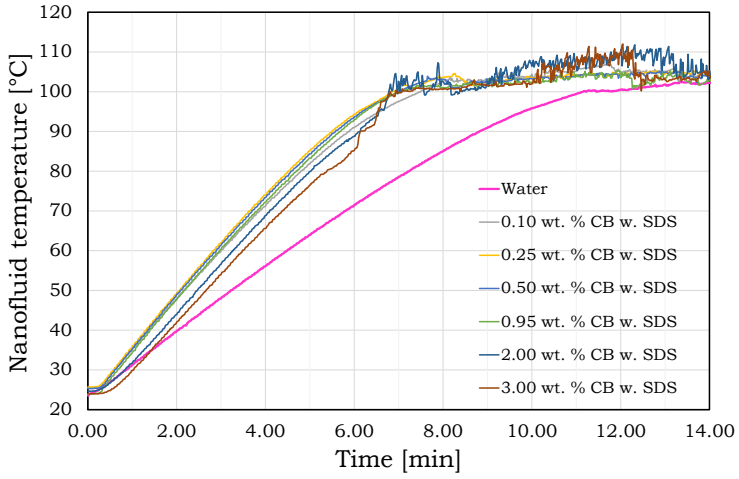

Figure 4.7: CB NF temperature containing SDS as a function of time.

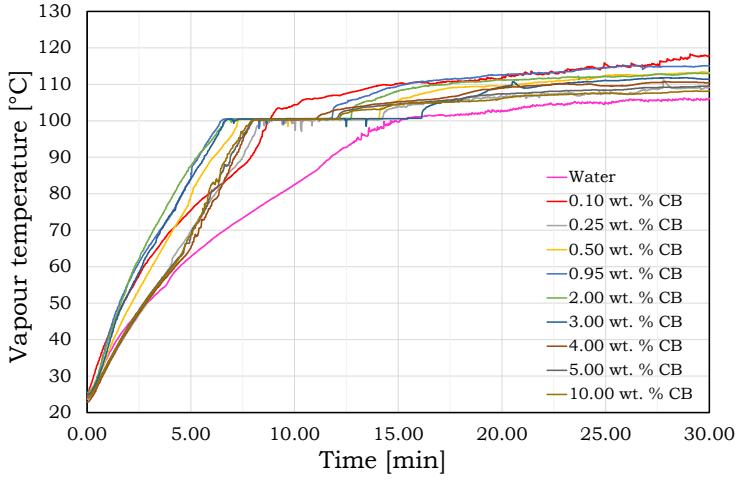

Figure 4.8: CB NF vapour temperature as a function of time.

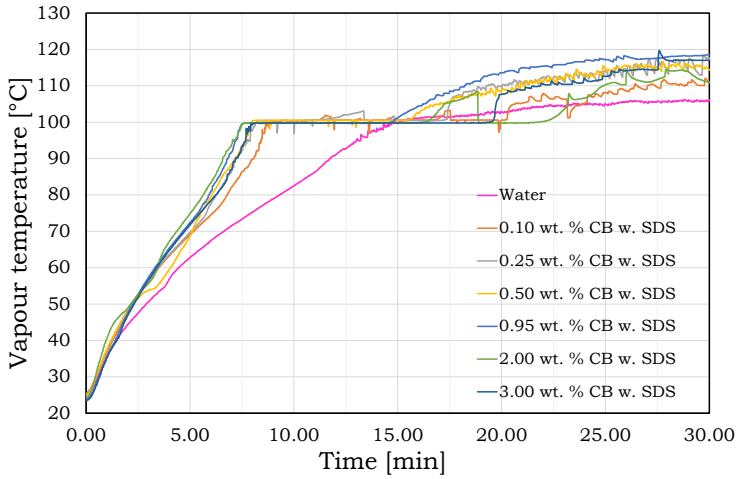

Figure 4.9: CB NF vapour temperature containing SDS as a function of time.

The temperature with respect to time of water and CB NFs for different concentrations without SDS is shown in figure 4.6. Figure 4.7 presents the temperature of water and CB NF containing SDS from the onset of illumination until steady boiling begins. The NF containing SDS shows oscillating tendencies in the temperature after the boiling point has been reached. This can be explained by the boiling occurring when SDS is present in the NF, see figure 4.4. Surfactant additions causes a reduction in surface tension of the NF, generating foam when boiling is initiated [83, 84]. Big soap bubbles boiled upwards in the test tube, inducing visible vibration on the thermocouple situated in the NF. Figures presenting the entire illumination period can be found in Appendix B. In some of the figures the thermocouple recording NF temperature detects values up to 140-150 °C. In these cases the NF had boiled off just beneath the sensor, and radiation strikes the thermocouple directly. Furthermore, the unsteady boiling of CB NFs with SDS could in periods cover the sensor, and present a more accurate temperature.

In some cases, the NF bubbles reached the second thermocouple recording vapour temperature, which can be seen in figure 4.9. Residue of NPs were seen at the tube wall exiting the NF tube for all samples containing SDS. We return to this issue in the next section, where a condensate sample analysis is presented and discussed.

The maximum vapour temperature of all CB samples is plotted in figure 4.10. It is clear that the vapour temperature of CB NF samples containing SDS is higher. The surfactant addition causes a better suspension of particles, and thereby the absorption area increases. Comparing the figure with maximum vapour temperature of water at 107.5 °C $\pm$ 1.3, an increased effect of CB NP additions is demonstrated. However, a reduction in vapour temperature appears for CB NF concentrations over 3.00 wt.%. For high NP concentrations, the particles are so closely packed that light will only radiate the outer layers of the volume, which will lead to an inefficient absorption and vapour generation process.

Figure 4.11 shows the NF temperature of all samples and was plotted to verify overheating existing in each concentration of CB NF. The data was averaged from the individual boiling points. Compared to water with an average temperature of 104°C $\pm$ 0.50, the results show some overheating within NFs containing SDS and NFs

less than 0.95 wt.% CB without surfactant addition. With increased concentration the NF temperature decreases, which refers to the fact that boiling occurs in outer layers of the NF sample. The high water temperature and dilute CB NFs ($\geqslant 0.95$ wt.%), especially the ones without surfactant addition, can be explained by heating of the temperature sensor due to directly incident radiation.

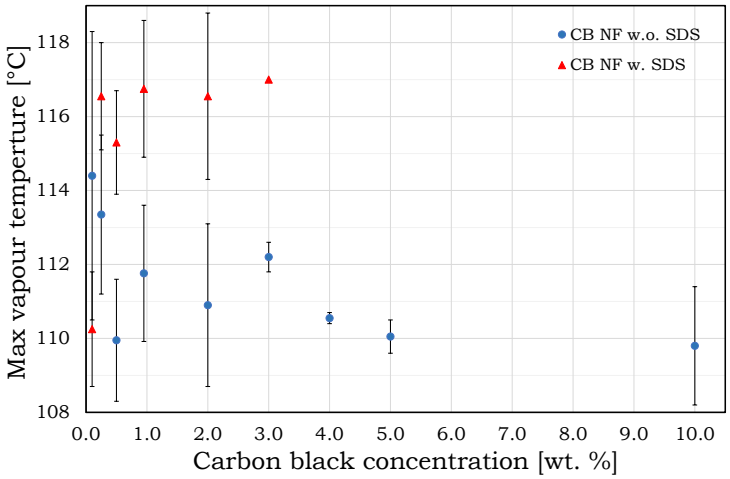

Figure 4.10: Maximum vapour temperature as a function of CB NF concentration.

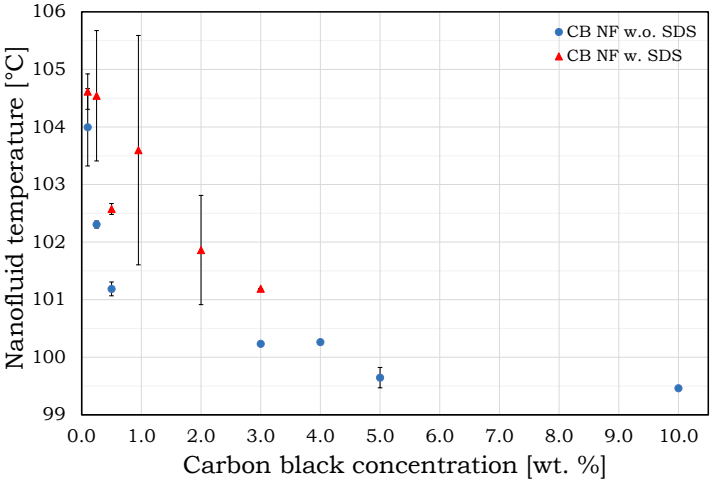

Figure 4.11: Average NF temperature as a function of CB NF concentration.

4.2.2 Mass evaporated

Prior to and by the end of each experiment, the NF weight was measured manually using a separate weight scale. The measured weights were then compared with the mass loss data using the Sartorius weight scale and LabView. The reliability of the Sartorius scale was shown to be creditable and was far within the maximum error of 5.00%. The mass loss data from each experiment was compared by calculating the evaporation ratio. This measure is defined by the mass of the NF evaporated scaled by the total amount of mass in the sample prior to illumination.

Due to the difficulty in definition of the exact boiling point by use of temperature measurements, the evaporation ratio is considered to give one of the most reliable and

revealing data to determine the most efficient NF concentration. Furthermore, the evaporation ratio is an important measure when it comes to the vapour generation process in a DASC.

Figure 4.12 presents the evaporation ratio of each CB NF. The most efficient concentration with regard to evaporation was 2.00 wt.% CB NF. Real time data for weight experiments with CB NF containing SDS were shown to be unreliable due to unsteady measurements. The boiling caused small bursts of NF streaming out of the outlet on top of the tube, which led to oscillations in mass measurements. The evaporation data in figure 4.12 was therefore determined by the difference in weight measured before and after the temperature experiments, where the vapour was directed by a tube to the condensate chamber. The figure shows no clear indication that addition of SDS has an impact on the total evaporation ratio of CB NFs. Water, which is not represented in figure 4.12, showed low evaporation ratio of 0.18 ± 0.01. The increase in evaporation ratio with increased concentration is connected to the absorption of the incident radiation. Figure 4.12 should therefore show a similar behaviour as the boiling time in figure 4.5. In addition, the absorption efficiencies and vapour generation efficiencies for CB NFs shown later should also correlate with the evaporation ratio and boiling time.

Figure 4.13 presents mass loss for all concentrations of CB without SDS. CB concentration of 2.00 wt.% and 3.00 wt.% are shown as the most efficient concentrations.

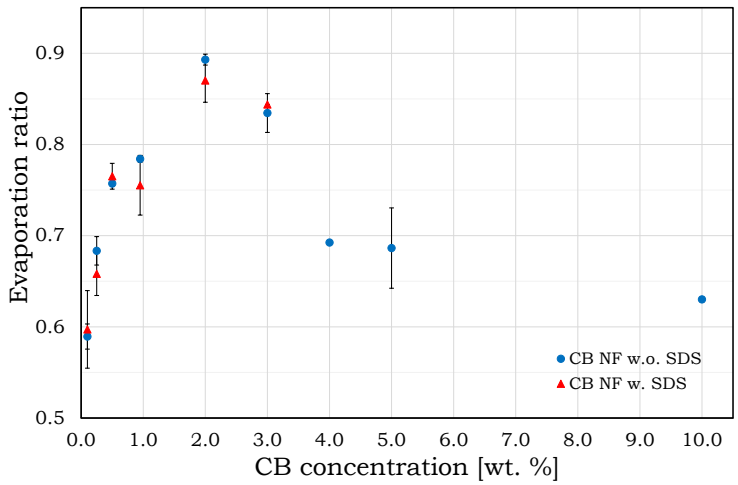

Figure 4.12: Evaporation ratio as a function of CB NF concentration.

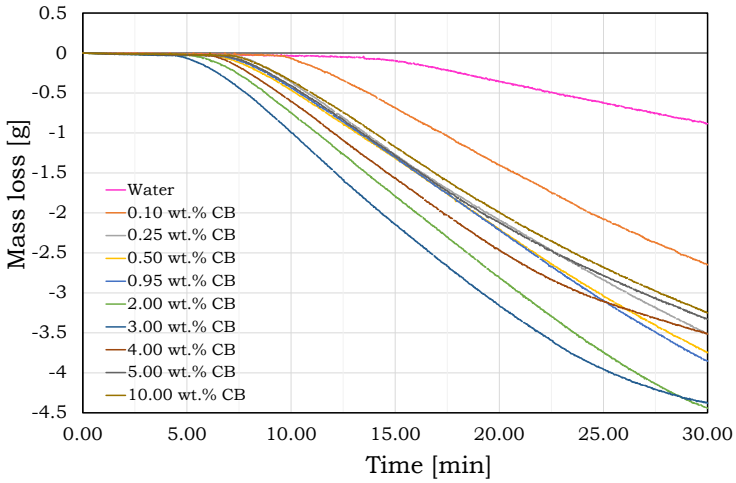

Figure 4.13: Mass loss as a function of time. Boiling of CB NFs without SDS.

4.2.3 Efficiency

The absorption and vapour generation efficiencies, discussed before, were computed based on temperature and weight experiments of CB NFs.

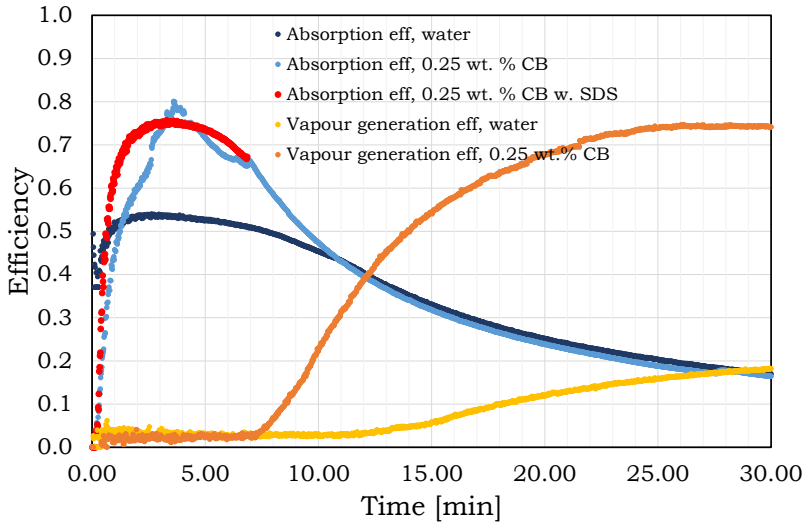

Figure 4.14: Absorption and vapour generation efficiency for water and 0.25 wt. % CB NF as a function of time.

Absorption efficiency

Eq. (3.1) was used to determine the absorption efficiency by numerical integration. Figure 4.14 presents the efficiency with time for water and NF containing 0.25 wt.% CB. The absorption efficiency of 0.25 wt.% CB NF has an absorption peak seen at all CB NF absorption efficiencies. This peak indicates a point in time when the distribution of the NPs are at its optimum, expanding the area of absorption. This

is explained by an increased convective heat transfer as a result of temperature differences in the NF, inducing a favourable NP dispersion within the bulk fluid. The CB NF continues to absorb incident radiation, but when the boiling point has been reached this energy is used to break hydrogen bonds between water molecules, and a vast reduction of all CB NF absorption efficiency curves is observed.

Absorption efficiency corresponding to the boiling of CB NFs with SDS shows the same tendencies as the absorption efficiency of water, see figure 4.14. Nevertheless, for CB NFs without SDS, the absorption curve has a well-defined maximum. The reason for the rapid increase in efficiency could be due to increased NP homogenization in CB NFs with increasing temperature. For samples containing SDS, the NPs are suspended in the solution from the beginning of the process, which will cause a smoother efficiency curve.

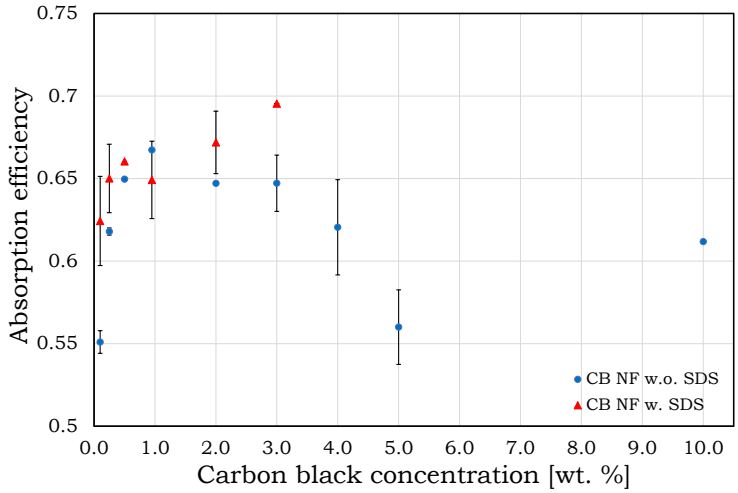

Figure 4.15: Time-averaged absorption efficiency as a function of CB NF concentration.

Absorption efficiency data is compared by a time-averaged value, which is calculated by the mean using the efficiencies for each time step until the boiling point. Time-averaged absorption efficiency for water was 0.43 ± 0.01. The NP addition displayed in figure 4.14 increases the time-average absorption efficiency of water by 29%. By only adding 0.10 wt.% CB the time averaged absorption efficiency increases by 21%.

Time-averaged absorption efficiencies with respect to CB NF concentrations are presented in figure 4.15. The figure illustrates enhanced absorption of CB concentrations in the range 0.50-3.00 wt.%. The absorption efficiencies of CB NFs containing SDS was calculated using a constant mass criteria due to the unreliable weight measurements mentioned in the previous subsection. The improved absorption of the NF concentrations in figure 4.15 is due to an increase in absorption area. In other words, light penetrates the NF and more NPs actively participate in the heat absorption process, which leads to a greater amount of energy transferred to the surrounding water. With further increase of NP concentration, the NPs in the outer layers of the sample will block the radiation from penetrating the sample, and the area of absorption decreases.

Vapour generation efficiency

The vapour generation efficiency was calculated using Eq. (3.2). The first term in the nominator describes latent heat and the second term represents the entropy increase of the generated vapour. Of the two terms, the contribution of latent heat is superior. By separating the two terms, the efficiency corresponding to the temperature increase in the vapour would only provide an additional gain in the order of 10^{-3}. The latter illustrates that a large amount of energy is required to break hydrogen bonds between water molecules compared to the energy used to increase the enthalpy of the vapour.

The efficiency curve in figure 4.14 starts at zero and increases when boiling commences due to evaporation. This is typical for all vapour generation efficiency curves observed in this study. If the NF evaporated completely and the residue consisted of NPs only, the vapour generation efficiency curve maximizes to an efficiency of 1. This can be explained by the assumed absorption area described in section 3.6.1. For a volumetric absorber, the real absorption area is greater than the cross section of the tube, which leads to higher efficiency data presented in current thesis. Since the cross section is used in this thesis, the efficiency data presented is larger than the actual efficiencies.

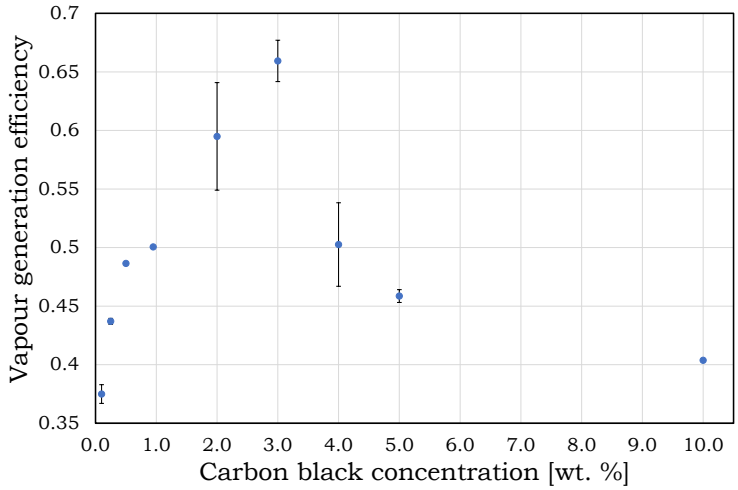

Figure 4.16: Time-averaged vapour generation efficiency as a function of CB NF concentration (no SDS added).

Similarly to the absorption efficiency, vapour generation efficiency data in figure 4.16 was determined by the time-average. Figure 4.16 reveals increased vapour generation efficiencies for CB NFs with no SDS addition up to 2.00 and 3.00 wt.% CB where 3.00 wt.% was the most efficient. Compared to water with a vapour generation efficiency of 0.08 ± 0.00, all CB NFs are superior. Due to unreliable weight measurements of CB NF containing SDS mentioned in section 4.2.2, efficiencies corresponding to SDS addition are not included in figure 4.16.

The results from the boiling of CB NPs are shown in a paper submitted to *Applied Thermal Engineering*, see Appendix G.

4.2.4 Summary

From the figures presented in this section, 2.00 wt.% CB NF with and without 1.00 wt.% SDS was found to be the CB concentration holding the best performance. The boiling time was one of the shortest at 7.13 ± 0.11 min for CB NF and 7.01 ± 0.03 min for CB NFs with SDS (figure 4.5). The samples had a relatively high vapour temperature (figure 4.10), and exhibited enhanced evaporation ratios of 0.89 ± 0.01 and 0.87 ± 0.02 (figure 4.24), where the latter ratio corresponds to the sample containing SDS. The NF with 2.00 wt.% CB had one of the highest average absorption efficiencies of 0.65 ± 0.01 (without SDS) and 0.67 ± 0.03 (with SDS). This concentration also had a high average vapour generation efficiency of 0.59 ± 0.04. Due to the large uncertainty seen for the latter efficiency with 2.00 wt.%, the evaporation ratio was the measure inducing the highest reliability to verify the optimum CB NF.

4.3 Boiling iron oxide nanofluids

The results from boiling IO NFs are presented in this section. The experimental procedure and the treatment of data are identical to CB NF experiments in section 4.2, using 5 g samples for each concentration. The experimental study was also conducted at a room temperature of 23-25°C. Twelve different concentrations were investigated in the range of 0.10-20 wt.% IO. Fifty weight and temperature experimental runs were conducted. Figure 4.17 displays mass and weight data from illumination of 4.00 wt.% IO NF over a period of 30 minutes. Appendix B presents the remaining figures for IO concentrations.

The IO NF in figure 4.17 shows similar trends as the boiling of CB NFs discussed in section 4.2. All temperature and mass figures of IO NF present increased boiling time, similar peaks in vapour temperature and faster evaporation rate, when compared to water. Samples were however not as viscous as CB NFs. As mentioned previously regarding CB NFs in section 4.2, the sudden rise in vapour temperature in figure 4.17 can be explained by an increase in concentration of the NF with respect to time, which initiates excessive heating of the surrounding water of the NPs. IO NPs can also induce LSPR when heated (mentioned in section 2.1). This phenomenon could contribute to the high vapour temperature seen for all IO NFs.

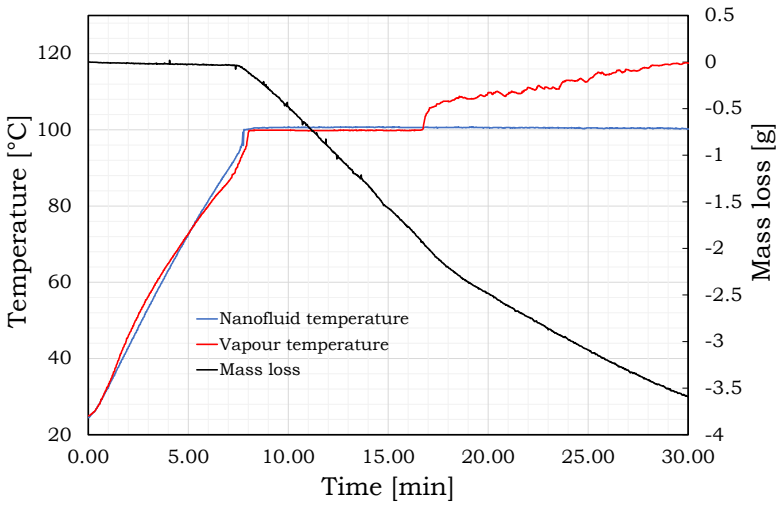

Figure 4.17: Boiling of 4.00 wt.% IO NF.

4.3.1 Temperature measurements

A relation of time until the boiling point for each corresponding concentration of IO NPs is presented in figure 4.18. The figure shows a decrease in boiling time until a low point is reached at 7.50 and 10.00 wt.% IO NF. For higher concentrations of IO NF the boiling time increases. As for CB NFs, explained in section 4.2.1, the short boiling time of IO NFs is caused by the NPs absorbing the radiation from the illumination source. With increased concentration of NPs, more particles absorb the incident light until the NPs closer to the radiation source causes a decrease in light penetration of the sample.

The NF temperature of IO concentrations with respect to time is represented in figure 4.19. As seen in the figure, 10.00 wt.% IO NF had the shortest boiling time. All samples showed boiling in comparison with the case when only water was present in a sample.

Figure 4.20 illustrates NF vapour temperature with respect to time for each NF concentration. The maximum vapour temperature for all IO concentrations plotted in figure 4.21 demonstrates the highest temperatures for concentrations between 0.10 and 10.00 wt.%. The IO NP concentrations of 2.00 wt.% and 7.50 wt.% appeared to induce the highest effect on maximum vapour temperatures. The decrease in maximum vapour temperature for concentrations of 3.00-5.00 wt.% could be a result of agglomeration. By increased NP clustering, less radiation is available for the total amount of NPs, and consequently the absorption area decreases. A significant decrease in maximum vapour temperature for concentrations above 15.00 wt.% is observed. Additional experiments were conducted to verify the reliability of the experiments, but the new tests confirmed the initial observations. Vapour temperature as a function of time is presented in figure 4.20, which demonstrates enhanced vapour temperature in all samples except 20.00 wt.% IO NF. The temperature curve of 15.00 wt.% decreases significantly after about 23 minutes of illumination. This confirms that a high NP concentration in a solution has a negative effect on the vapour temperature. A reason for this could be insufficient absorption of NPs in the sample due to NP shielding. Also, high concentrations of IO NPs could actively prompt additional agglomeration due to the large number of NPs. If the agglomerates are large enough, the convection within the NF will not induce high enough buoyancy to suspend the clustered NPs. The NPs could then potentially settle down to the bottom, or stick to the glass of the tube. For the latter case, the NPs would form a layer and reject the light from penetrating the sample.

Figure 4.19 reveals an increased temperature of approximately 104 °C for the 0.10 wt.% IO NF after the boiling point. A similar increase is seen for the water sample later in the illumination process. An explanation for this could be overheating of the thermocouple recording the temperature because of the direct radiation striking the sensor. Average NF temperature with respect to IO concentrations is shown in figure 4.22. The same decreasing trend is found in the NF temperature of CB in figure 4.11. The temperature of IO NF falls below 100°C for concentrations over 7.50 wt.%. This can, as mentioned for CB NFs in section 4.2.1, be due to boiling in the outer layers of the sample.

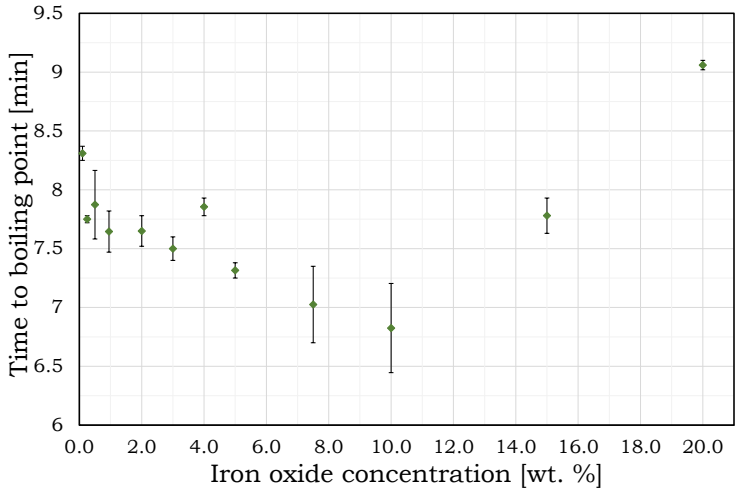

Figure 4.18: Time to reach the boiling point as a function of IO concentration.

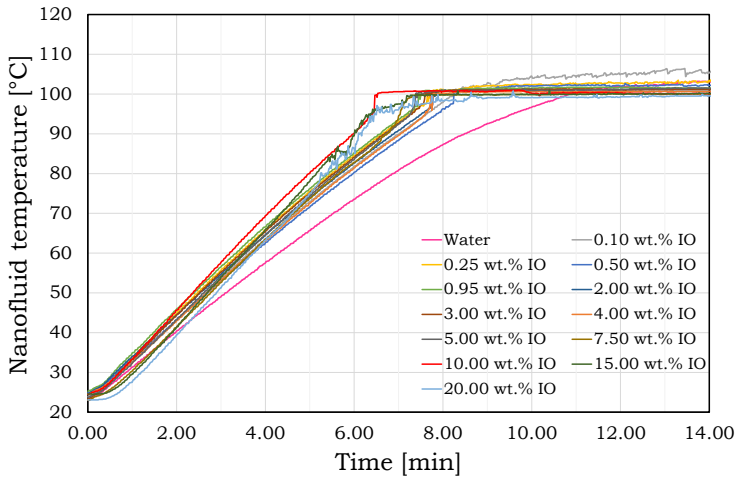

Figure 4.19: IO NF temperature as a function of time.

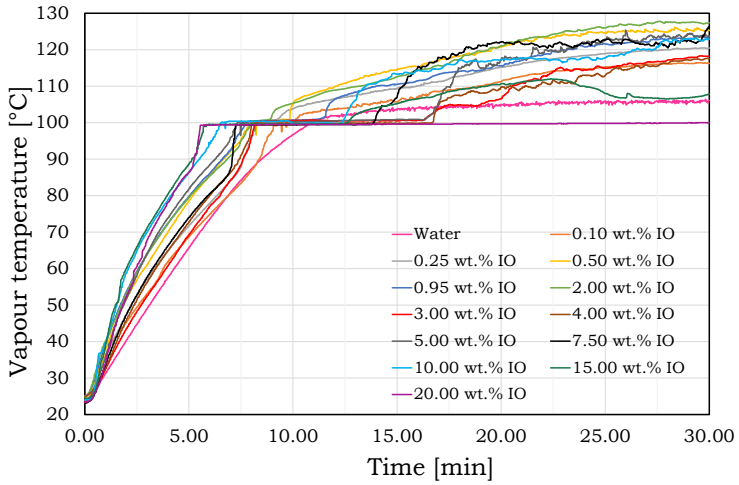

Figure 4.20: IO NF vapour temperature as a function of time.

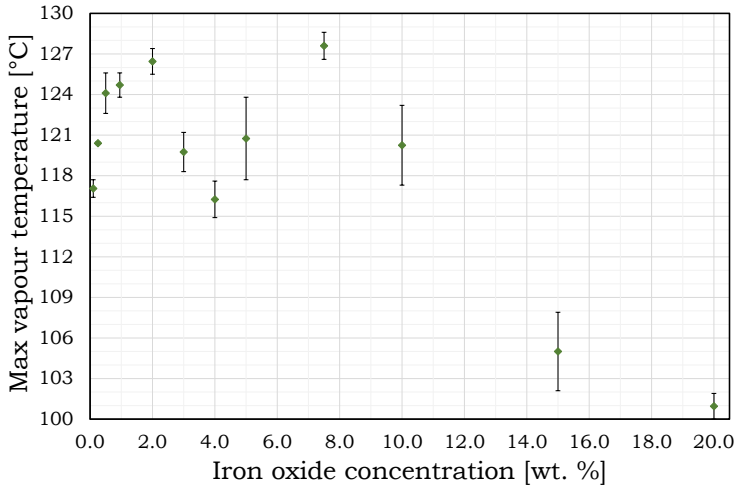

Figure 4.21: Maximum vapour temperature as a function of IO NF concentration.

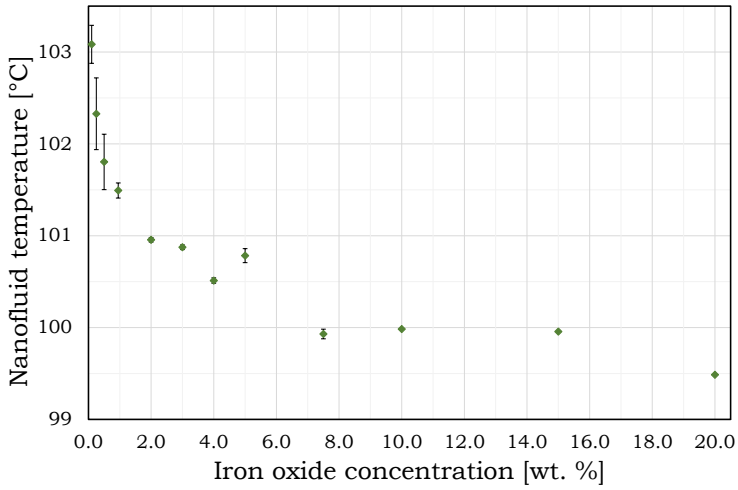

Figure 4.22: Average NF temperature as a function of IO NF concentration.

4.3.2 Weight measurements

Mass loss measurements of IO NFs were conducted in the same manner as for experiments with CB NFs, described in section 4.2.2. The NF mass before and after 30 minutes of illumination was recorded and compared with the evaporated mass logged in LabView. The manual weight recordings and mass loss data showed an excellent correspondence within a maximum error of 5.00%. As for CB NFs, mass loss experiments were considered more reliable than the temperature measurements due to the uncertainty in defining the boiling point. However, there was still a satisfying agreement between the mass and temperature experiments. When the NF temperature reached the boiling point, evaporated mass increased.

Evaporation ratio, given by mass evaporated scaled with starting mass of sample, is plotted for each IO concentrations in figure 4.23. The figure shows a steep increase in evaporation ratio from 0.50 wt.% to 0.95 wt.% IO NFs. As explained earlier, the evaporation ratio is associated with raised absorption of incident radiation due to an increased absorption area. The ratio increases until 10.00 wt.% and decreases after

15.00 wt.% due to NP shielding. Figure 4.24 represents mass loss with time for every concentration. All IO concentrations have superior evaporation ratios in comparison with water. The optimum concentration of IO NF was found to be 10.00 wt.%.

The IO mass fraction of 10.00 wt.% corresponds to a volume fraction of 2.07 vol.%. In comparison, the most efficient CB NF of 2.00 wt.% (section 4.2) equals 0.90 vol.%. The high volume fraction of IO NPs needed to accomplish max absorption compared to the results of boiling CB NFs could be due the IO NPs high bulk density compared to CB NPs. Even though IO NPs are hydrophilic, the bulk density of 5240 kg/m^3 causes settling and reduces the amount of NPs in the solution, due to the large gravity forces compared to the buoyancy induced by convection. This is especially applicable when there is a high number of agglomerates. The NP sizes of IO were found larger than of CB NPs in the SEM and TEM analysis performed, see section 3.3. This size difference could be a significant cause of more NP clustering in the IO NFs, and additionally a source of induced settling. The agglomerates of IO NPs found in air by use of TEM-images were in fact slightly smaller. Still, the behaviour of the NPs dispersed in water has not been investigated in this thesis and the sizes of agglomerates formed in the suspension are not known.

Despite the aforementioned issues, IO NFs still show enhanced evaporation ratios. With 2.00 wt.% IO NPs, the evaporation was increased by 73.0%. By adding 10.00 wt.% IO NPs the evaporation raised by 77.5%. The high photothermal response can be attributed to the different wetting of IO NPs in water, which will lead to different boiling kinetics than of hydrophobic NPs in a polar fluid. In addition, it has been reported that hydrophilic NPs enhance the convective heat transfer coefficient [83].

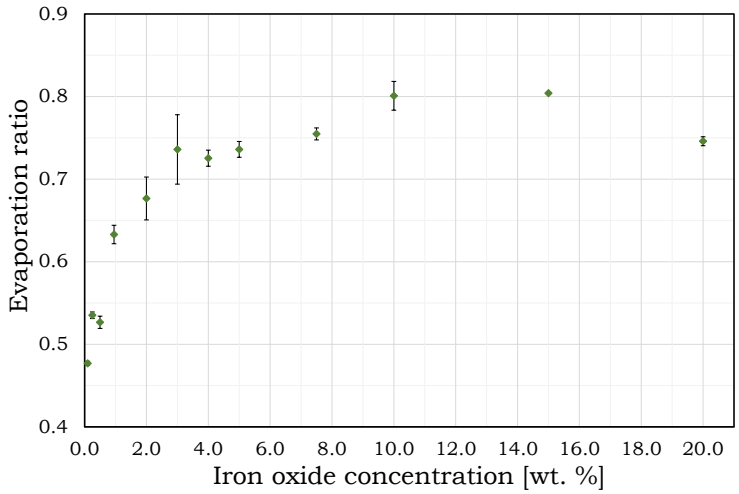

Figure 4.23: Evaporation ratio as a function of IO NF concentration.

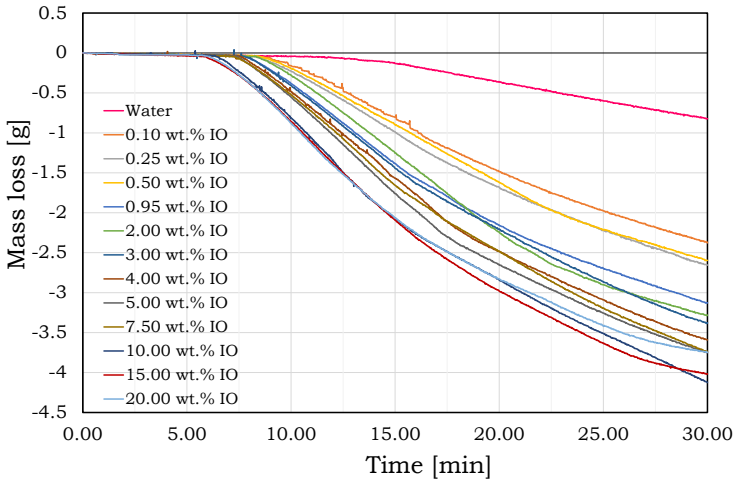

Figure 4.24: Mass loss as a function of time. Boiling of IO NFs.

4.3.3 Efficiency

Temperature and weight experiments were combined in order to obtain absorption and vapour generation efficiencies of illuminated IO NFs. The efficiencies were calculated by numerical integration using Eq. (3.1) and Eq. (3.2), in the same manner as CB NFs efficiencies (subsection 4.2.3). Figure 4.25 illustrates an example of the computed efficiency with respect to time. For comparison, absorption and vapour generation efficiencies of water are shown in the same figure. The efficiency results in terms of absorption and vapour generation for all IO NFs reveal an improved performance compared to pure tap water. Efficiency as a function of time is previously presented for a CB NF in section 4.2.3.

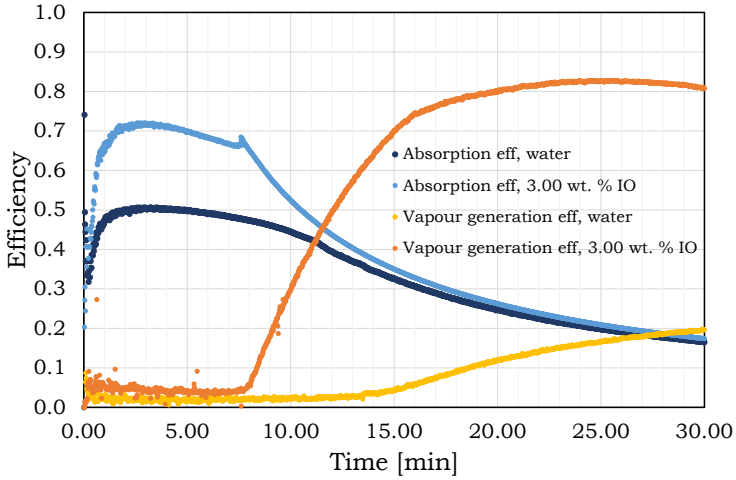

Figure 4.25: Absorption and vapour generation efficiencies of water and 3.00 wt. % IO NF.

Absorption efficiency

Figure 4.25 shows absorption efficiency as a function of time for 3.00 wt.% IO NF. The other concentrations demonstrate a similar behaviour. However, compared to a typical absorption curve of boiling CB NFs without SDS (example in figure 4.15), IO NFs do not demonstrate a defined maximum. The same is seen for water and CB with surfactant addition. This could be due to the difference in NP movement in the respective NFs with increased temperature, see figure 4.1 for convection illustrations. As mentioned previously, IO NPs are heavier than CB NPs, which leads to an increased settling. The NPs in the bottom of the tube in figure 4.1 do not homogenize until the boiling point has been reached. For CB NFs, the NPs leave the bottom of the tube prior to the boiling point due to convection. This induces a more stable absorption efficiency curve with respect to time for IO NFs, which is also applicable for water and CB NFs with SDS addition.

Time-averaged absorption efficiencies for each IO nanofluid concentration is presented in figure 4.26. The efficiency increases with increased concentration of IO NPs due to an increased absorption area, and decreases after 15.00 wt.% due to the NP shielding. Absorption is most efficient for the concentration of 10.00 wt.% IO NF. This corresponds to the results obtained from boiling time in figure 4.18 and evaporation ratio represented in figure 4.23.

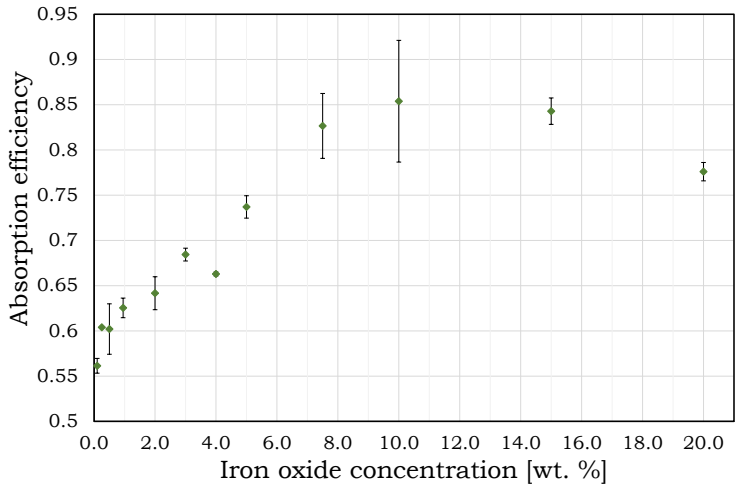

Figure 4.26: Time-averaged absorption efficiency as a function of IO NF concentration.

Vapour generation efficiency

Eq. (3.2) was used to determine vapour generation efficiencies of IO NF boiling by numerical integration. The second term in the numerator, correlating to the enthalpy increase of the vapour, induced a small contribution to the efficiency in the order of 10^{-3}. Please note that this also refers to the vapour generation efficiency of CB NFs.

Vapour generation efficiencies for the boiling of IO NFs shown in figure 4.27 were obtained by the temporal averaging values of efficiency data collected during a radiation time of 30 minutes. In figure 4.27, the vapour generation efficiency increases with concentration of IO NPs until 15.00 wt.%. An explanation of the high concentrations needed to induce maximum absorption of IO NFs can be found in subsection 4.3.2.

The optimum evaporation ratio of 10.00 wt.% in figure 4.23 should in theory correspond to the most efficient concentration presented in figure 4.27. In all vapour generation efficiency calculations, the mass fraction of water in the sample is taken into account (see explanation in section 3.6.3). In order to identify the fraction of water for each time step, the exact concentration of NPs in the solution is required. Due to the lack of true values of concentration with time, it was assumed that for all CB and IO concentrations, NPs did not leave the test tube. For CB NFs no visual NPs were seen in the condensate sample and the calculated concentration of the evaporated mass was assumed reliable. However, for IO NFs with concentration equal to and higher than 5.00 wt.%, a large number of NPs was observed in the vapour condensate. This could be the main reason of the deviation between the results for the optimum evaporation ratio and the vapour generation. The ratio of evaporation was therefore considered as more reliable than the vapour generation efficiency.

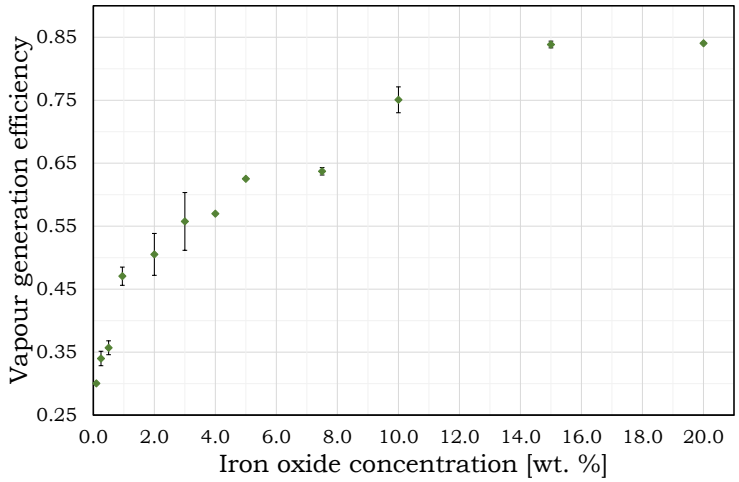

Figure 4.27: Time-averaged vapour generation efficiency as a function of IO NF concentration.

4.3.4 Summary

The concentration of IO NF with the shortest boiling time was 10.00 wt.%, which started to boil within a time frame of 6.83 ± 0.38 min. This concentration also induced the highest evaporation ratio of 0.80 ± 0.02, and the most efficient absorption of $\eta_{abs} = 0.85 \pm 0.07$. Although 15.00 wt.% IO NF was the most efficient with regard to vapour generation efficiency, the uncertainty supplied by this measure was found to be high for large concentrations. Figure 4.21 shows maximum vapour temperature with a falling trend from 7.50 wt.%. The highest vapour temperatures were found at lower concentrations in the range 120-126°C, whereas 10.00 wt.% did not yield the highest vapour temperature. By examining the obtained figures in this section, the performance at lower concentrations is satisfying. Due to the large amount of NPs used to make 10.00 wt.%, it was decided that 2.00 wt.% IO NFs was sufficient to obtain a decent performance with regard to evaporation ratio and absorption efficiency, in addition to producing high temperature steam at 126.45 ± 0.95°C. Efficiencies of 2.00 wt.% IO correspond to $\eta_{abs} = 0.64 \pm 0.02$ and $\eta_{boil} = 0.51 \pm 0.03$. with the evaporation ratio of 0.68 ± 0.03.

4.4 Comparing the nanofluids

The most efficient NF samples of CB and IO NFs found in section 4.2 and section 4.3, demonstrated enhanced performance with regard to evaporation ratio, maximum vapour temperature, and efficiencies. These NFs were studied in series of additional experiments in order to double-check their performance. Distilled water was used as base for the NFs.

Figures showing temperature and mass loss can be found in Appendix C. The vapour and NF temperature of samples containing SDS revealed intervals with unrealistic temperatures, as observed in earlier experiments described in section 4.2.1.

Mass loss with respect to time is presented in figure 4.28. It shows $82.82 \pm 0.40\%$ and $82.61 \pm 0.46\%$ enhanced evaporation for CB and IO NFs, respectively. CB NFs containing SDS shows $83.82 \pm 0.41\%$. As mentioned in section 4.2.2, the evaporation ratio for samples with SDS was calculated by the mass difference, which could include an additional uncertainty. Figure 4.29 presents efficiencies for NFs and water. Absorption efficiencies for all NFs demonstrate improved performance compared to water. A similar defined absorption peak for CB NFs as in previous experiments is revealed in figure 4.29. The high efficiency data is most likely due to the assumed absorption area discussed earlier. The area in which a fluid absorbs illuminated radiation is dependent on the volume penetrated by the light. Due to NP addition, the volume is not solely determined by the concentration, but the orientation and sizes of NPs and agglomerates in the fluid. This area is difficult to determine for each concentration of NFs.

Table 4.1 presents an overview of the key performance factors of the NFs, which potentially can be used in a DASC. An increase in vapour temperature was observed in these results. The sensor was positioned 0.7 cm closer to the NF than in the experiments presented in previous section, which can explain the increased temperature of water and NF vapour shown in table 4.1 compared to previous experiments. The increase can be explained by the temperature gradient formed over the sample as a consequence of temperature rise in the NF, in addition to less nucleation centers in distilled water.

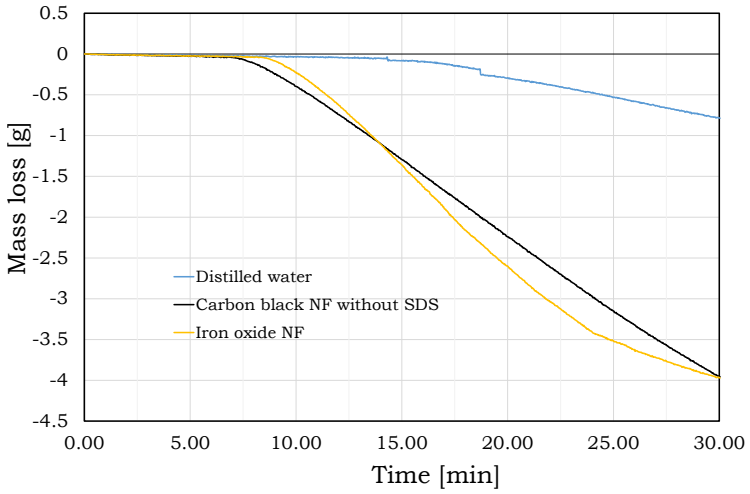

Figure 4.28: Mass loss as a function of time of water, 2.00 wt.% IO NF and 2.00 wt.% CB NF with and without SDS.

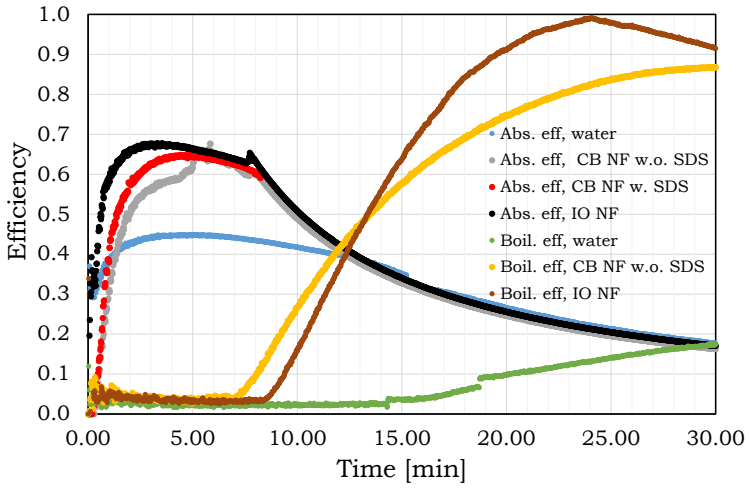

Figure 4.29: Absorption and boiling efficiency for water, CB NF with and without SDS and IO NF.

Table 4.1: A summary of experimental results by illumination of distilled water, 2.00 wt.% CB NF w. and w.o. SDS, and IO NF.

Fluid	**Evap. ratio**	**Max vap. T [°C]**	η_{abs}	η_{evap}
Dist. water	0.13 ± 0.24	120.1 ± 0.00	0.40 ± 0.00	0.06 ± 0.01
CB NF	0.77 ± 0.02	125.6 ± 0.60	0.58 ± 0.02	0.46 ± 0.02
CB NF+SDS	0.82 ± 0.02	129.4 ± 0.85	0.60 ± 0.01	-
IO NF	0.76 ± 0.03	128.7 ± 0.85	0.67 ± 0.02	0.53 ± 0.01

The time-averaged absorption efficiencies in table 4.1 reveal an improved absorption compared to water. By use of 2.00 wt.% CB NF, absorption is enhanced by $31.90 \pm 0.92\%$. The addition of SDS advances the fluids ability to capture radiation by $34.33 \pm 0.72\%$. This demonstrates that surfactant addition increases the area of absorption by suspending the NPs in water. However, IO NFs with 2.00 wt.% presents the most efficient absorber by $40.51 \pm 0.83\%$ enhancement of water absorption capability. This NF also reveals the highest raise of the time-averaged vapour generation efficiency by $88.28 \pm 0.08\%$ in comparison to water. CB NFs without surfactant also improves the vapour generation process by $86.48 \pm 0.35\%$. The vapour generation efficiency of CB NF with SDS is not included in table 4.1 due to the uncertainty followed by the mass difference.

The addition of IO and CB NPs in a DASC will contribute to a more efficient evaporation due to the high photothermal response of the particles when dispersed in water. In these results, the NF containing 2.00 wt.% IO presents a greater evaporation efficiency than CB NFs. Also, CB NPs dispersed in water with the aid of SDS induces a higher evaporation ratio than both CB NPs without surfactant and IO NFs. This could be due to a variation in the interfacial contact between NPs and water in the different NFs. To optimize the heat transfer between a solid and a liquid, a high heat transfer coefficient is needed (mentioned in subsection 4.3.2) and a low thermal resistance is required between the two phases [57].

4.5 Characterization of the condensed vapour

4.5.1 Overview

The effect of nano-sized particle exposure of humans is still not entirely known [85]. There is a risk that NPs could be toxic, both for humans and the nature. Measures must therefore be put into action in order to avoid emissions to the environment. In addition, it is important to know if the NPs follow the vapour flow. Presence of NPs could potentially be deposited in the recycling system if the condensate were to be re-used. Also, if the steam is clear of NPs, it is easier to control the concentration in the volumetric absorber. Furthermore, it is important to verify contamination if the generated steam was used for medical cleaning applications or for drinking water purposes.

In this analysis the main goal was to detect any existence of possible NP contamination in the condensates rather than to perform a quantitative analysis of their presence. Condensate samples from the boiling of each concentration of IO and CB NFs with and without SDS were examined. Since tap water was the base fluid used to produce the NFs, a sample taken directly from the sink was used as a reference in this analysis. A qualitative and quantitative analysis of the local tap water provided by [86] can be found in Appendix F. Furthermore, an open container holding a sample of the tap water was placed in the NF production laboratory for three days. The latter sample was then analysed in order to investigate any NP contamination in the lab.

4.5.2 Raman spectroscopy

To identify any contamination of the condensed vapour from CB and IO NFs, Raman spectroscopy was performed. The Raman spectroscopy instrument illuminates a material using monochromatic light in order to verify its chemical composition and concentration. All chemicals hold unique fingerprints based on the frequency of the scattered radiation due to their vibrational and rotational characteristics, which is dependent on the molecular shape and structure, molecule-molecule interactions and chemical bonding [87, 88]. The dominant part of the scattered radiation has a frequency equal to the frequency of the incident radiation, which is known as Rayleigh scattering. Only a small fraction constitutes different frequencies. The latter is known as Raman scattering, where the intensity and the Raman shift is obtained in a Raman spectrum. The Raman shift gives information of the frequency transitions within molecules, whereas the intensity of a Raman spectrum is directly proportional to the concentration. The shift is recognized by peaks in a Raman spectrum, where the location of the peaks is important for a quantitative analysis.

The instrument used for condensate characterization was of the type RamanRxn1 Analyzer with a spectral coverage from 100-3425 cm^{-1}. This instrument can be used for analysis of liquid samples, films, powders, solids, and biological materials.

The Raman spectrum obtained in Figure 4.30 displays no direct sign of any CB NPs contamination by examination of the peaks, comparing it to the spectrum of water. The overall increase in Raman intensity, especially for the condensate of boiling 10.00

wt.% CB NFs is a result of background interference called fluorescence. This is a typical challenge within Raman spectroscopy, and is usually due to sample properties and the Raman technique being used [89]. CB can be identified by the band peak at 1340 cm^{-1} called the D-band and by 1580 cm^{-1} referred to as the G-band [90].

The samples containing SDS were all visually contaminated, which can also be seen in the Raman spectrum in figure 4.31. Both the D-band and the G-band show large peaks. This can be explained by the decrease in surface tension of the NF by surfactant additions. As mentioned in subsection 4.2.1, CB NFs containing SDS generated foam after the boiling point was reached. This foam carried NPs further in the system. The SDS presence can be determined by C-C stretching modes in the region 1050-1150 cm^{-1}, CH_2 twisting mode at 1300 cm^{-1} and bending modes at 1050-1150 cm^{-1} [91]. Neither the C-C stretching mode, nor the CH_2 bending mode was observed in the spectrum. The same peak identifying CB in the Raman shift around 1300 cm^{-1} could also indicate that SDS was present in the condensate due to the CH_2 twisting mode. However, since neither of the two peaks relating to the surfactant were observed, it can be suggested that SDS most likely stays in the NF. Considering SDS is a salt, which under ordinary circumstances does not evaporate, the latter could be a probable scenario.

Figure 4.32 represents the Raman spectrum from the condensate of IO NFs where concentrations from 0.10-10.00 wt.% were investigated. Condensate samples of the boiling of 5.00 and 10.00 wt.% IO revealed a change in Raman intensity for the shift at 686 cm^{-1}, which corresponds to Fe(III)-O motions [90]. Other modes were not detected. The credibility of the current Raman analysis was put into question due to visual detection of IO NPs in condensate samples at lower concentrations. Their presence was not detected using Raman spectroscopy.

Some materials scatter a small fraction of Raman scattering. Due to this issue, the concentration of these materials must be high enough in order to detect changes in frequency [88]. The sensitivity of the instrument can, in some cases, be adjusted to obtain a representative Raman spectrum. However, sensitivity adjustments did not detect any change in the spectrum for dilute samples.

A chemometric analysis named principal component analysis (PCA) was performed at the UiB Chemistry Department, in order to obtain additional information from the individual Raman spectrum of the IO NF condensates. A PCA calculates new, independent, latent variables that are linear combinations of the measured variables [92]. The linear combinations are constructed in order to capture as much variance as possible while being mutually orthogonal. In other words, the variance of the measured variables are explained in one latent variable or component, which is expressed as a vector. The components contributing the most in explaining the variance define the coordinates in a PCA score plot. The score of the vector consists of a value which is plotted in the same plot [93].

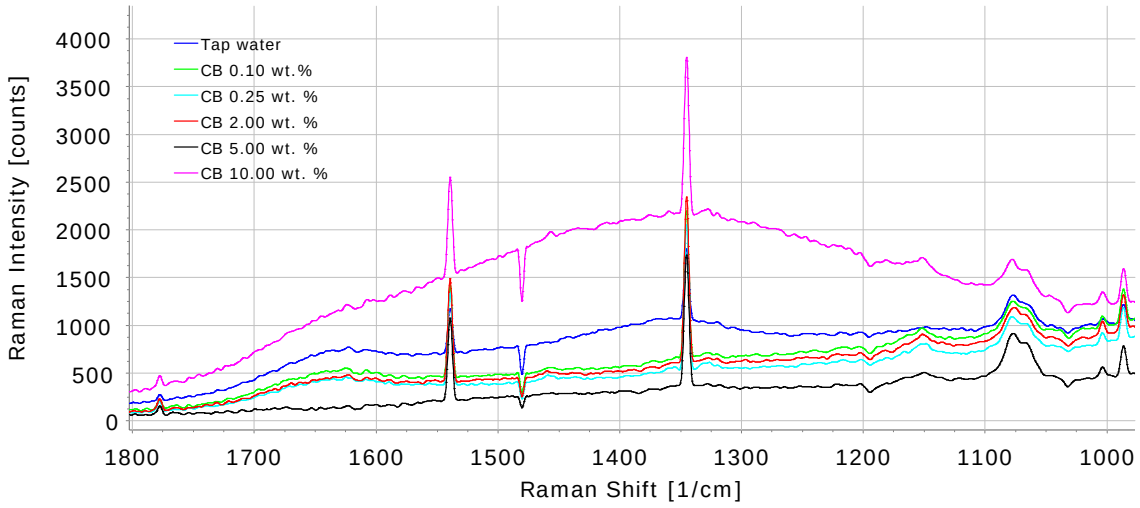

Figure 4.30: Raman spectrum of condensates obtained from CB NFs without SDS.

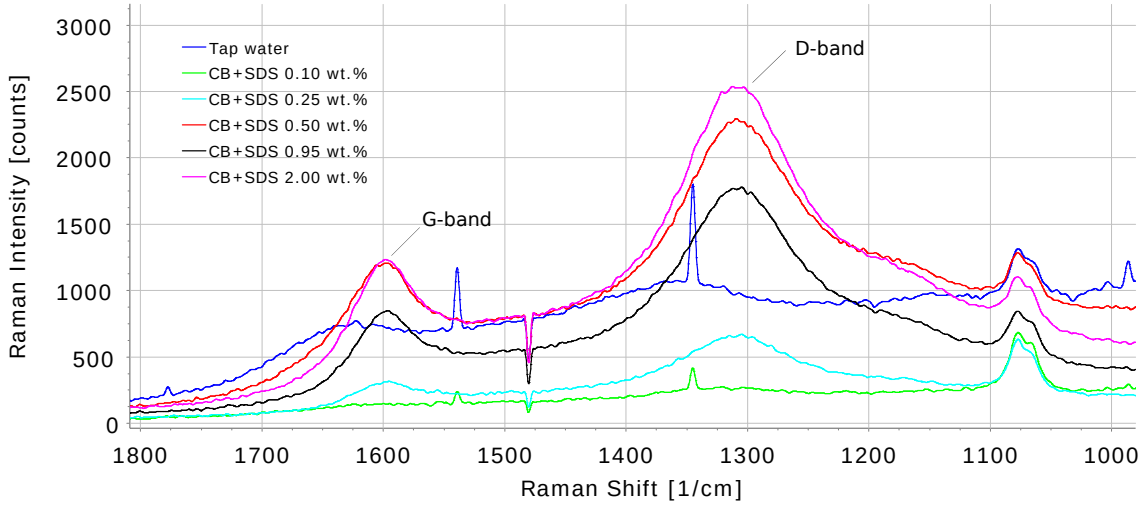

Figure 4.31: Raman spectrum of condensates obtained from CB NFs with SDS.

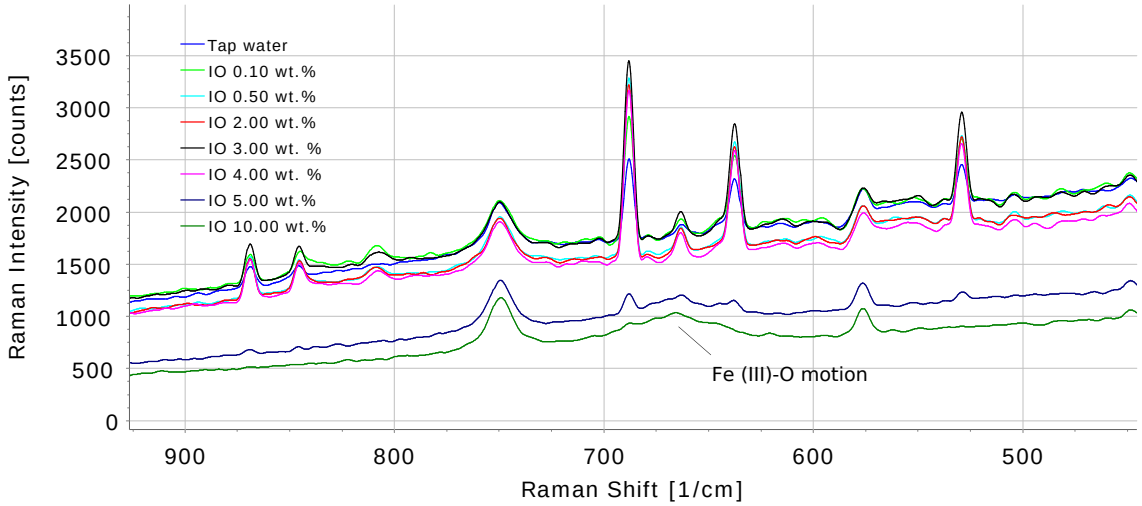

Figure 4.32: Raman spectrum of condensates obtained from IO NFs.

Figure 4.33 presents a PCA score plot by use of IO condensate samples, direct tap water and tap water exposed to the air in the laboratory for a period of three days. The data was extracted from the Raman shift region 300-1800 cm^{-1}. The x-axis represents component 1, which explains 84.8% of the variance in the spectrum, whereas component 2 only explains 8.7%. The variation with regard to component 1 is therefore the the most important component explaining the variance within the data set.

If the components represent all or a large contribution of the variation, the scores in a PCA score plot which falls close to each other have similar properties with the original data [93]. In figure 4.33, the two components contain 93.5% of the variation. From the score plot, the condensate from concentrations of 5.00 wt.% and 10.00 wt.% are close together. As mentioned previously, these concentrations showed peaks in the Raman spectrum in figure 4.32, confirming IO contamination. In the score plot, all other samples of IO NF condensates are clustered together, which reveals that these have a similar spectrum. However, pure tap water has a different score in component 1. This indicates that all condensate samples of IO NFs could be contaminated. In addition, the tap water sample is found in the dilute samples of IO NF condensates, which could refer to a possible contamination of the lab where all the experiments were conducted.

Due to the lack of obtained data for diluted samples containing NPs by use of Raman spectroscopy analysis, a further investigation of the samples was needed. The new analysis had to confirm whether the condensates from boiling CB NF without SDS, dilute IO condensates and the sample exposed to the laboratory were contaminated.

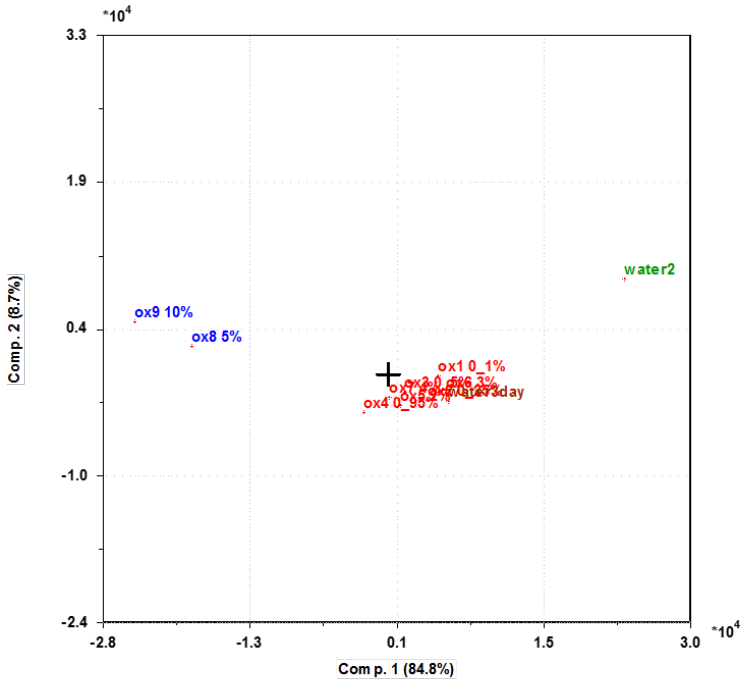

Figure 4.33: PCA score plot of condensate samples of IO NFs, direct tap water and tap water exposed for three days.

4.5.3 Static light scattering

Condensate samples from the boiling of each respective concentration of CB and IO NFs, were further analysed by use of FRITSCH ANALYSETTE 22, which is a static light scattering (SLS) instrument[1]. The instrument can detect particle sizes within the range of 0.01-2100 μm. In the figures shown below, two parameters vary with particle size; cumulative particle size distribution and normalized particle size distribution. The cumulative distribution presents the number of particles at or below a particle size, while the normalized distribution shows the amount of particles at each size [94]. One condensate sample constituting from a single NF concentration of each volumetric absorber was found sufficient in order to present the qualitative analysis of the samples.

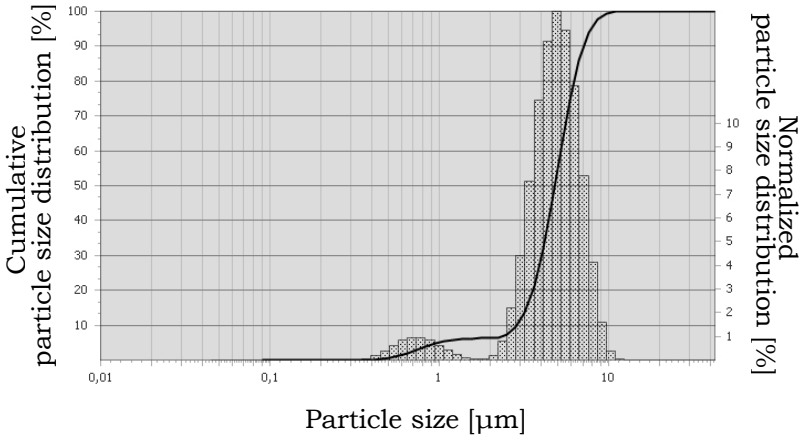

Figure 4.34: Particle size distribution of tap water.

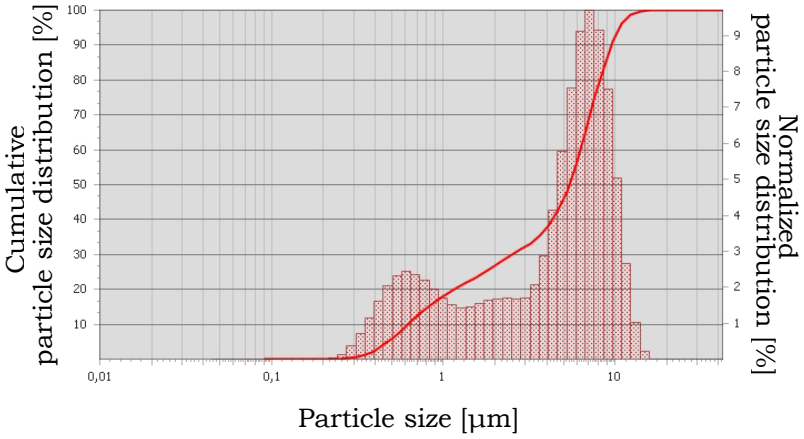

Figure 4.35: Particle size distribution of tap water exposed to the lab air for three days.

The size distribution of particles present in tap water was shown to be between 0.40-1.10 μm and 1.10-10.03 μm, with an average of 4.80 μm, see figure 4.34. Figure 4.35 displays the size distribution of water exposed to the lab air for three days. By comparing the two water samples, an increase in the number of particles between 0.30-1.50 μm was revealed in the exposed sample. In addition, smaller particle sizes

[1]Collaboration with Moscow Engineering Physics Institute.

were detected in the area of 0.10-0.30 μm. Dust in the lab air could potentially effect the sample being exposed. The sizes of dust particles are dependent upon the type, which can originate from the out- and indoor environment. Particle size of dust is defined being less than 50 μm, and can for example contain soil, sand, micro-organisms, human skin, clothing, pollen, and so forth [95]. When considering the latter statement, a detection of particle sizes over a large size range might indicate dust. Nevertheless, the SLS analysis of the three-day water sample does not reveal particles larger than 10.06 μm. The microscope analysis in section 3.3 presents CB NP agglomerates in air of sizes between 2.5-31.0 μm, and IO NP agglomerates to be in the range of 2.0-31.0 μm. It is therefore more likely that the exposed sample is polluted by NPs and not dust.

NP air pollution in the laboratory can effect the SLS results of the condensate samples. This is due to the sample handling of the condensates after each NF boiling experiment, which took place in the laboratory. However, the probability of the latter decreases due to the extension of condensate exposure being less than half a minute. Direct tap water in figure 4.34 was therefore used as reference in the SLS analysis of condensate samples.

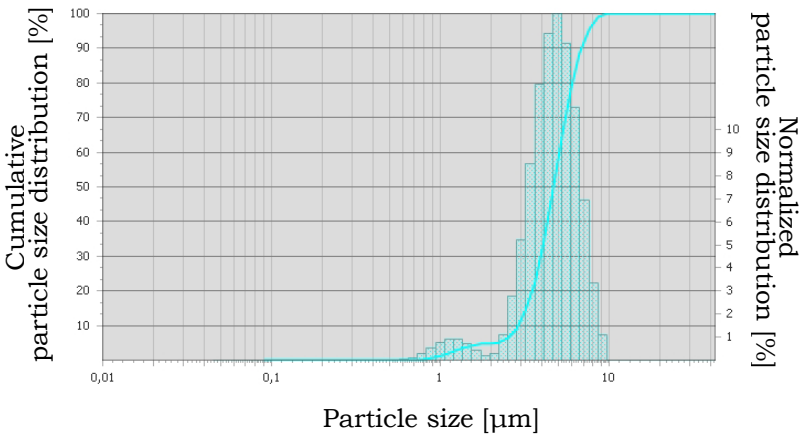

Figure 4.36: Particle size distribution in condensate obtained from 4.00 wt.% CB NF.

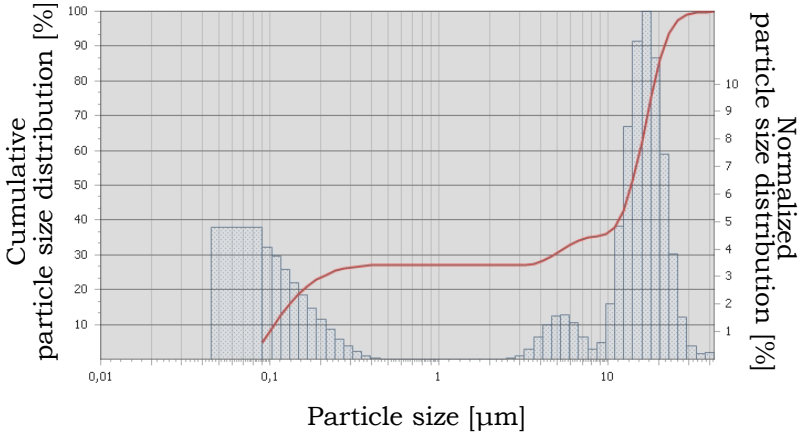

Figure 4.37: Particle size distribution in condensate obtained from 0.95 wt.% CB NF with SDS.

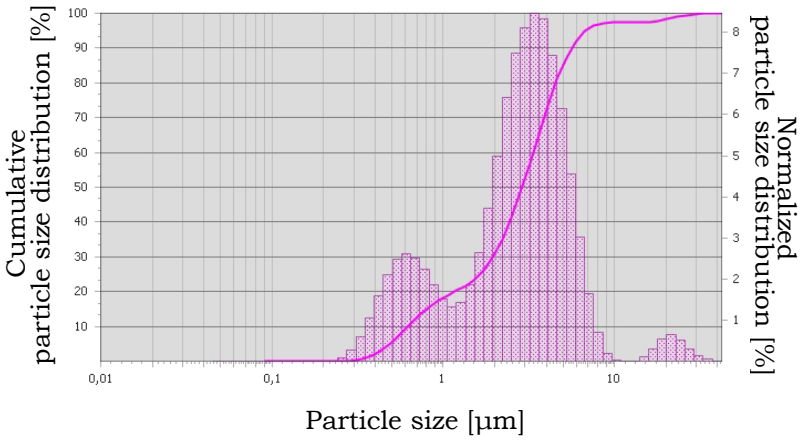

Figure 4.38: Particle size distribution in condenate obtained from 3.00 wt.% IO NF.

The CB NF condensates revealed a similar size distribution as tap water and did not indicate NP presence. Figure 4.36 presents the SLS result from the condensate obtained from 4.00 wt.% CB NF. The small variations seen in the figure can be attributed to the change in the tap water quality of the day the sample was taken. The complete NP deposition in the CB NF samples can be due to the hydrophobic properties of CB NPs, in addition to a higher gravitational force compared to the buoyancy induced by the boiling of water.

With the use of SLS, contamination was seen in all the condensate samples of CB NFs containing SDS. In figure 4.37, the particle size distribution of the condensate constituting from 0.95 wt.% CB NF with SDS addition is illustrated. It reveals a distribution of particles ranging from the sizes 0.046 to 10.06 μm. A large amount was detected from 0.046 to 0.460 μm, which indicates CB agglomerates. CB NPs was also identified in the Raman spectrum in previous subsection, but the spectroscopy analysis of CB NF condensates consituting from NFs with concentrations < 0.25 wt.% failed to detect the NPs. As mentioned in subsection 4.5.2, an explanation of the presence of CB NPs in the condensate samples could be a result of the reduced surface tension of water due to the SDS addition.

The Raman spectrum in figure 4.32 indicates condensate contamination for NF concentrations $\geqslant$ 5.00 wt.% IO. When using SLS, a change in the particle size distribution was seen for condensate samples above 3.00 wt.%. There was no clear indication of NP presence in dilute concentrations. Figure 4.38 presents the particle size distribution in 3.00 wt.% IO NF condensate, revealing particle sizes in the range of 0.24-10.06 μm. Particles between 10.05 and 10.28 μm were observed in 3.00 wt.%, which could be a sign of large agglomerates. This could also imply a change in the tap water quality of the day this sample was taken. The sizes are approximately in the same range as tap water, however the amount of particles has increased significantly.

The cause of IO NPs being led by steam for large concentrations of IO NFs can be due to the hydrophilic properties of IO. Recent studies [96–99] have reported reduced radius of vapour bubbles in hydrophilic NFs, compared to the vapour bubbles formed in pure water. This is explained by the decreased surface tension induced by hydrophilic NPs. Quan et al. [83] suggest that for NPs inducing high wettability

properties, the small bubble size can reduce the amount of NPs incorporated at the bubble surface. A smaller amount of NPs per vapour bubble can lead to an increased buoyancy compared to the gravitational force, and be a reason for NP presence in the vapour. With a large amount of IO NPs, here found to be $\geqslant 3.00$ wt.%, the wettability may be suitable for NP departure.

The results from the SLS analysis are shown in an article submitted to *Applied Thermal Engineering* attached in Appendix G.

4.6 Uncertainty analysis

To increase the the credibility of the results, experiments were reproduced in order to reduce the uncertainty. Sample collection, mass and temperature measurements, and efficiency data include uncertainties with regard to procedure, set-up, and instrumentation. Instruments used to obtain the results all hold a given uncertainty, which are listed in table 4.2.

The measurement of the respective concentrations of NFs consist of independent measurements of water, NPs, and SDS when applicable. As a result, the concentration uncertainty of the NFs, calculated using Eq. (A.3) in Appendix A, was ± 0.0001 wt.%. In addition, an increased uncertainty arises when measuring the amount of CB NF for high NP concentrations (> 2.00 wt.%). This is due to an increased viscosity of the samples, resulting in a more difficult sample collection.

All experiments were conducted with a starting temperature corresponding to the ambient temperature in the laboratory. Changes in the room temperature may have occurred and the starting temperature for each experiment could vary. It was therefore important to verify the significance of the variation and whether it could influence the credibility of the experimental data. The average start temperature of the experiments involving CB NFs, CB NFs with surfactant and IO NFs were 24.93 ± 0.68°C, 24.60 ± 0.83°C and 24.24 ± 0.59°C, respectively. The largest variation of the start temperature existed for experiments of CB NF with SDS addition. An experimental error was calculated using all start temperatures recorded for CB NFs with SDS. The most extensive temperature change from room temperature to approximately 100°C was considered. The uncertainty contributing to temperature measurements was found to be ± 0.0344°C.

The response time of the temperature sensors was verified prior to the experimental work, see section 3.4.1 and Appendix E.0.2 for further information. However, NPs sticking to the thermocouple may have interfered with the temperature measurements. This uncertainty occurred in all experiments where different concentrations were used. To reduce this uncertainty to a minimum, the thermocouples were cleaned carefully with water and concentrated ethanol between experiments.

It should be noted that the merge of mass and temperature data leads to an unavoidable experimental error for the set-up used in the thesis. By comparing the obtained results in a mass-temperature diagram, the observations were physically reasonable. Nevertheless, an uncertainty regarding the stability of the NF samples, and an exact distance from the tube to the lamps exists. The relative uncertainty

of the measured distance of 10 cm is 1.0%. If the tube were situated 0.1 cm closer to the lamp, the radiative heat flux, according to figure 3.8, would increase by 31.9 W/m^2. This would only effect the absorption efficiency by approximately 0.55%. Therefore, the presence of the thermocouple in the temperature measurements of the NFs may have had the largest influence on temperature and weight experiments. This is discussed thoroughly in section 3.5. In addition, as mentioned previously, the effect on NP clustering to the thermocouples may also induce an uncertainty.

The efficiency data can be considered as a vulnerable parameter due to the number of independent variables, which all hold different uncertainties. The total uncertainty of absorption efficiency was calculated using Eq. (A.3) in Appendix A and found to be ± 0.0031. The variable that has the most significant influence is the absorption area A, which is also discussed in section 3.6.

Table 4.2: Instrumental uncertainties

Instrument	**Manufacturer**	**Parameter**	**Uncertainty**	**Unit**
Radiometer, LSS 122 IR	Lingshang	Heat flux	± 1	W/m^2
Thermometer, ST-9215B	Yi Chun Electrics	Temperature	± 0.1	°C
T type, HTMQSSIM100G150	Omega	Temperature	± 0.1	°C
Weight scale, CPA 324S	Sartorius	Mass	± 0.0001	g
Data acquisition	LabView	Time	± 1	s
Dry well, 9102S	FLUKE	T reference	± 0.25	°C
Radiometer, AAC-VIS	TriOs	Radiation	6-8%	$Wm^{-2}nm^{-1}$

5. Conclusion

In this thesis, three NFs with a broad range of concentrations were compared by analysing boiling time, evaporation ratio, vapour temperature, absorption and vapour generation efficiency. The objective was to investigate their volumetric absorption and steam generation capabilities for future solar energy utilization. The investigated NFs contained NPs of hydrophobic CB and hydrophilic IO, where a surfactant (SDS) was added to a series of CB NF samples in order to increase dispersion stability. Each NF sample was illuminated over a period of 30 minutes, using two halogen lamps delivering 5759.7 W/m^2 each.

All the NFs showed improved efficiencies compared to water, which can be applied to the high photothermal response of the NPs due an increase in absorption area. Of all the NF concentrations examined, the NFs containing 2.00 wt.% CB, 2.00 wt.% CB with SDS and 2.00 wt.% IO were found to exhibit an optimum absorption distribution of NPs in order to achieve high evaporation efficiencies and vapour temperatures. The absorption efficiencies of CB NF, CB NF with SDS and IO NF were improved by $31.90 \pm 0.92\%$, $34.33 \pm 0.72\%$ and $40.51 \pm 0.83\%$ compared to water. The increased absorption of CB containing SDS compared to the case without SDS, can be attributed to a better NP dispersion, leading to an increased area of absorption, in addition to a possible enhanced thermal contact between the NPs and the water molecules. The most efficient absorber was the IO NF sample with a vapour generation efficiency of 0.53 ± 0.01. Further, the experiments revealed a vapour generation efficiency of 0.46 ± 0.02 for CB NF and 0.06 ± 0.01 for water.

With steam temperatures from 125-129°C and evaporation ratios of 0.77 ± 0.02, 0.82 ± 0.02 and 0.76 ± 0.03 compared to water with a ratio of 0.13 ± 0.24, all the NFs are volumetric absorber candidates in a DASC.

The NF used for future collectors must be cheap enough to compete against other energy resources, but also hold no risks of human exposure of NPs in addition to zero emissions of NPs to the nature. In order to achieve this, a possible contamination of the vapour generated by boiling NFs must be revealed. In this thesis, condensate samples were examined by use of Raman spectroscopy. The condensates of all CB NFs samples containing SDS showed contamination, which can be explained by the reduced surface tension of water. In addition, the condensates for IO concentrations over 5.00 wt.% indicated contamination. However, this method of analysis was not sufficient to obtain results of samples containing low concentrations of NPs. A SLS analysis was therefore conducted with the aim to reveal existing NPs in dilute samples. No CB NFs condensates revealed contamination by use of SLS, however IO NPs were found in the vapour condensates belonging to $\geqslant 3.00$ wt.% IO NFs. This

can be attributed to the wettability of IO NPs which by increased concentration reduces the bubble size in water [83].

Of the volumetric absorbers investigated in this thesis, 2.00 wt.% IO is most fitted for electricity generation since this NF achieved the highest efficiencies and steam temperatures. For applications where the water condense needs to be free of NPs, 2.00 wt.% CB without SDS addition can be suggested.

6. Future work

Suggestions for future work is listed below:

- Scale up and improve the current experimental set-up by adding a steam turbine. Recycle vapour using optimum concentrations of CB and IO NFs, or other types of NF.
- Further investigation of the stability of CB and IO NFs.
- Boil IO NFs containing a surfactant and review whether this influences dispersion and efficiency.
- Study optical properties, such as extinction coefficient, of NFs at temperatures which solar collectors operate (50-100 °C).
- Compare radiative losses in surface absorbers and different volumetric absorbers using numerical simulations. Investigate how geometry and radiation angle effects the thermal losses.
- Develop a better model for the absorption area in order to increase the accuracy in efficiency results for DASCs.
- Establish an accurate method to quantitatively characterize contamination of fluids containing low concentrations of NPs.

Bibliography

[1] "International Energy Outlook 2017." [Online]. Available: https://www.eia.gov/outlooks/ieo/pdf/0484(2017).pdf

[2] "BP Statistical Review of World Energy 2017." [Online]. Available: https://www.bp.com/content/dam/bp/en/corporate/pdf/energy-economics/statistical-review-2017/bp-statistical-review-of-world-energy-2017-full-report.pdf.

[3] "United Nations Sustainable Development Goals," (Accessed: 30.11.2017). [Online]. Available: http://www.un.org/sustainabledevelopment/energy/

[4] R. Ehrlich, *Renewable Energy: A First Course*, 1st ed. CRC Press, 2013.

[5] "Solar, 2013." [Online]. Available: https://www.worldenergy.org/wp-content/uploads/2013/10/WER_2013_8_Solar_revised.pdf

[6] R. Taylor, "Thermal Energy Conversion in Nanofluids," 2011, PhD thesis, Arizona State University.

[7] R. Chen, Z. Wu, T. Zhang, T. Yu, and M. Ye, "Magnetically recyclable self-assembled thin films for highly efficient water evaporation by interfacial solar heating," *RSC Adv.*, vol. 7, no. 32, pp. 19 849–19 855, 2017.

[8] Y. Tian and C. Y. Zhao, "A review of solar collectors and thermal energy storage in solar thermal applications," *Applied Energy*, vol. 104, pp. 538–553, 2013.

[9] G. Boyle, *Renewable Energy: Power for a Sustainable Future, Chapter 2*, 3rd ed. Oxford University Press and The Open University, 2012.

[10] M. I. R. Serrano, *Concentrating Solar Thermal Technologies: Analysis and Optimisation by CFD Modelling.* Springer, 2016.

[11] S. Manikandan and K. S. Rajan, "Sand-propylene glycol-water nanofluids for improved solar energy collection," *Energy*, vol. 113, pp. 917–929, 2016.

[12] A. Guo, Y. Fu, G. Wang, and X. Wang, "Diameter effect of gold nanoparticles on photothermal conversion for solar steam generation," *RSC Adv.*, vol. 7, no. 8, pp. 4815–4824, 2017.

[13] J. Liu, C. Xu, L. Chen, X. Fang, and Z. Zhang, "Preparation and photothermal conversion performance of modified graphene/ionic liquid nanofluids with excellent dispersion stability," *Solar Energy Materials and Solar Cells*, vol. 170, pp. 219–232, 2017.

[14] H. Ghasemi, G. Ni, A. M. Marconnet, J. Loomis, S. Yerci, N. Miljkovic, and G. Chen, "Solar steam generation by heat localization," vol. 5, p. 4449, 2014.

[15] G. Ni, G. Li, S. V. Boriskina, H. Li, W. Yang, T. Zhang, and G. Chen, "Steam generation under one sun enabled by a floating structure with thermal concentration," *Nat. Energy*, vol. 1, p. 16126, 2016.

[16] O. Neumann, A. D. Neumann, E. Silva, C. Ayala-Orozco, S. Tian, P. Nordlander, and N. J. Halas, "Nanoparticle-Mediated, Light-Induced Phase Separations," *Nano Lett.*, vol. 15, pp. 7880–7885, 2015.

[17] H. Jin, G. Lin, L. Bai, A. Zeiny, and D. Wen, "Steam generation in a nanoparticle-based solar receiver," *Nano Energy*, vol. 28, pp. 397–406, 2016.

[18] L. Zhang, J. Liu, G. He, Z. Ye, X. Fang, and Z. Zhang, "Radiative properties of ionic liquid-based nanofluids for medium-to-high-temperature direct absorption solar collectors," *Solar Energy Materials and Solar Cells*, vol. 130, pp. 521–528, 2014.

[19] R. A. Taylor, P. E. Phelan, T. P. Otanicar, R. Adrian, and R. Prasher, "Nanofluid optical property characterization: Towards efficient direct absorption solar collectors." *Nanoscale Res. Lett.*, vol. 6, 2011.

[20] X. Wang, Y. He, G. Cheng, L. Shi, X. Liu, and J. Zhu, "Direct vapor generation through localized solar heating via carbon-nanotube nanofluid," *Energy Conversion and Management*, vol. 130, pp. 176–183, 2016.

[21] A. Polman, "Solar Steam Nanobubbles," *ACS Nano*, vol. 7, pp. 15–18, 2013.

[22] J. Philip and P. D. Shima, "Thermal properties of nanofluids," *Adv. Colloid Interface Sci.*, vol. 183–184, pp. 30–45, 2012.

[23] O. Neumann, N. J. Halas, A. Urban, N. Hogan, Z. Fang, S. Lal, A. Pimpinelli, and P. Nordlander, "Solar vapor generation enabled by nanoparticles," *Abstr. Pap. Am. Chem. Soc.*, vol. 246, 2013.

[24] J. P. Liu, "Ferromagnetic nanoparticles: Synthesis, processing, and characterization," *JOM*, vol. 62, no. 4, pp. 56–61, 2010.

[25] E. Petryayeva and U. J. Krull, "Localized surface plasmon resonance: Nanostructures, bioassays and biosensing - A review," *Analytica Chimica Acta*, vol. 706, no. 1, pp. 8–24, 2011.

[26] C. D. Geddes, *Reviews in Plasmonics 2016*. Springer, 2017.

[27] S. A. Angayarkanni and J. Philip, "Review on thermal properties of nanofluids: Recent developments," *Advances in Colloid and Interface Science*, vol. 225, pp. 146–176, 2015.

[28] J. A. Duffie, *Solar Engineering of Thermal Processes*, 3rd ed. Wiley, 2006.

[29] D. Han, Z. Meng, D. Wu, C. Zhang, and H. Zhu, "Thermal properties of carbon black aqueous nanofluids for solar absorption," *Nanoscale Res. Lett.*, vol. 6, p. 457, 2011.

[30] G. Ni, N. Miljkovic, H. Ghasemi, X. Huang, S. Boriskina, C.-T. Lin, J. Wang, Y. Xu, M. M. Rahman, T. Zhang, and G. Chen, "Volumetric solar heating of nanofluids for direct vapor generation," *Nano Energy*, vol. 17, pp. 290–301, 2015.

[31] W. Yu and H. Xie, "A Review on Nanofluids: Preparation, Stability Mechanisms, and Applications," *J Nanomater.*, vol. 2012, 2012.

[32] S. Mukherjee and S. Paria, "Preparation and Stability of Nanofluids-A Review," *J. Mech. Civ. Eng.*, vol. 9, pp. 63–69, 2013.

[33] Y. Hwang, J.-K. Lee, J.-K. Lee, Y.-M. Jeong, S.-I. Cheong, Y.-C. Ahn, and S. H. Kim, "Production and dispersion stability of nanoparticles in nanofluids," *Powder Technol.*, vol. 186, no. 2, pp. 145–153, 2008.

[34] E. Lukianova-Hleb, Y. Hu, L. Latterini, L. Tarpani, S. Lee, R. A. Drezek, J. H. Hafner, and D. O. Lapotko, "Plasmonic Nanobubbles as Transient Vapor Nanobubbles Generated around Plasmonic Nanoparticles," *ACS Nano*, vol. 4, pp. 2109–2123, 2010.

[35] Y. Zeng, J. Yao, H. Bahman Amini, K. Wang, Y. Wu, D. Li, and H. Wang, "Solar evaporation enhancement using floating light-absorbing magnetic particles," *Energy Environ. Sci.*, vol. 4, pp. 4074–4078, 2011.

[36] M. Webster, "Heat," 2017, (Accessed: 17.11.2017). [Online]. Available: https://www.merriam-webster.com/dictionary/heat

[37] Y. A. Cengel and M. A. Boles, *Thermodynamics: An Engineering Approach*, 4th ed. Tata McGraw Hill, 2011.

[38] B. Academic, "Electromagnetic radiation," 2017, (Accessed: 28.11.2017). [Online]. Available: http://academic.eb.com/levels/collegiate/article/electromagnetic-radiation/106022.

[39] "Electromagnetic spectrum," (Accessed: 02.02.2017). [Online]. Available: https://www.britannica.com/science/electromagnetic-spectrum

[40] W. L. McCabe, *Unit Operations of Chemical Engineering*, 7th ed., ser. McGraw-Hill chemical engineering series. McGraw-Hill, 2005.

[41] V. Thomsen, "Response time of a thermometer," *The Physics Teacher*, vol. 36, pp. 540–541, 1998.

[42] J. H. Lienhard, *A Heat Transfer Textbook*, 4th ed. Dover Publications, 2011.

[43] J. C. Dixon, "Appendix B: Properties of Air," in *The Shock Absorber Handbook*. John Wiley and Sons, Ltd, 2007, pp. 375–378.

[44] W. Graebel, *Advanced Fluid Mechanics*. Elsevier Science, 2007.

[45] D. Shang, *Free Convection Film Flows and Heat Transfer*. Springer, 2010.

[46] M. Rathore and R. Kapuno, *Engineering Heat Transfer*. Jones and Barlett Publishers, 2011.

[47] B. Academic, "Enthalpy," 2017, (Accessed: 12.11.2017). [Online]. Available: http://academic.eb.com/levels/collegiate/article/enthalpy/32717

[48] ——, "Thermodynamics," 2017, (Accessed: 12.11.2017). [Online]. Available: http://academic.eb.com/levels/collegiate/article/thermodynamics/108582

[49] J. Warnatz, U. Maas, and R. W. Dibble, "Thermodynamics of Combustion Processes," in *Combustion*. Springer-Verlag Berlin Heidelberg, 1999, pp. 33–48.

[50] B. Academic, "Latent heat," 2017, (Accessed: 12.11.2017). [Online]. Available: http://academic.eb.com/levels/collegiate/article/latent-heat/47272

[51] K. Soman, *Thermal Engineering*. PHI Learning Pvt. Ltd., 2011.

[52] K. A. Orlov, "WaterSteamPro," (Accessed: 02.12.2017). [Online]. Available: http://www.wsp.ru/en/default.asp

[53] S. Lee, "A study of Latent Heat of Vaporization in Aqueous Nanofluids," 2015, PhD thesis, Arizona State University.

[54] R.-H. Chen, T. X. Phuoc, and D. Martello, "Effects of nanoparticles on nanofluid droplet evaporation," *International Journal of Heat and Mass Transfer*, vol. 53, no. 19, pp. 3677–3682, 2010.

[55] M. M. Ameen, K. Prabhul, G. Sivakumar, P. P. Abraham, U. B. Jayadeep, and C. B. Sobhan, "Molecular Dynamics Modeling of Latent Heat Enhancement in Nanofluids," *Int J Thermophys*, vol. 31, no. 6, pp. 1131–1144, 2010.

[56] M. Chieruzzi, G. F. Cerritelli, A. Miliozzi, J. M. Kenny, and L. Torre, "Heat capacity of nanofluids for solar energy storage produced by dispersing oxide nanoparticles in nitrate salt mixture directly at high temperature," *Solar Energy Materials and Solar Cells*, vol. 167, pp. 60–69, 2017.

[57] W. J. Minkowycz, E. M. Sparrow, and J. P. Abraham, *Nanoparticle Heat Transfer and Fluid Flow*. CRC Press, 2016.

[58] X.-J. Wang, D.-S. Zhu, and S. Yang, "Investigation of pH and SDBS on enhancement of thermal conductivity in nanofluids," *Chemical Physics Letters*, vol. 470, no. 1, pp. 107–111, 2009.

[59] D.-H. Yoo, K. S. Hong, and H.-S. Yang, "Study of thermal conductivity of nanofluids for the application of heat transfer fluids," *Thermochim. Acta*, vol. 445, pp. 66–69, 2007.

[60] C. Zhang, S. Liu, Y. Tang, and Y. Yin, "Effects of nanoparticle clustering and alignment on thermal conductivities of Fe3O4 aqueous nanofluids," *Appl. Phys. Lett. Publ. Am. Inst. Phys.*, vol. 89, no. 2, 2006.

[61] P. Jamilpanah, H. Pahlavanzadeh, and A. Kheradmand, "Thermal conductivity, viscosity, and electrical conductivity of iron oxide with a cloud fractal structure," *Heat Mass Transfer*, vol. 53, no. 4, pp. 1343–1354, 2017.

[62] S. L. Shindé, *High Thermal Conductivity Materials*. Springer, 2006.

[63] Thermtest, "Thermal Properties Materials Database," (Accessed: 04.01.2018). [Online]. Available: https://thermtest.com/materials-database/

[64] J. F. Shackelford and W. Alexander, *Materials Science and Engineering Handbook*, 3rd ed. CRC Press, 2000.

[65] H. Patel, T. Sundararajan, and S. K. Das, "An experimental investigation into the thermal conductivity enhancement in oxide and metallic nanofluids," *Journal of Nanoparticle Research*, vol. 12, no. 3, pp. 1015–1031, 2010.

[66] S. Khosrojerdi, A. M. Lavasani, and M. Vakili, "Experimental study of photothermal specifications and stability of graphene oxide nanoplatelets nanofluid as working fluid for low-temperature Direct Absorption Solar Collectors (DASCs)," *Solar Energy Materials and Solar Cells*, vol. 164, pp. 32–39, 2017.

[67] Paisarn Naphon, "Effect of Magnetic Fields on the Boiling Heat Transfer Characteristics of Nanofluids," *Int. J. Thermophys.*, vol. 36, pp. 2810–2819, 2015.

[68] E. D. Palik, *Handbook of Optical Constants of Solids*. Academic Press, 1998.

[69] V. Khullar, H. Tyagi, N. Hordy, T. P. Otanicar, and Y. Hewakuruppu, "Harvesting solar thermal energy through nanofluid-based volumetric absorption systems," *Int. J. Heat Mass Transf.*, vol. 77, pp. 377–384, 2014.

[70] Y. A. Çengel, *Heat and Mass Transfer: Fundamentals and Applications*, 4th ed. McGraw-Hill, 2011.

[71] N. J. Hogan, A. S. Urban, C. Ayala-Orozco, A. Pimpinelli, P. Nordlander, and N. J. Halas, "Nanoparticles Heat through Light Localization," *Nano Lett.*, vol. 14, pp. 4640–4645, 2014.

[72] O. Neumann, N. J. Halas, C. Feronti, A. D. Neumann, A. Dong, K. Schell, B. Lu, E. Kim, M. Quinn, S. Thompson, N. Grady, P. Nordlander, and M. Oden, "Compact solar autoclave based on steam generation using broadband light-harvesting nanoparticles." *Proc. Natl. Acad. Sci. U. S. A.*, vol. 110, no. 29, pp. 11 677–11 681, 2013.

[73] R. A. Taylor, P. E. Phelan, R. J. Adrian, A. Gunawan, and T. P. Otanicar, "Characterization of light-induced, volumetric steam generation in nanofluids," *Int. J. Therm. Sci.*, vol. 56, pp. 1–11, 2012.

[74] T. P. Otanicar, P. E. Phelan, R. S. Prasher, G. Rosengarten, and R. A. Taylor, "Nanofluid-based direct absorption solar collector," *J. Renew. Sustain. Energy*, vol. 2, no. 3, 2010.

[75] Sigma-Aldrich, "Iron(II,III) oxide nanopowder, 50-100 nm particle size (SEM)," (Accessed: 26.11.2017). [Online]. Available: https://www.sigmaaldrich.com/catalog/product/aldrich/637106?lang=en&region=NO

[76] ——, "Sodium dodecyl sulfate BioReagent, suitable for electrophoresis, for molecular biology," (Accessed: 27.11.2017). [Online]. Available: https://www.sigmaaldrich.com/catalog/product/sigma/l3771?lang=en&region=NO

[77] K. Brautaset, *Innføring i Oljehydraulikk*. Universitetsforl., 1983.

[78] P. R. N. Childs, J. R. Greenwood, and C. A. Long, "Review of temperature measurement," *Rev. Sci. Instrum.*, vol. 71, no. 8, pp. 2959–2978, 2000.

[79] S. L. Hovden and M. E. Tennebø, "Nano-fluid i solfanger," 2017, B.Sc. thesis, Western Norway University of Applied Sciences.

[80] Halbritter, "Haloline_230V_400W_64702_ES_127-07-8_180707," 2007, (document), Osram.

[81] A. G173-03(2012), "Standard Tables for Reference Solar Spectral Irradiances: Direct Normal and Hemispherical on 37° Tilted Surface," 2012. [Online]. Available: www.astm.org

[82] C. Snow, "The Heat Capacity and Thermodynamic Properties of the Iron Oxides and Their Relation to the Mineral Core of the Iron Storage Protein Ferritin," *Theses Diss.*, 2010.

[83] X. Quan, D. Wang, and P. Cheng, "An experimental investigation on wettability effects of nanoparticles in pool boiling of a nanofluid," *International Journal of Heat and Mass Transfer*, vol. 108, pp. 32–40, 2017.

[84] Y. M. Qiao and S. Chandra, "Experiments on Adding a Surfactant to Water Drops Boiling on a Hot Surface," *R. Soc.*, vol. 453, no. 1959, pp. 673–689, 1997.

[85] M. R. Gwinn and V. Vallyathan, "Nanoparticles: Health Effects-Pros and Cons," *Environ Health Perspect*, vol. 114, no. 12, pp. 1818–1825, 2006.

[86] A. Bjørklund, "Water quality in Bergen," 2017, (document), Bergen Vann KF.

[87] G. S. Bumbrah and R. M. Sharma, "Raman spectroscopy – Basic principle, instrumentation and selected applications for the characterization of drugs of abuse," *Egyptian Journal of Forensic Sciences*, vol. 6, no. 3, pp. 209–215, 2016.

[88] Y.-S. Li and J. S. Church, "Raman spectroscopy in the analysis of food and pharmaceutical nanomaterials," *Journal of Food and Drug Analysis*, vol. 22, no. 1, pp. 29–48, 2014.

[89] D. Wei and L. Quan, "Review of Fluorescence Suppression Techniques in Raman Spectroscopy: Applied Spectroscopy Reviews:," *Appl. Spectrosc. Rev.*, vol. 50, no. 5, 2015.

[90] C. S. S. R. Kumar, *Raman Spectroscopy for Nanomaterials Characterization*. Springer Berlin Heidelberg, 2012, vol. 1.

[91] M. Picquart, "Vibrational model behavior of SDS aqueous solutions studied by Raman scattering," *J. Phys. Chem.*, vol. 90, no. 2, pp. 243–250, 1986.

[92] M. Ringnér, "What is principal component analysis?" *Nat. Biotechnol.*, vol. 26, no. 3, p. 303, 2008.

[93] R. Bro and A. K. Smilde, "Principal component analysis," *Anal. Methods*, vol. 6, no. 9, pp. 2812–2831, 2014.

[94] B. Weiner, "What is a Continous Particle Size Distribution?" 2011. [Online]. Available: http://www.brookhaveninstruments.com/pdf/What%20is%20a%20Continuous%20Particle%20Size%20Distribution.pdf

[95] SNL, "Støv - Store norske leksikon," 2017, (Accessed: 08.12.2017). [Online]. Available: https://snl.no/st%C3%B8v

[96] B. Truong, L.-w. Hu, J. Buongiorno, and T. McKrell, "Modification of sand-blasted plate heaters using nanofluids to enhance pool boiling critical heat flux," *International Journal of Heat and Mass Transfer*, vol. 53, no. 1, pp. 85–94, 2010.

[97] S. Vafaei, A. Purkayastha, A. Jain, G. Ramanath, and T. Borca-Tasciuc, "The effect of nanoparticles on the liquid–gas surface tension of Bi2Te3 nanofluids," *Nanotechnology*, vol. 20, no. 18, 2009.

[98] L. Xu and J. Xu, "Nanofluid stabilizes and enhances convective boiling heat transfer in a single microchannel," *International Journal of Heat and Mass Transfer*, vol. 55, no. 21, pp. 5673–5686, 2012.

[99] S. Vafaei and D. Wen, "Flow boiling heat transfer of alumina nanofluids in single microchannels and the roles of nanoparticles," *J. Nanoparticle Res.*, vol. 13, no. 3, pp. 1063–1073, 2011.

[100] J. P. Holman, *Experimental Methods for Engineers*, 6th ed., ser. Special Issue on Measurement in Turbulent Flow. McGraw-Hill, 1994, vol. 9.

Appendices

A. Uncertainty calculations

The following equations were used for the uncertainty calculations in the experimental results.

Mean

The mean value $\bar{x}$ of independent variables can be calculated by the following equation:

$$\bar{x} = \frac{x_1 + x_2 + x_3 + ... + x_N}{N} = \frac{1}{N}\sum_{i=1}^{N} x_i \tag{A.1}$$

Standard deviation

Population standard deviation is

$$S = \sqrt{\frac{1}{N}\sum_{i=1}^{N}(x_i - \bar{x})^2}, \tag{A.2}$$

where N is the number of values within a data set.

Independent variables

If the quantity of an experimental result f is calculated by independent variables x, y, z..., i, with corresponding uncertainties S_x, S_y, S_z, ... , S_i , the uncertainty is given by:

$$S_f = \sqrt{\left(\frac{\delta f}{\delta x}S_x\right)^2 + \left(\frac{\delta f}{\delta y}S_y\right)^2 + \left(\frac{\delta f}{\delta z}S_z\right)^2 + ... + \left(\frac{\delta f}{\delta i}S_i\right)^2} \tag{A.3}$$

where S_f is the standard deviation of the result f.

B. Nanofluid boiling graphs I

Presented figures are established from experiments described in section 4.2 and section 4.3.

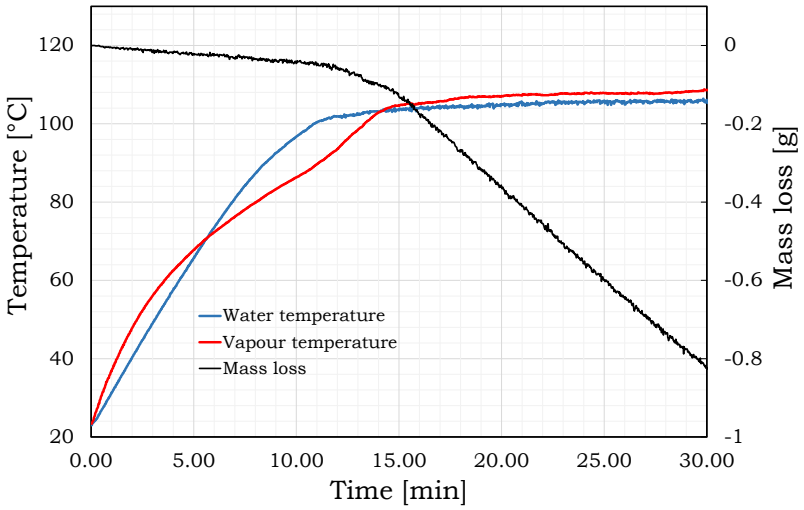

Figure B.1: Boiling of water.

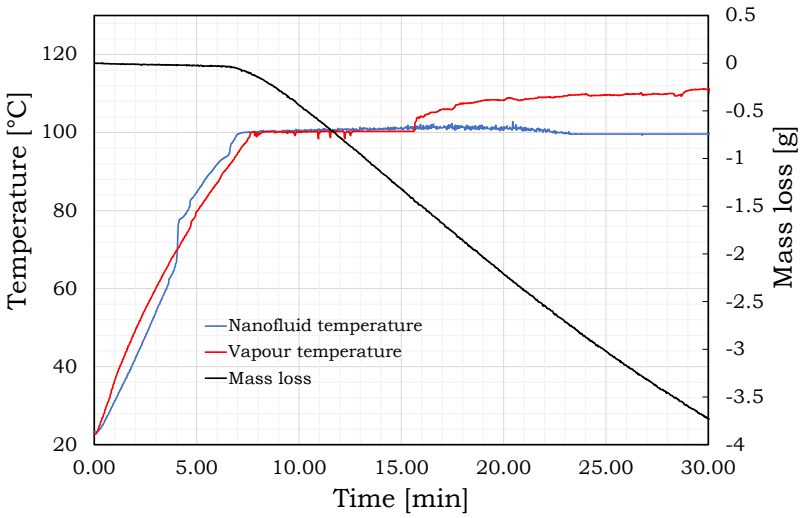

Figure B.2: Boiling of 0.50 wt.% CB NF

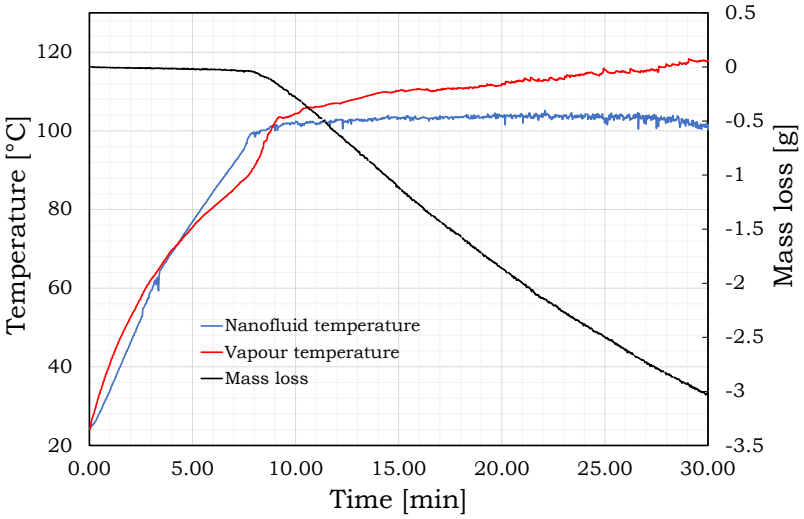

Figure B.4: Boiling of 0.10 wt.% CB NF

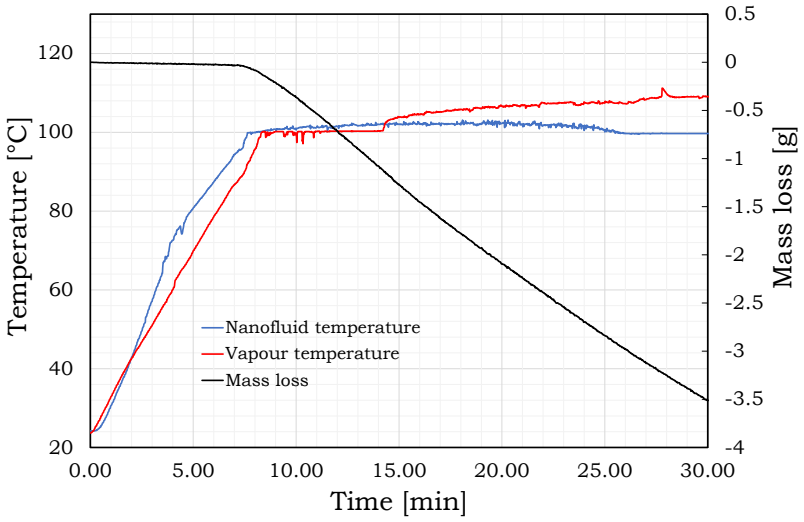

Figure B.5: Boiling of 0.25 wt.% CB NF

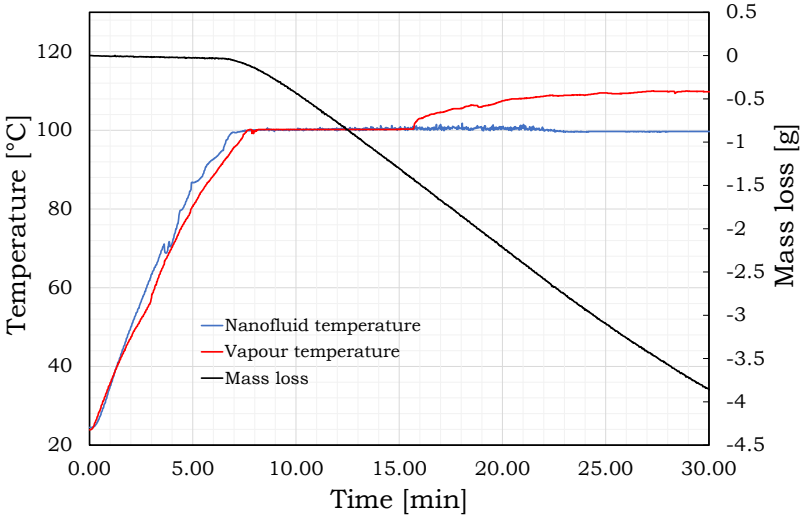

Figure B.3: Boiling of 0.95 wt.% CB NF

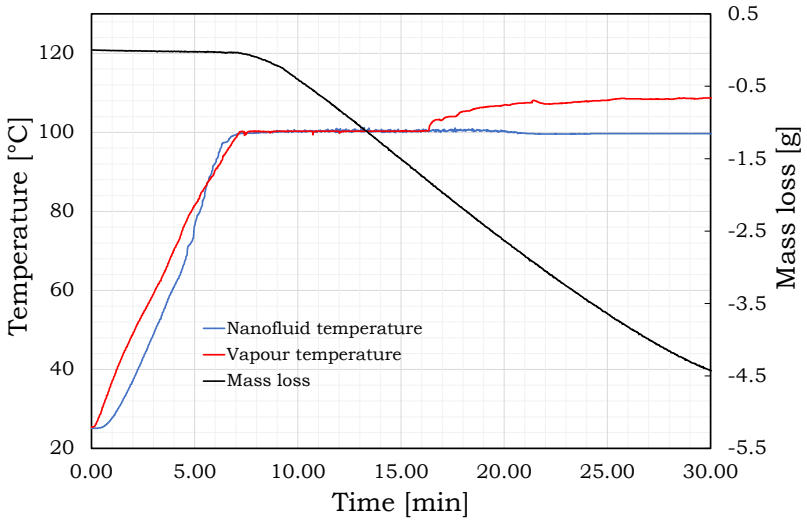

Figure B.6: Boiling of 2.00 wt.% CB NF

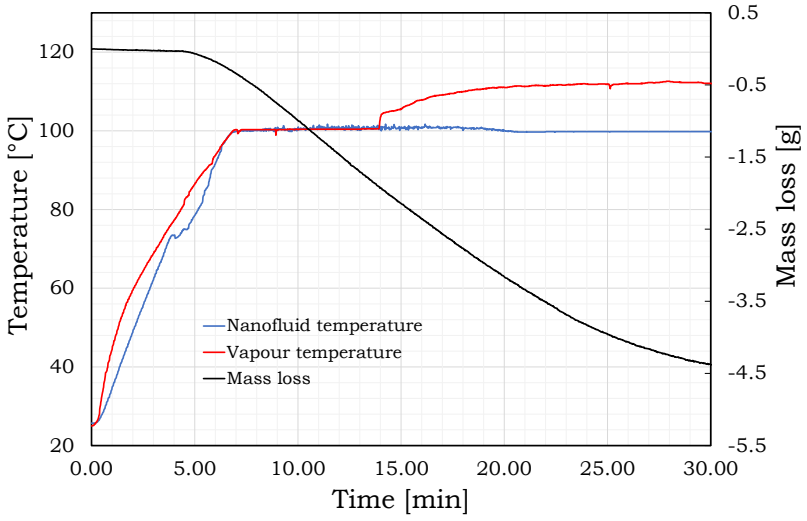

Figure B.7: Boiling of 3.00 wt.% CB NF

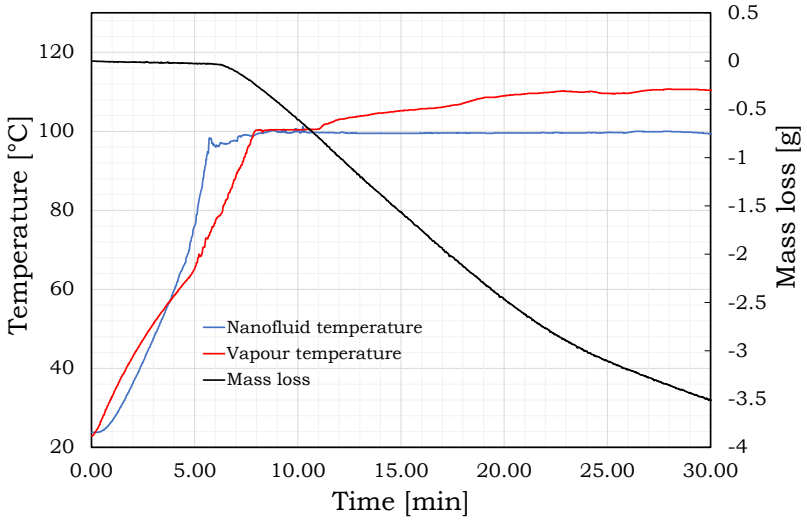

Figure B.8: Boiling of 4.00 wt.% CB NF

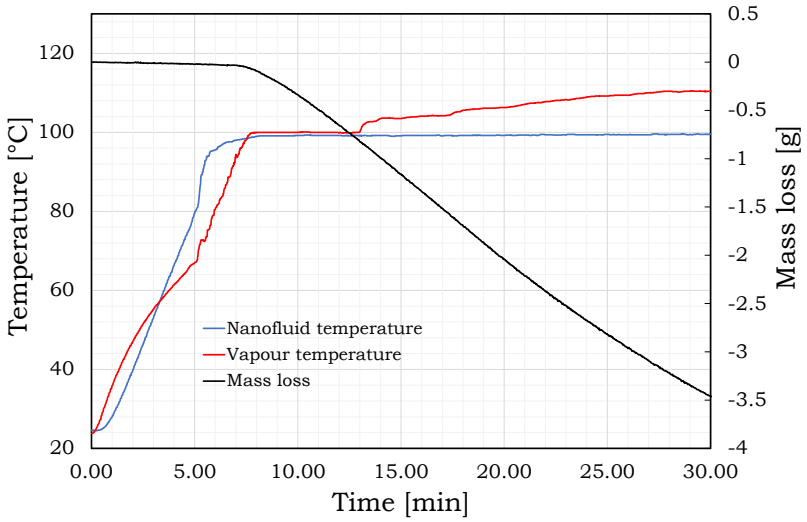

Figure B.9: Boiling of 5.00 wt.% CB NF

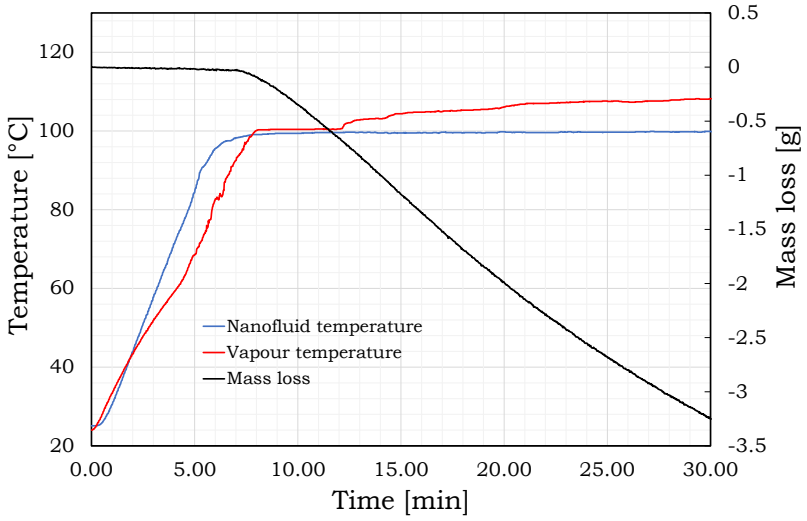

Figure B.10: Boiling of 10.00 wt.% CB NF

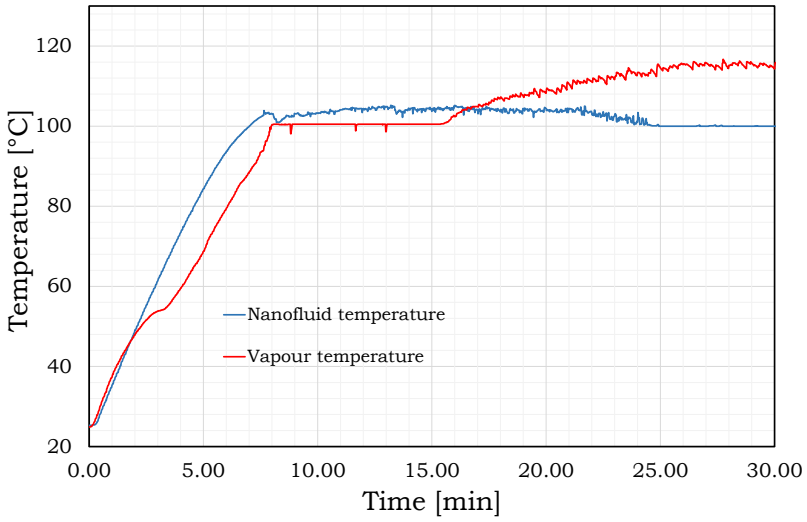

Figure B.11: Boiling of 0.50 wt.% CB NF with SDS.

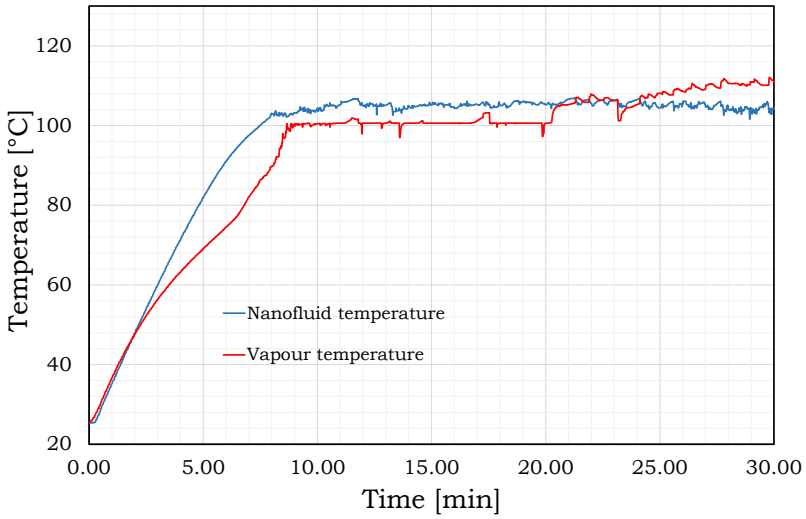

Figure B.13: Boiling of 0.10 wt.% CB NF with SDS.

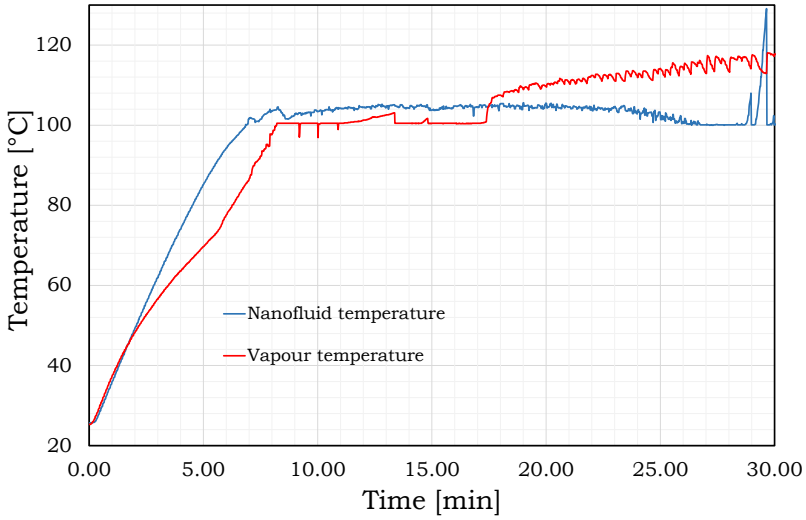

Figure B.14: Boiling of 0.25 wt.% CB NF with SDS.

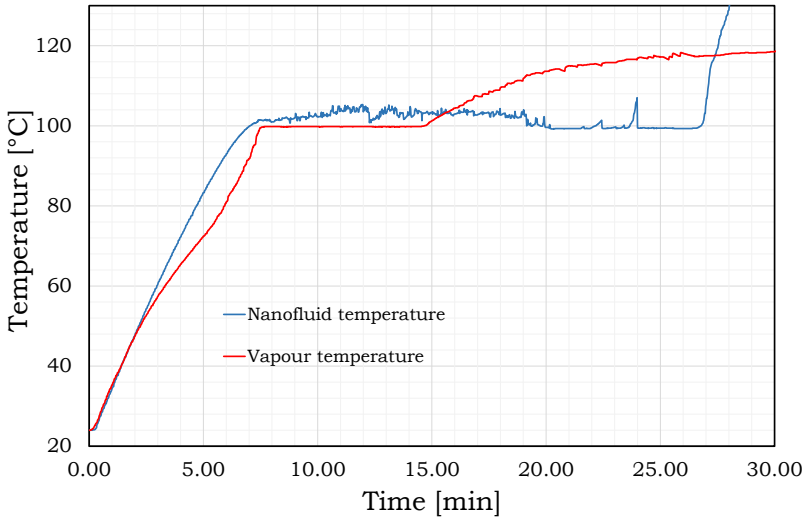

Figure B.12: Boiling of 0.95 wt.% CB NF with SDS.

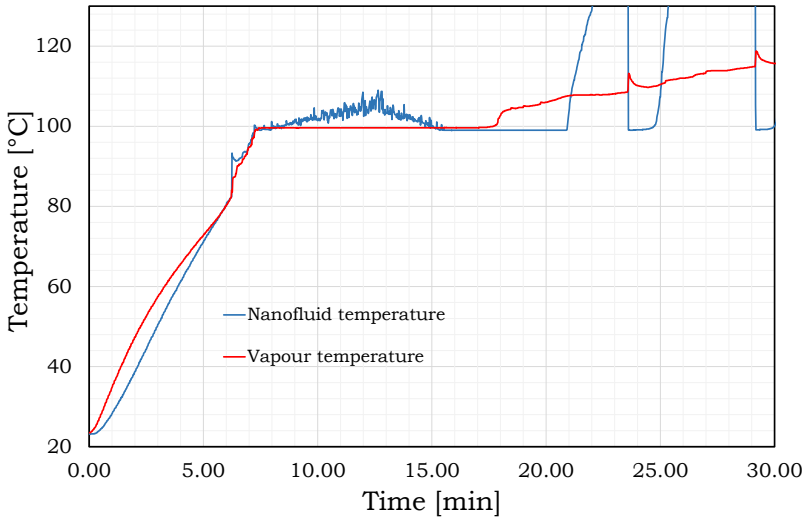

Figure B.15: Boiling of 2.00 wt.% CB NF with SDS.

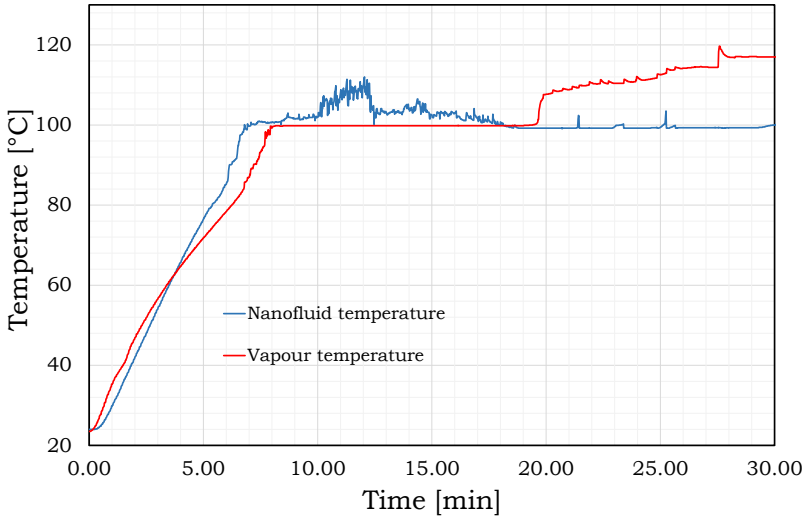

Figure B.16: Boiling of 3.00 wt.% CB NF with SDS.

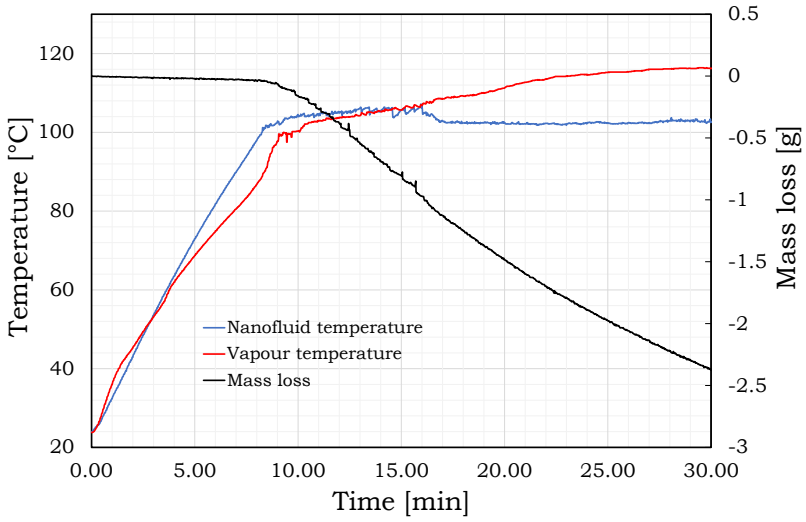

Figure B.17: Boiling of 0.10 wt.% IO NF.

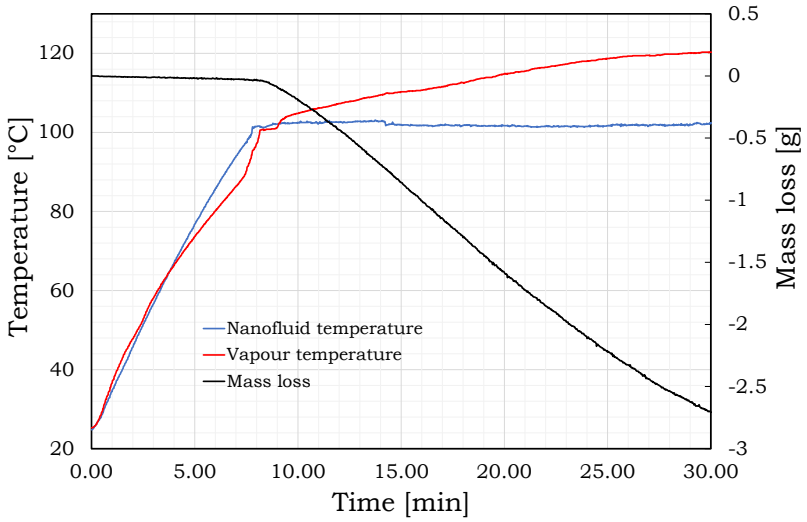

Figure B.18: Boiling of 0.25 wt.% IO NF.

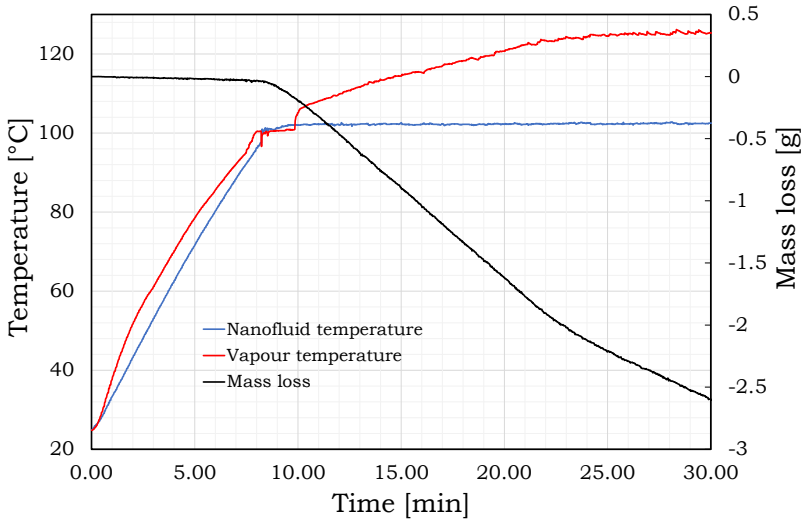

Figure B.19: Boiling of 0.50 wt.% IO NF.

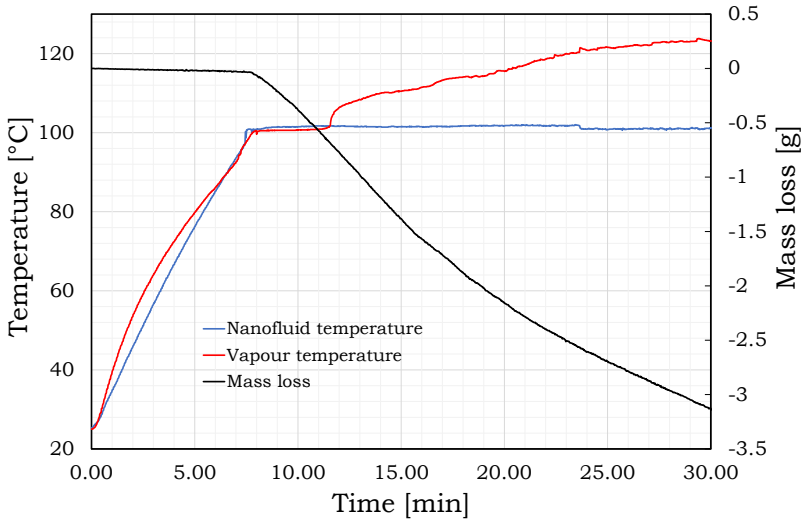

Figure B.20: Boiling of 0.95 wt.% IO NF.

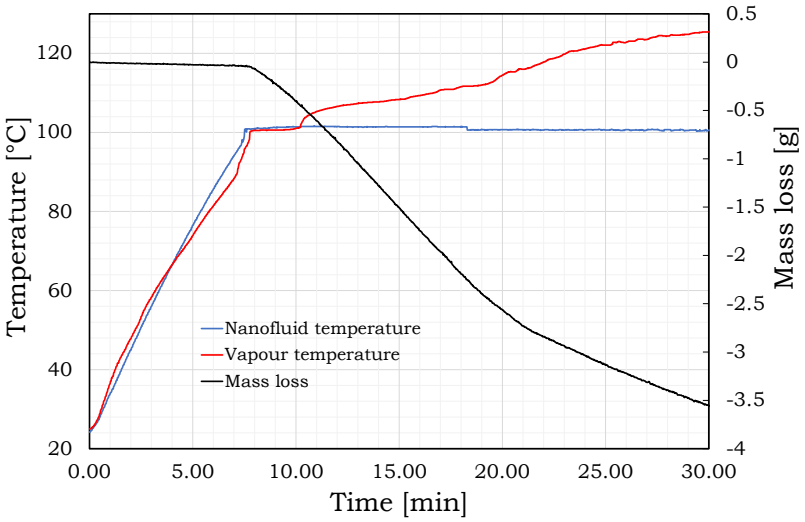

Figure B.21: Boiling of 2.00 wt.% IO NF.

C. Nanofluid boiling graphs II

Presented figures are established from experiments described in section 4.4.

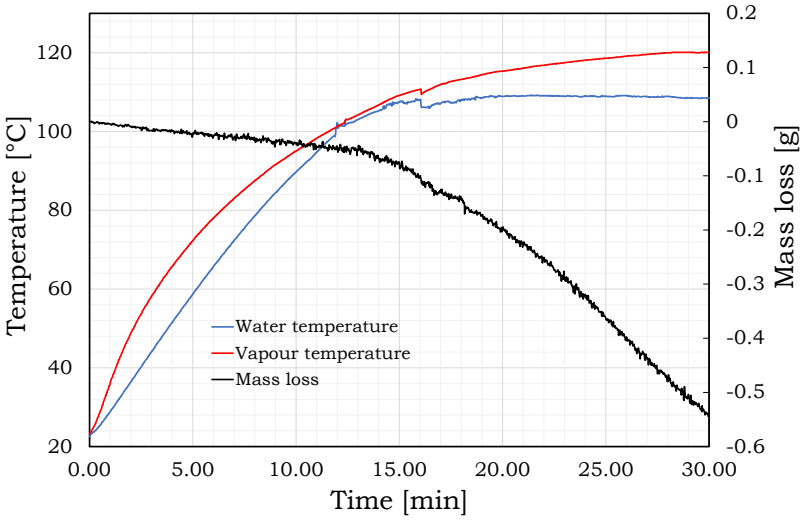

Figure C.1: Boiling of distilled water.

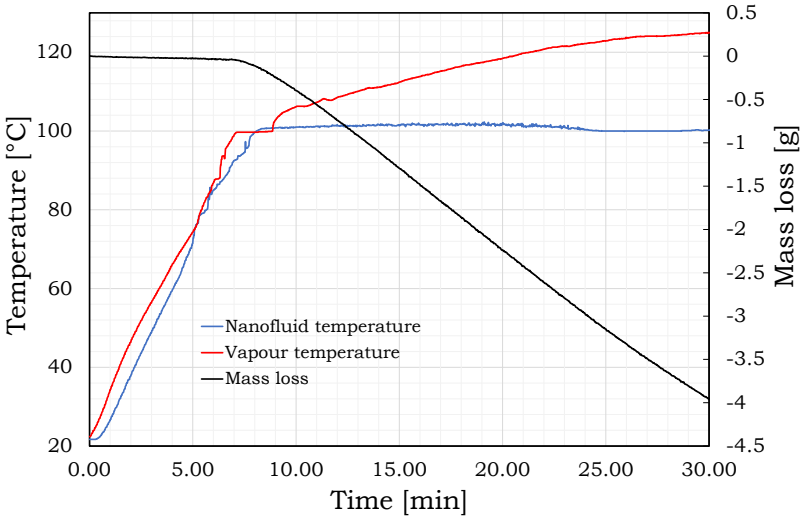

Figure C.2: Boiling of 2.00 wt.% CB NF without SDS.

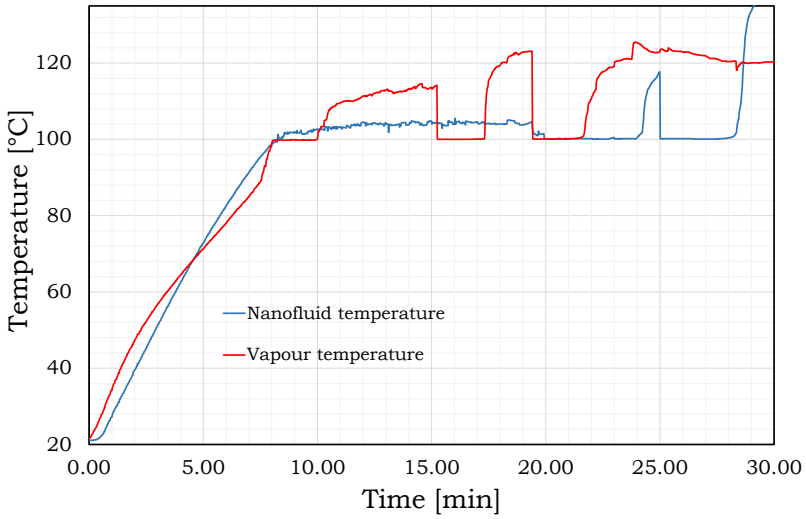

Figure C.3: Boiling of 2.00 wt.% CB NF with SDS.

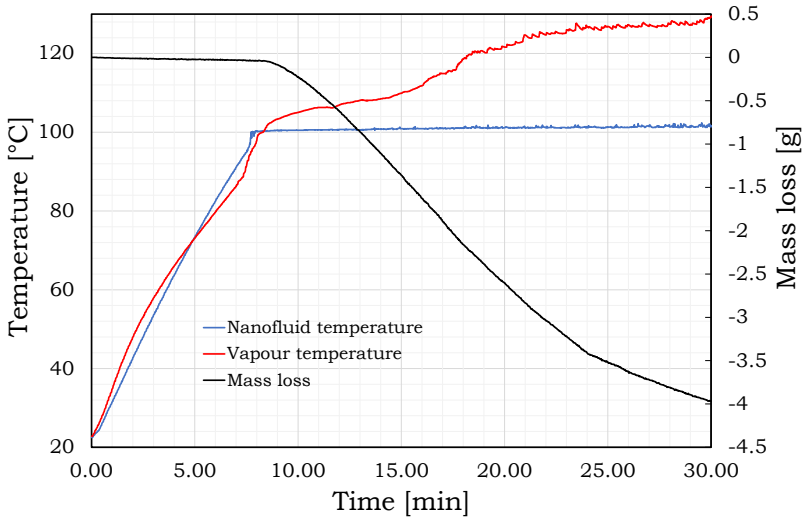

Figure C.4: Boiling of 2.00 wt.% IO NF.

D. SEM images

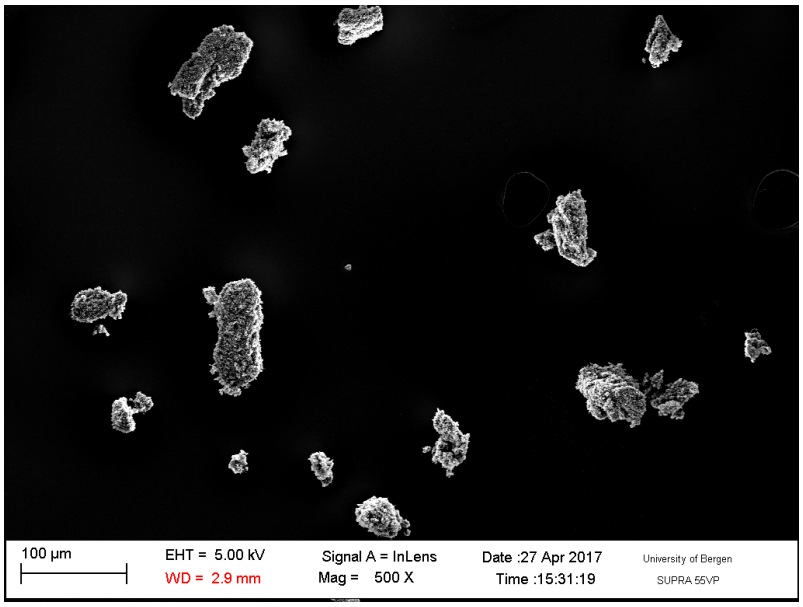

Figure D.1: SEM image of CB NPs.

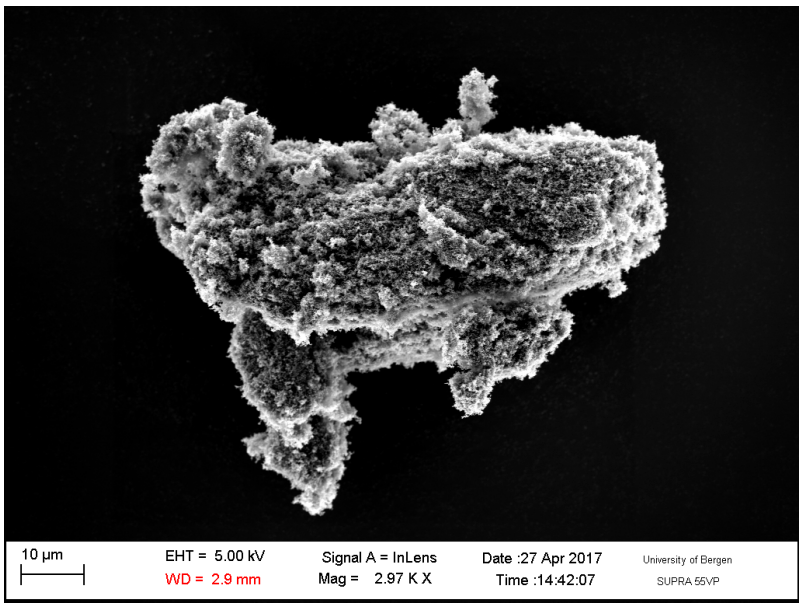

Figure D.2: SEM image of CB NPs.

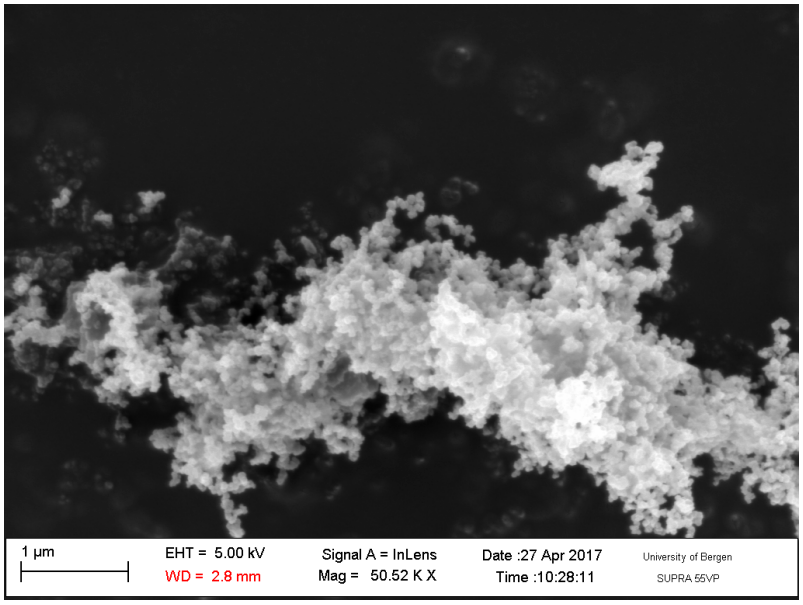

Figure D.3: SEM image of CB NPs.

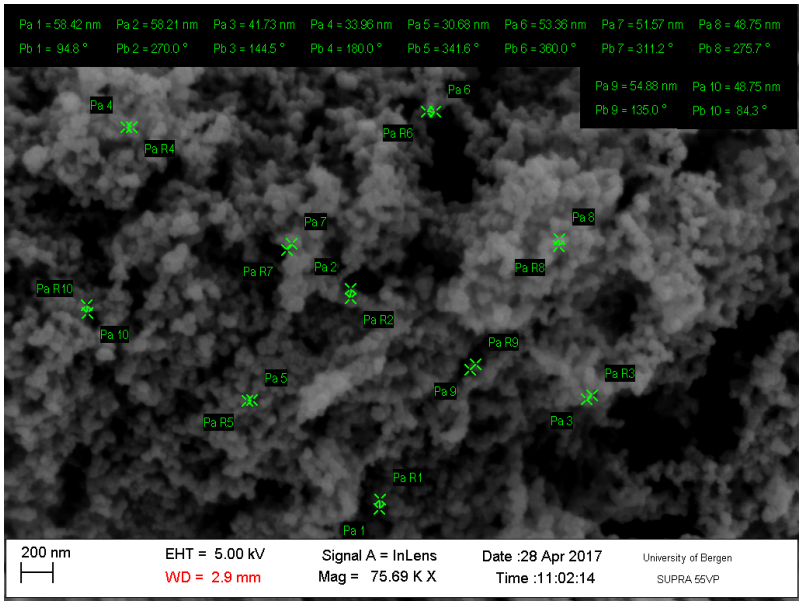

Figure D.4: SEM image of CB NPs.

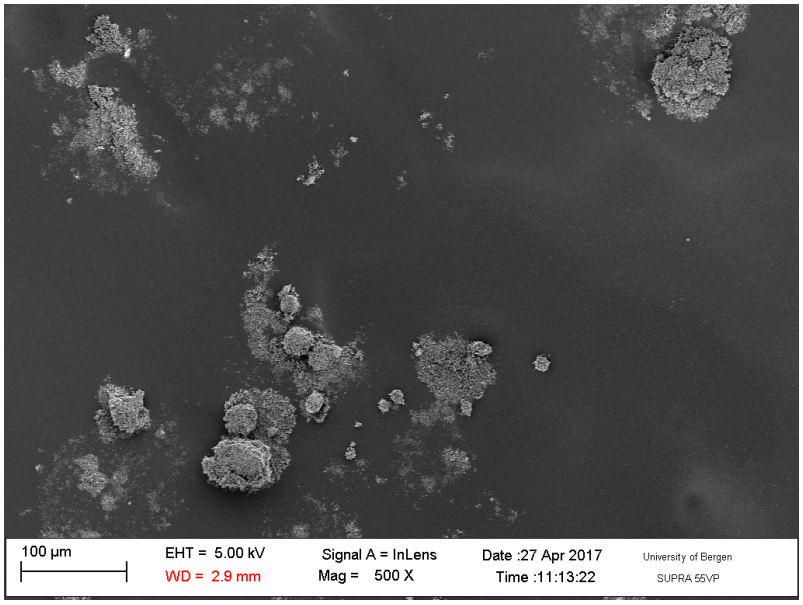

Figure D.5: SEM image of IO NPs.

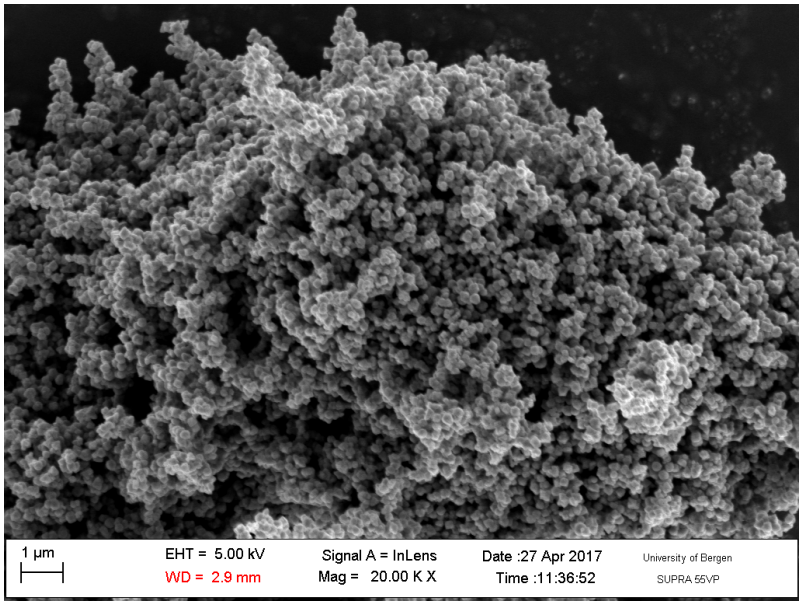

Figure D.6: SEM image of IO NPs.

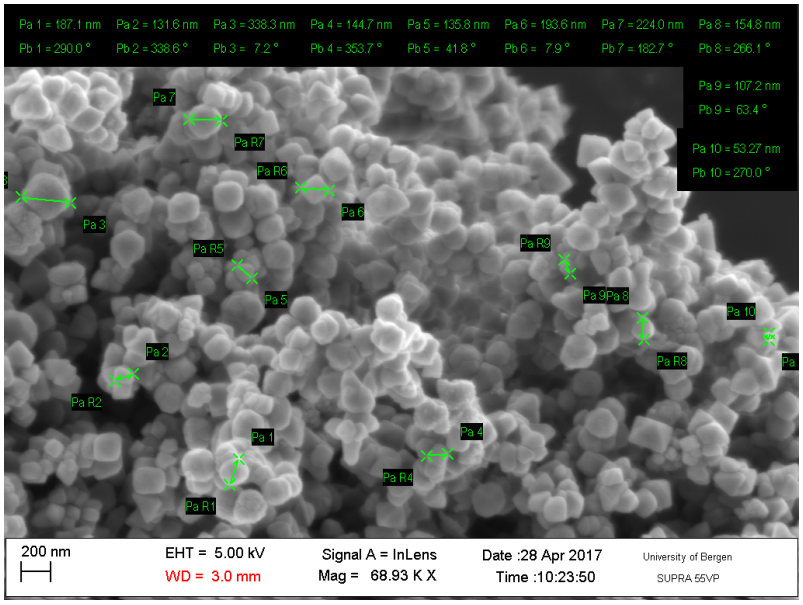

Figure D.7: SEM image of IO NPs.

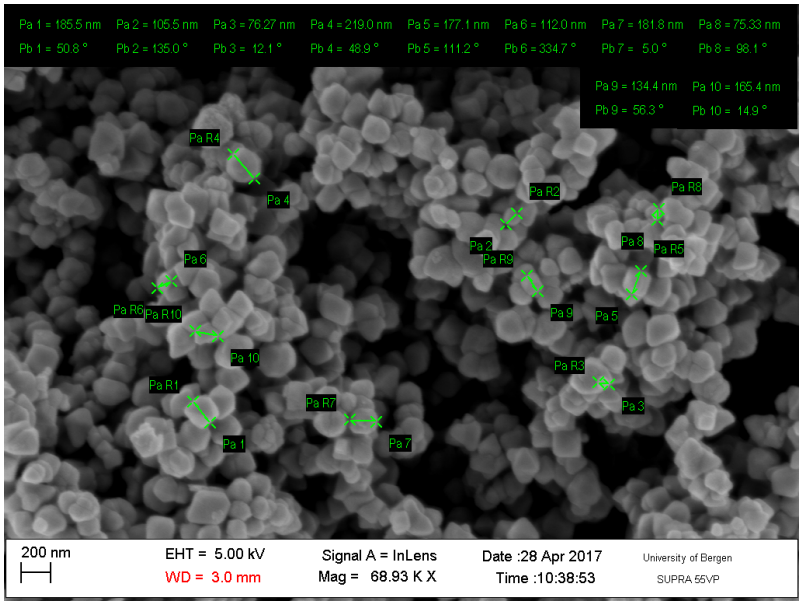

Figure D.8: SEM image of IO NPs.

E. Response time

E.0.1 Response time of a thermometer

The first law of thermodynamics, $E_{internal} = Q - W$, is the basis of calculating the RT of a thermometer [41]. The energy from the surrounding fluid of a thermometer equals the internal energy gained by the thermometer. The internal energy of a thermometer is given by the one dimensional heat equation: $E_{internal} = mC_p\Delta T$. The energy from the liquid considers heat transferred by convection, see Newton's law of cooling Eq. (2.2), and neglects conduction and radiation.

Combining the one dimensional heat equation and Eq. (2.2) in the first law of thermodynamics we obtain:

$$m\,C_p\,\frac{dT}{dt} = hA\,(T_s - T). \tag{E.1}$$

Collecting the constants from the energy balance (E.1) results in:

$$\tau = \frac{mC_p}{hA}. \tag{E.2}$$

Substituting Eq. (E.2) in Eq. (E.1) yields:

$$\frac{dT}{dt} = \frac{(T_s - T)}{\tau}. \tag{E.3}$$

Eq. (E.3) is a first order linear differential equation. At the time $t = 0$, the ambient temperature $T_\infty = T$. The solution is:

$$T = T_s - (T_s - T_\infty)\,e^{-t/\tau}. \tag{E.4}$$

With the assumption $T_\infty = 0$, the temperature T is:

$$T = T_s\,(1 - e^{-t/\tau}). \tag{E.5}$$

At the time $t = \tau$ the time constant is found:

$$T = 63.21\,\%\,T_f. \tag{E.6}$$

The RT is therefore 63.21% of the time it takes for the thermometer to reach the final temperature, T_f [41, 77]. Eq. (E.2) shows that the RT is dependent upon the mass, i.e. the density and volume of the junction in the thermocouple [100].

E.0.2 Response time measurements

In order to perform correct and reliable temperature measurements, a variety of temperature sensors were investigated. RT of the different sensors in water and in air was found through experiments, and is here presented as supplementary information.

The final temperature was defined as 98% of the temperature change in all graphs. The RT is given in table 3.1 and 3.2.

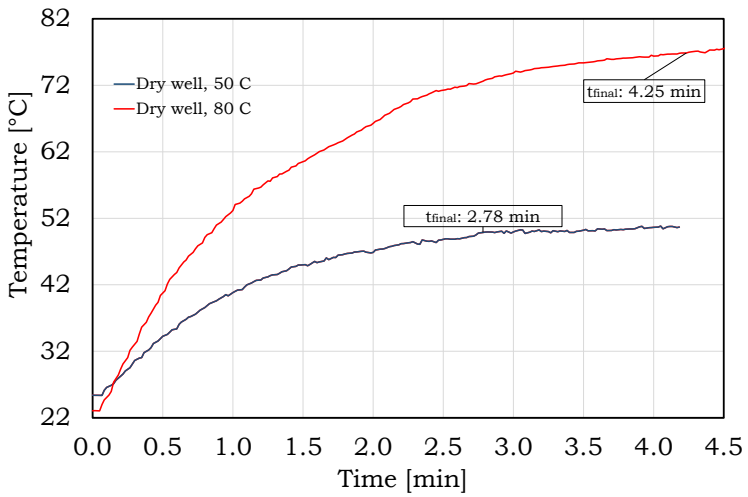

Figure E.1: NTC-thermistor from Vellemann, response time in air from room temperature to 50°C and 80°C.

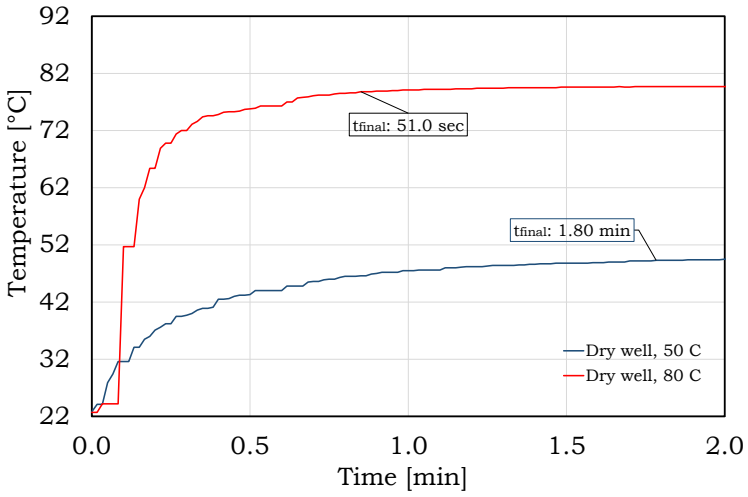

Figure E.2: T-type thermocouple, response time in air from room temperature to 50°C and 80°C.

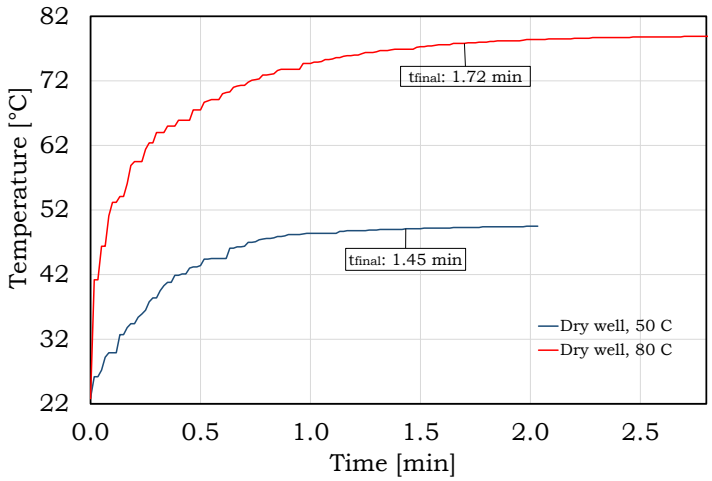

Figure E.3: K-type thermocouple, response time in air from room temperature to 50°C and 80°C.

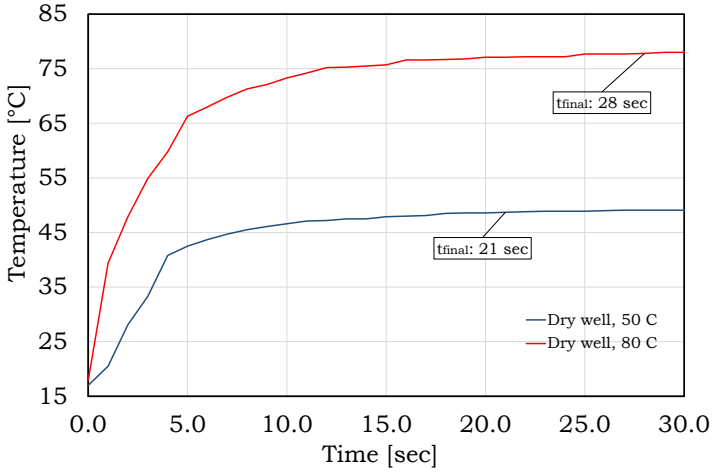

Figure E.4: T-type thermocouple from Omega, response time in air from room temperature to 50°C and 80°C.

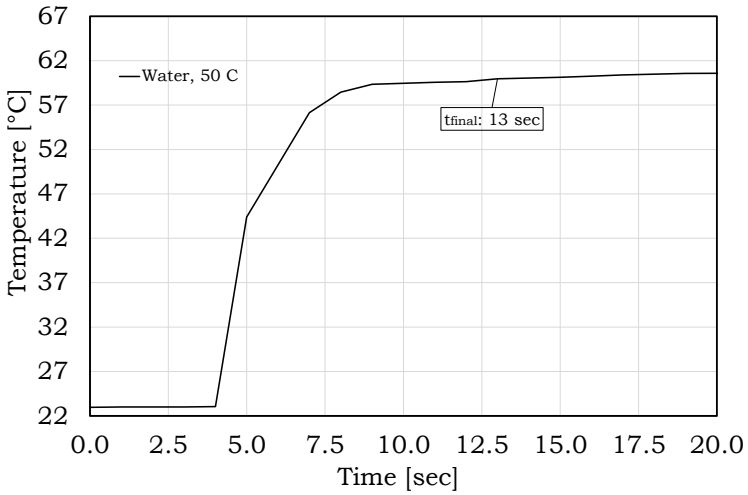

Figure E.5: NTC-thermistor from Vellemann, water response time (50°C).

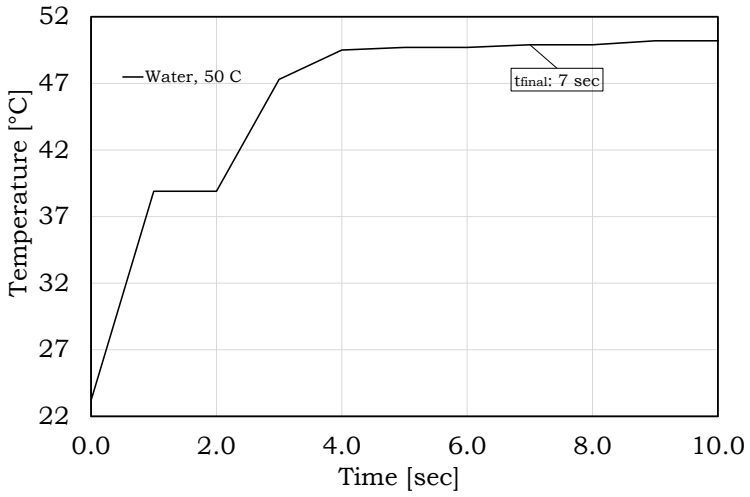

Figure E.6: T-type thermocouple, water response time (50°C).

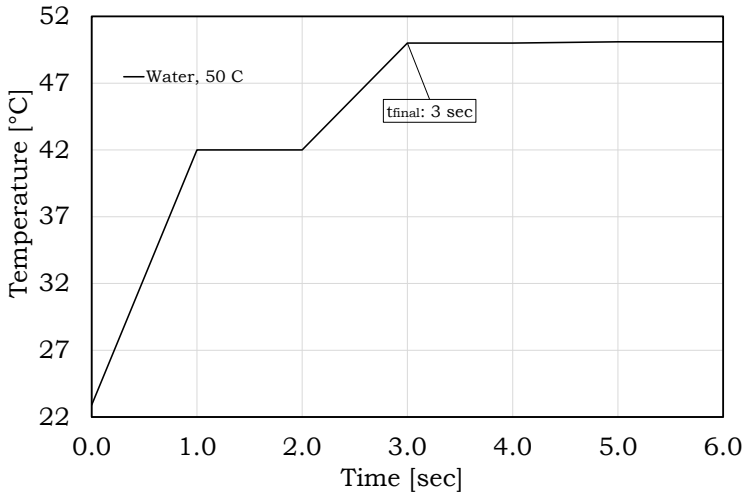

Figure E.7: K-type thermocouple, water response time (50°C).

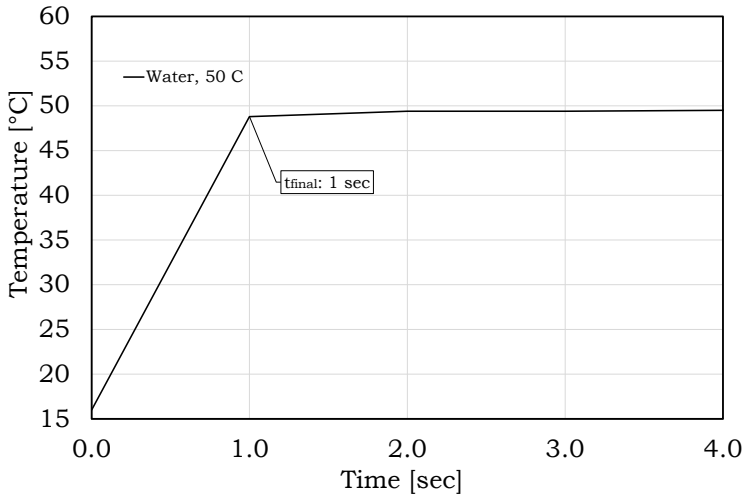

Figure E.8: T-type thermocouple from Omega, water response time (50°C).

F. Tap water reference data

Tap water quality in Bergen from Bjørklund [86]:

Kvalitet på vann levert fra Svartediket vannbehandlingsanlegg i 2017.
Svartediket forsyner normalt sett til Bergen sentrum.
Det forsyner også vestre deler av Bergen sammen med Espeland,
og områdene Kokstad, Hjellestad/Milde og Skjold/Nordås sammen med Kismul og Espeland.

Tabell 1
Analyseresultat fra rentvann ved Svartediket vannbehandlingsanlegg i perioden 1.1.2017 – 31.12.2017.
Analysene er utført ved ALS sine laboratorier.

Parameter	Enhet	Snitt	Maks	Min	Antall	Drikkevannsforskriftens grenseverdi
1.2-dikloretan	µg/l	0,75	0,75	0,75	2	3
Aluminium	µg/l Al	34	43	26	5	200
Ammonium	µg/l NH4-N	11,8	20,0	4,0	5	500
Antimon	µg/l Sb	0,012	0,013	0,012	2	5
Arsen	µg/l As	0,025	0,025	0,025	2	10
Benzen	µg/l C6H6	0,20	0,20	0,20	2	1
Benzo(a)pyren	µg/l	0,002	0,002	0,002	2	0,01
Bly	µg/l Pb	0,01	0,01	0,01	2	10
Bor	µg/l B	10	10	10	2	1000
Cyanid	µg/l CN	5,00	5,00	5,00	2	10
Fluorid	mg/l F	0,11	0,20	0,02	2	1,5
Jern	µg/l Fe	11,19	40,00	2,04	5	200
Kadmium	µg/l Cd	0,006	0,007	0,005	2	5
Klorid	mg/l Cl	9,73	10,40	9,05	2	200
Konduktivitet	mS/m	11,7	12,6	10,7	34	250
Kopper	µg/l Cu	0,500	0,500	0,500	2	100
Krom	µg/l Cr	0,01	0,01	0,01	2	50
Kvikksølv	µg/l Hg	0,001	0,001	0,001	2	0,5
Mangan	µg/l Mn	5,70	6,64	4,76	2	50
Natrium	mg/l Na	4,44	4,68	4,20	2	200
Nikkel	µg/l Ni	0,606	0,657	0,554	2	20
Nitrat	mg/l NO3-N	0,10	0,10	0,10	1	10
Nitritt	µg/l NO2-N	2,0	2,0	2,0	1	50
Surhet	pH	8,2	8,3	8,1	34	6,5-9,5
Selen	µg/l Se	0,500	0,500	0,500	2	10
Sulfat	mg SO4/l	6,90	7,25	6,54	2	100
Tetrakloreten	µg/l	0,20	0,20	0,20	2	
1.1.2-Trikloreten	µg/l	0,10	0,10	0,10	2	
Sum 1.1.2-Trikloreten og tetrakloreten	µg/l	0,30	0,30	0,30	2	10
TOC	mg/l C	0,58	0,72	0,48	21	5
Glyfosat	µg/l	0,050	0,050	0,050	2	0,1
Ampa	µg/l	0,050	0,050	0,050	2	0,1
MCPA	µg/l	0,020	0,020	0,020	2	0,1
Mecoprop	µg/l	0,010	0,010	0,010	2	0,1
Fluoroxipyr	µg/l	0,010	0,010	0,010	2	0,1
Plantevernmidler totalt	µg/l	0,140	0,140	0,140	2	0,5
Benzo(ghi)perylen	µg/l	0,003	0,003	0,003	2	
Benzo(b)flouranten	µg/l	0,004	0,004	0,004	2	
Indeno(1.2.3-cd)pyren	µg/l	0,003	0,003	0,003	2	
Benzo(k)flouranten	µg/l	0,002	0,002	0,002	2	
Sum PAH(4)	µg/l	0,0120	0,0120	0,0120	2	0,1
Triklormetan	µg/l	0,30	0,30	0,30	2	
Tribrommetan	µg/l	0,20	0,20	0,20	2	
Dibromklormetan	µg/l	0,10	0,10	0,10	2	
Bromdiklormetan	µg/l	0,10	0,10	0,10	2	
Sum Trihalometaner	µg/l	0,70	0,70	0,70	2	50
Monoetylenglykol	µg/l C	10,00	10,00	10,00	1	10
Dietylenglykol	µg/l C	10,00	10,00	10,00	1	10
Trietylenglykol	µg/l C	10,00	10,00	10,00	1	10
Propylenglykol	µg/l C	10,00	10,00	10,00	1	10

G. Short communication, submitted to *Applied Thermal Engineering*

Attached article presents selected results from this thesis and contains additional results of CB NF boiling in a parabolic collector.

Solar steam in an aqueous carbon black nanofluid

Edda T. Ulset[a], Pawel Kosinski[a], Boris V. Balakin[b,c,*]

[a] *University of Bergen, Dept. Phys. Tech., Norway*
[b] *NRNU Moscow Engineering Physics Institute, Dept. Therm. Phys., Russia*
[c] *Western Norway University of Applied Sciences, Dept. Mech. Mar. Eng., Bergen, Norway*

Abstract

A limited number of experimental studies report intensive steam generation in direct adsorption solar collectors with nanofluids. Most nanofluids used for these applications are produced with expensive gold nanoparticles. This contribution proposes a low-cost alternative solution made of water and carbon black nanoparticles. Our nanofluid-generated steam is produced in a parabolic collector with 73% efficiency and 25°C superheat under the solar conditions in the Nordic region.

Keywords: nanofluid, solar steam, boiling, solar collector, carbon black

1. Introduction

The most successful attempts of sun-enabled, *in-situ* steam generation of nanofluids (NF) were reported less than decade ago. Using low-concentration aqueous suspensions of golden nanoparticles (NP), they demonstrated evaporation efficiency of around 80% [1, 2] and relatively high steam temperature (120-130°C) [3]. These experiments were carried out in regions with excessive solar resources. This raises questions about the possibility of utilizing the technology in a moderate climate. The practical applicability of the process is also strongly criticized because of the high cost of gold NPs and lack of information on potential toxicity of the solar steam that may contain NPs. An alternative solution [4] was proposed by Ni et.al. based on carbon black (CB) NPs, studying different CBNFs under artificial radiation. Nevertheless, the degree of light concentration and volume fraction of the particles were insufficient to obtain notable superheat while still providing reasonable evaporation efficiency of 60%. In this study, we investigate a low-cost and solar steam-efficient application based on CBNF with different composition.

2. Experiments

Our nanofluid was produced mixing CBNPs (ENSACO 350G) and water from the Bergen communal municipal network (S.0). ImageJ processing of TEM-scans of dry CBNPs returns

*corresponding author
Email address: Boris.Balakin@hvl.no (Boris V. Balakin)

51±17 nm mean particle size (see Fig. S.1.1 in the supplementaries). NF samples were homogenized using Branson 3510 ultrasonic bath (320 W). CBNF optimum composition was selected in a series of lab-scale experiments on photo-thermal evaporation of the fluid.

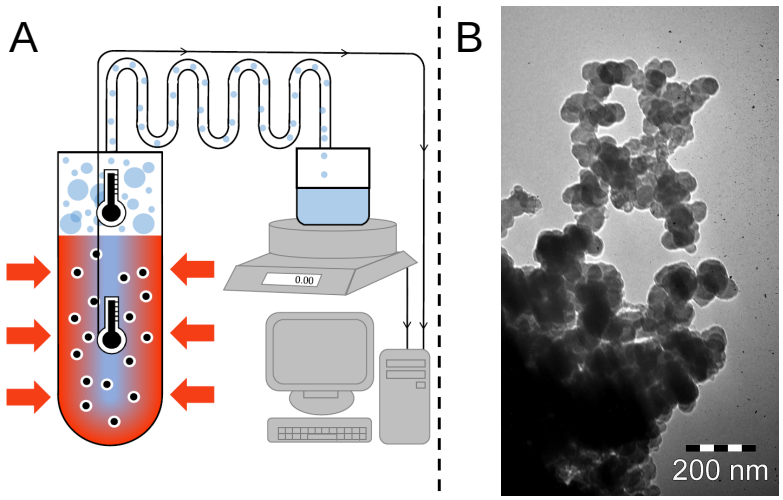

Figure 1: A: Experimental set-up. B: TEM of CBNPs

The laboratory set-up (Fig. 1A) consisted of a transparent glass tube (ID 14 mm, height 148 mm), connected via PVC-pipe to a condensate collector. A 5-ml sample of CBNF was heated in the light of two halogen lamps OSRAM (400 W), delivering 5.5 kW/m^2 each (Fig. S.2). The 300-nm shift to the red region relative to the solar spectrum was detected for the lamp. The measurement system included two thermocouples Omega(T) (±0.3°) and the scale Sartorius CPA 324S (±0.1 mg). The thermocouples were placed in the bulk of CBNF and the steam, respectively.

Once the optimum composition was found, a 1-l batch of CBNF was produced for the solar collector test (see the graphical abstract). Here the nanofluid, poured in a round-bottom flask, was placed in the focus of a 1.5-m^2 parabolic collector (concentration ratio 64, Marsrock). Temperature of the solar steam was controlled with a ST-9215C-300 thermistor (±0.1°C). The concentrator test was run at 60°22'06.5"N and 5°21'07.9"E in the summer of 2017. The environmental conditions, recorded by the meteo-station ≈ 2 km from the site of the experiment, are shown in the supplementaries (Figs. S.3.1-S.3.5).

3. Results and discussion

3.1. Artificial illumination

Figure 2 illustrates the dynamics of photo-thermal boiling of 3wt% CBNF during lab-scale experiments. In this test we detected no signs of early sub-cooled boiling as reported by Neumann et.al. [1]: the fluid gradually reaches saturation after about 7 min. The system most possibly follows the heating scenario proposed by Ni et.al. [4], where trapping thermal boundary layers for individual nanoparticles was proposed as the driving force. Following our visual observations (video 1), CBNF starts boiling at the saturation temperature.

Evaporation of CBNF down to 58% of initial sample volume compacts the solution. The inter-particle separation distance reduces so the steam bubbles gain superheat slightly over 11 K, i.e. twice larger the superheat for 5.5 kW/m^2 from the conventional water boiling curve. In Ni et.al. [4] the equivalent superheating was not demonstrated at 5-10 sun. Following our CFD-estimates (STAR-CCM+), the system gauge pressure never exceeded 2 kPa, so that this temperature cannot be explained by pressurization of the steam.

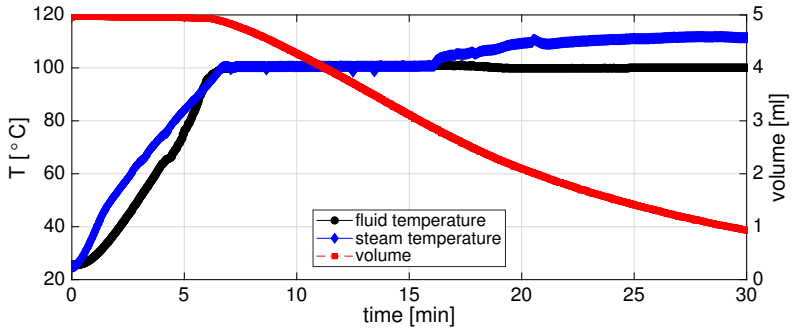

Figure 2: Lab-scale experiment log

The condensate samples, studied with FRITSCH ANALYSETTE 22, contained no traces of nanoparticles; the particle size distribution from the condensate matched the sizes observed in pure water, used for CBNF production (Figs. S.4.1-S.4.2). The condensate from a reference sample of Fe_2O_3 nanofluid with the same volume fraction of heavier NPs (184±55 nm) was contaminated (Fig. S.4.3). We attribute this observation to different wettability of the compared NPs.

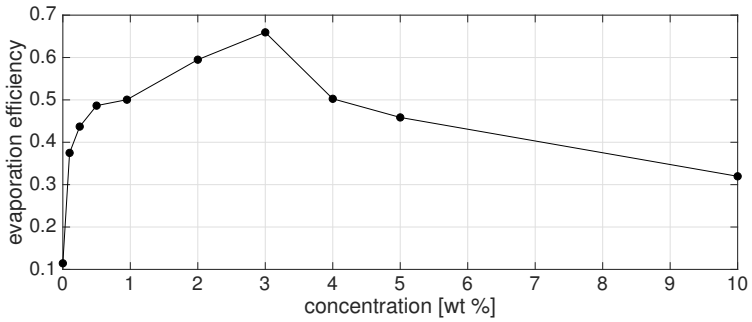

Figure 3: Evaporation efficiency

The evaporation efficiency of the process is presented against CBNP concentration in Fig. 3. Following [4], this parameter is defined as the ratio of the amount of heat utilized for CBNF evaporation and superheating of produced steam to in-coming heat. Screening the composition, we observed maximum at 3 wt%, below which the addition of new particles increased heating and the number of nucleation sites. The penetration depth does reduce with concentration and, passing the optimum, CPNPs limit photo-thermal exposure of the bulk.

3.2. Solar concentrator test

An experimental log from the solar concentrator study at 0.76±0.04 sun is shown in Fig. 4 (video 2). Here the volume of the sample was defined by processing with ImageJ digital photos taken at different stages of the process. Unlike the heating in the laboratory system, CBNF was superheated up to 25°C without temporal delay at saturation conditions. The superheat was in the interval reported by Neumann et.al. [3] for a similar solar steam system with Au-Si NPs. This value again does not correspond to the conventional boiling curve. The evaporation efficiency is estimated as 73%, which is comparable with the results reported by [1, 2].

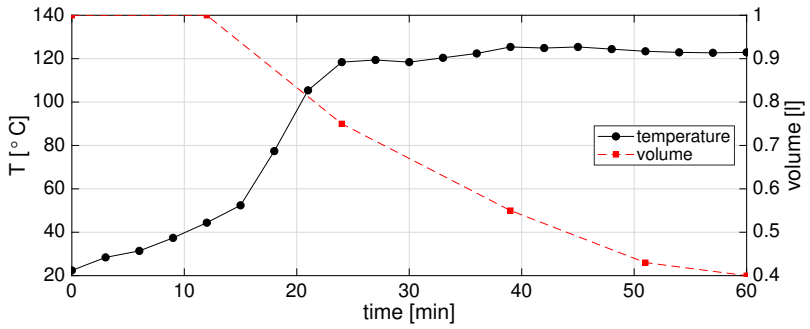

Figure 4: Concentrator experiment log

4. Conclusions

This paper describes laboratory experiments on solar steam generation in CBNF at 11 sun. Screening NF composition, we detected maximum evaporation efficiency at 3wt%. Solar steam condensate was free of nanoparticles. CBNF with optimum concentration was tested in the parabolic solar collector at 0.76 sun, the evaporation efficiency was estimated to be 73%. To our knowledge, this was the first experimental record of NP-assisted steam production in the limited solar conditions in the Nordic region. Both the laboratory system and the collector test resulted in high superheating of the steam. Even though the rate of solar steam generation (10 ml/min) was not yet sufficient to establish a turbine cycle, the process is applicable for technical desalination, disinfection and direct heating.

Acknowledgements

This study was supported by Russian Science Foundation (project 17-79-10481).

References

[1] O. Neumann, A. S. Urban, J. Day, S. Lal, P. Nordlander, N. J. Halas, Solar vapor generation enabled by nanoparticles, ACS Nano 7 (2013) 42–49.

[2] Y. Fu, T. Mei, G. Wang, A. Guo, G. Dai, S. Wang, J. Wang, J. L, X. Wang, Investigation on enhancing effects of Au nanoparticles on solar steam generation in graphene oxide nanofluids, Applied Thermal Engineering 114 (2017) 961–968.

[3] O. Neumann, C. Feronti, A. D. Neumann, A. Dong, K. Schell, B. Lu, E. Kim, M. Quinn, S. Thompson, N. Grady, P. Nordlander, M. Oden, N. J. Halas, Compact solar autoclave based on steam generation using broadband light-harvesting nanoparticles, PNAS 110 (2013) 11677–11681.

[4] G. Ni, N. Miljkovic, H. Ghasemi, X. Huang, S. V. Boriskina, C.-T. Lin, J. Wang, Y. Xu, M. M. Rahman, T. J. Zhang, G. Chen, Volumetric solar heating of nanofluids for direct vapor generation, Nano Energy 17 (2015) 290–301.

Supplementary materials

to “Solar steam in an aqueous carbon-based nanofluid” by Ulset et al.

S.0. Water chemical composition

Tap water chemical composition is found at:

https://d1pk8xkmonbx0b.cloudfront.net/1504677533/svartediket-2016.pdf

S.1. Carbon black particles

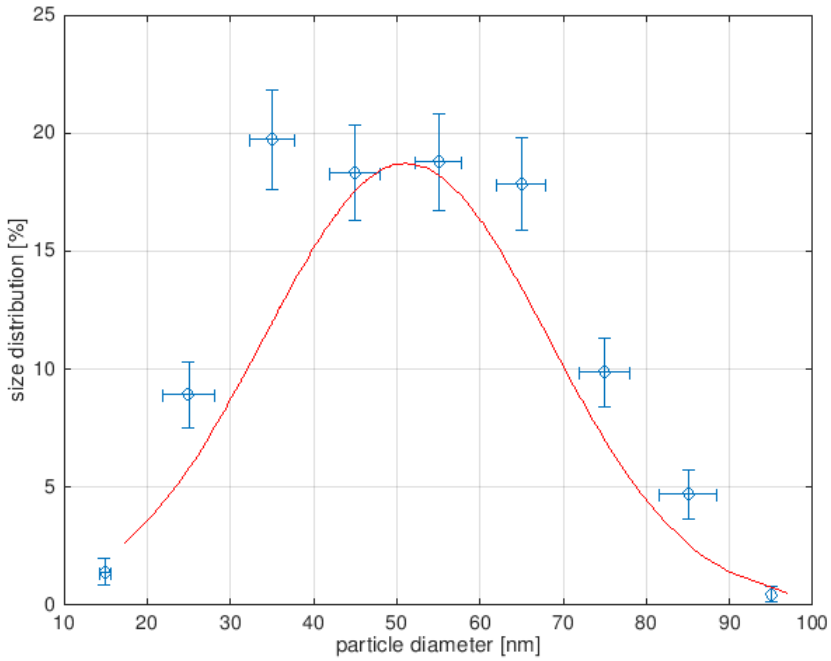

Fig.S.1.1. Particle size distribution: ImageJ analysis of TEM results, red line – normal distribution

S.2 Lamp characterization

Measurement performed with IR-sensor LS122 from Aermanda

The sensor was calibrated with Sol3A Class AAA Solar Simulator from AZPECT (HVL)

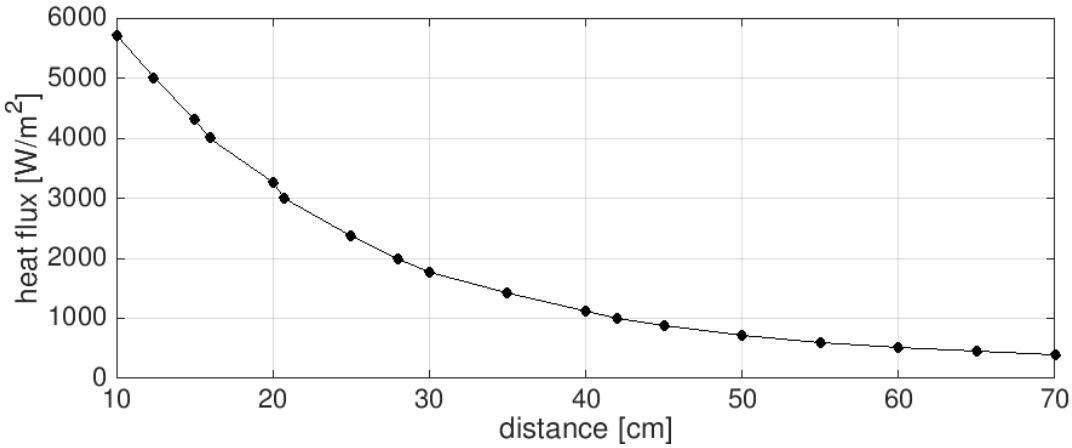

Fig.S.2 Heat flux as a function of distance from the lamp

S.3 Meteorological information. Experiment conducted from 12:57 for an hour.

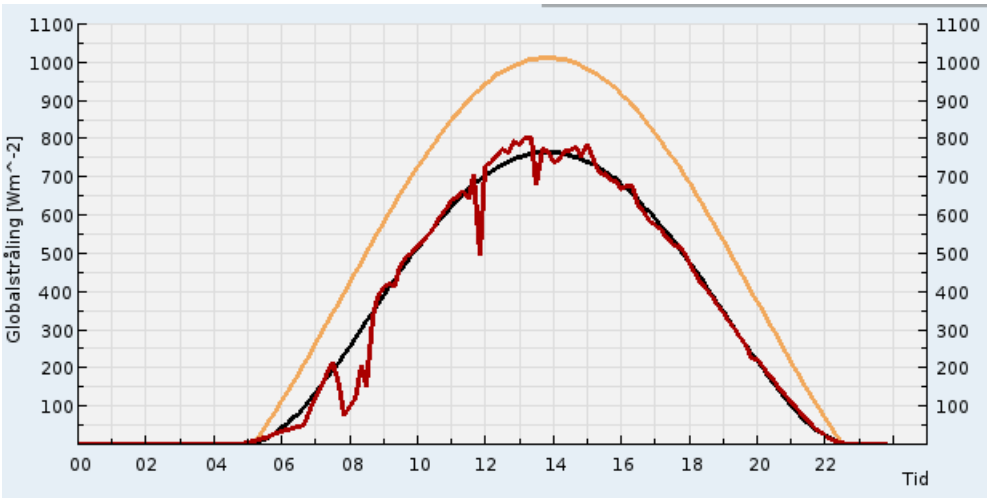

Fig.S.3.1 Solar heat flux (red line) as a function of time (hours)

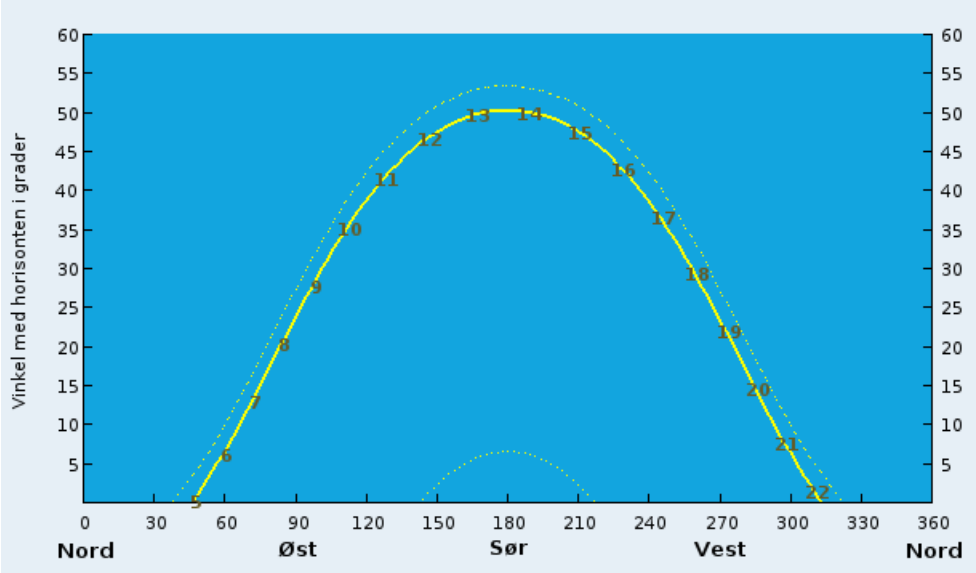

Fig.S.3.2 Sunlight angle (deg.) relative to horizon as a function of time (hours)

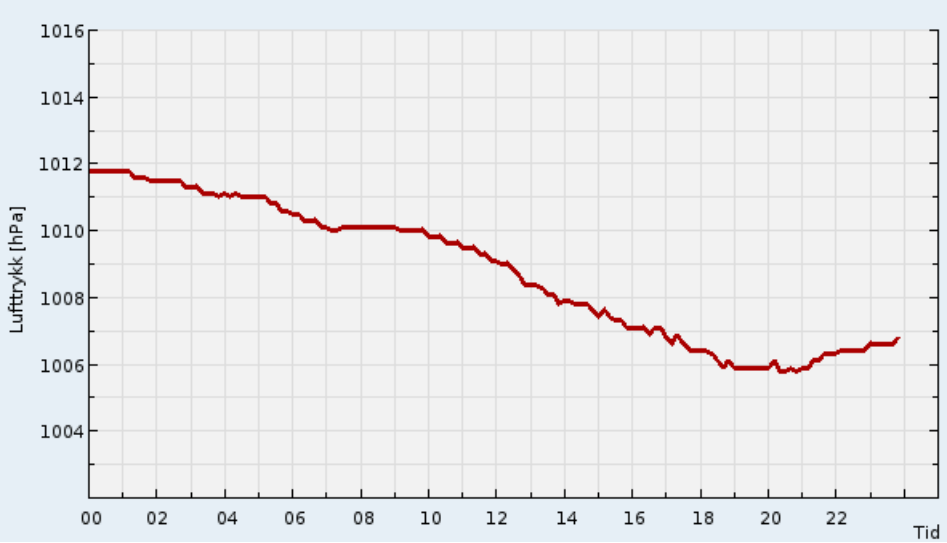

Fig.S.3.3 Atmosphere pressure (hp) as a function of time (hours)

Fig.S.3.4 Relative humidity as a function of time (hours)

Fig.S.3.5 Ambient temperature as a function of time (hours)

S.4 Particle size distribution in condensate

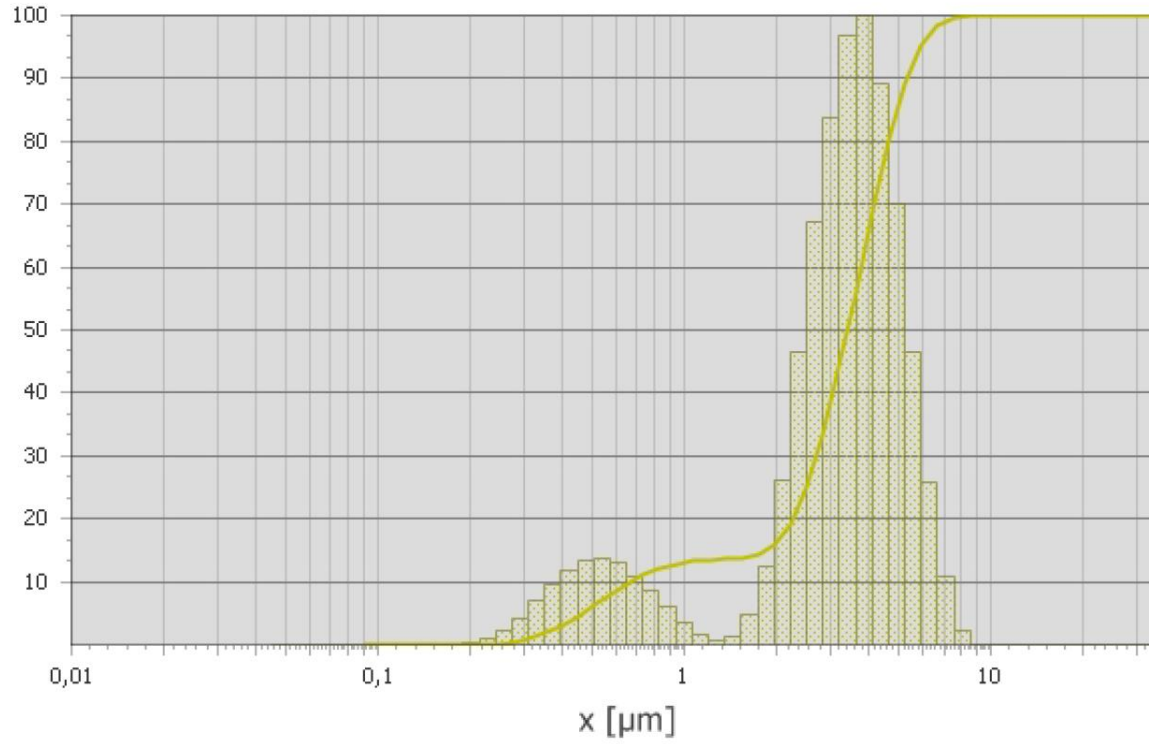

Fig.S.4.1. Particle size distribution in condensate, evaporated from 4.7% (vol.) CBNF

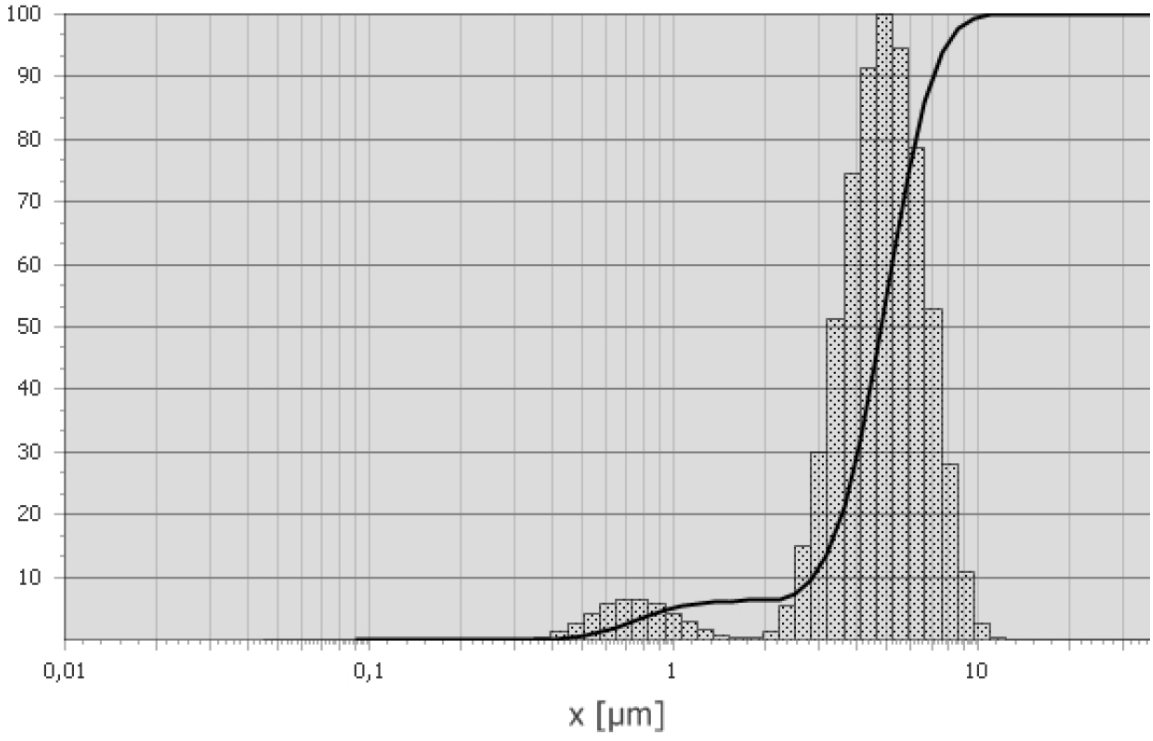

Fig.S.4.2. Particle size distribution in tap water

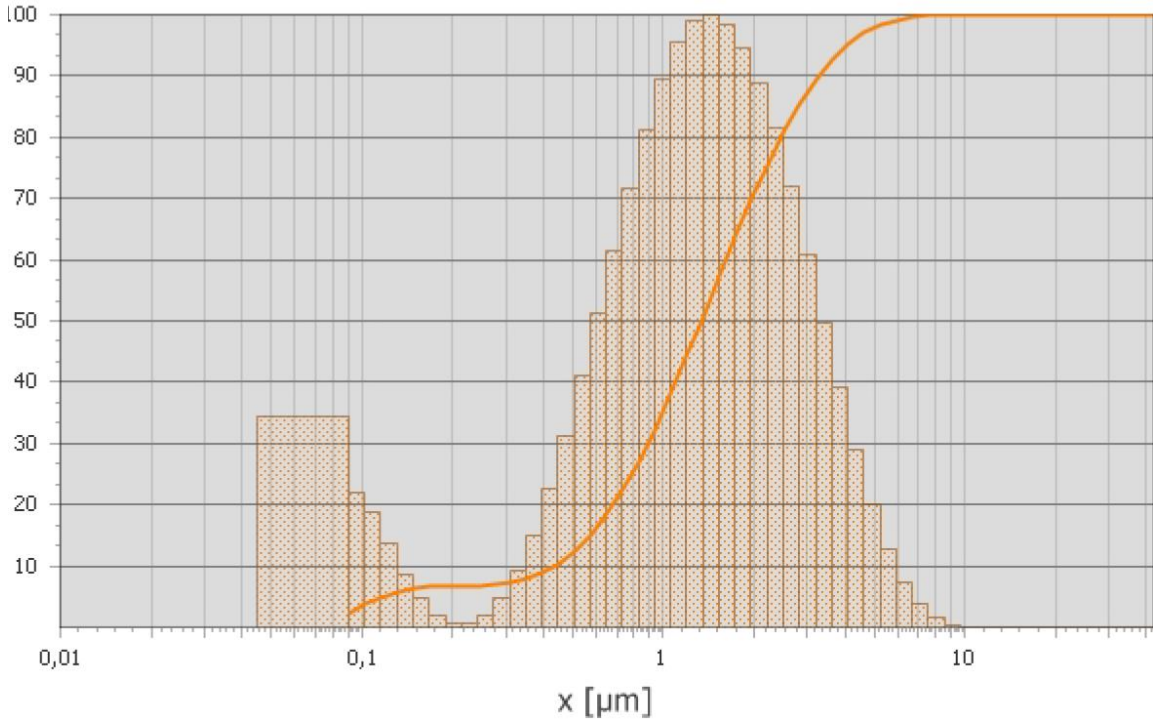

Fig.S.4.1. Particle size distribution in condensate, evaporated from 4.6% (vol.) iron oxide NF